The Influence of Manganese Content and Temperature on the Relative FCC/HCP Phase Stability and Strain-Hardening Behavior of High-Manganese TRIP/TWIP Steels

By

Dean Thomas Pierce

Dissertation

Submitted to the Faculty of the

Graduate School of Vanderbilt University

in partial fulfillment of the requirements

for the degree of

DOCTOR OF PHILOSOPHY

in

Interdisciplinary Materials Science

May, 2014

Nashville, Tennessee

Approved:

James Wittig, Ph.D.

James Bentley, Ph.D.

Greg Walker, Ph.D.

Çağlar Oskay, Ph.D.

To my loving parents, Sandy and Tom Pierce, for their continuous support.

ACKNOWLEDGEMENT

This research would not have been possible without the support of many people and organizations. I would like to express my deepest gratitude to my advisor, Dr. James Wittig, who provided invaluable guidance, assistance and facilitated numerous opportunities for my professional development. I would also like to give special thanks to my collaborators: Dr. José Antonio Jiménez for his technical guidance and assistance with mechanical testing and X-ray diffraction, Dr. James Bentley for the instruction in transmission electron microscopy and technical guidance, professor Çağlar Oskay for his overall support and professor Dierk Raabe and the Max-Planck-Institut für Eisenforschung for their financial and technical support during two summer internships. I would also like to thank Dr. Rudy Ghisleni, Dr. Kai Nowag and Dr. Alex Montagne for the introduction to nanoindentation and providing facility and technical support. I am also grateful for the National Science Foundation Division of Materials Research grant, DMR0805295, which provided the funding for this research.

I would like to express my deepest love and thanks to my girlfriend Ioana for her love and support over the last two and a half years.

A special thanks is also due to my best friend, Edin Balic, who provided the direction and inspiration for my return to graduate school and has been a truly great friend.

TABLE OF CONTENTS

Page

LIST OF TABLES

LIST OF FIGURES

Figure Page

CHAPTER 1

INTRODUCTION

High-manganese austenitic transformation- and twinning-induced plasticity (TRIP/TWIP) steels are a new class of advanced high strength steels (AHSSs) that have received significant research interest over the last decade owing to their superior combination of strain-hardening, strength and ductility compared to other types of steel [1] [2] [3] [4] [5] [6] [7] [8] (see Figure 1-1). The automotive industry is highly interested in these steels as a means to reduce vehicle weight (through down gauging), increase crash worthiness and improve manufacturing efficiency through better room temperature formability. The performance requirements of structural automotive components are largely being driven by more stringent fuel economy and safety requirements. New corporate average fuel economy (CAFE) standards will require the average fuel economy of a manufacturer's fleet of cars and light trucks to be 54.5 miles per gallon (MPG) by 2025 [9]. Increasingly rigorous crash requirements, like the Insurance Institute for Highway Safety (IIHS) offset frontal impact test [10], require materials that can dissipate large amounts of energy during crashes in order to protect vehicle occupants. While lighter-weight materials such as Aluminum and Magnesium will play a role in meeting these requirements, AHSSs currently offer substantial cost savings over the aforementioned materials and are the preferred material to meet these targets [11]. Figure 1-2 shows the estimated production costs/savings associated with reducing vehicle mass with several types of material solutions. AHSSs are currently the only material which can reduce vehicle mass and production costs simultaneously. In fact, several automotive manufacturers, such as Volkswagen [12], have begun replacing aluminum with

thinner gauge AHSS to retain weight savings while lowering costs. The multinational steel manufacturer POSCO has recently produced the first commercially available high-Mn TWIP steel [13] proving that these materials have the potential to play an important part in automotive design in the coming years. However, there are still many aspects of these steels and their unique deformation mechanisms that are not well understood. Further research is necessary to ensure TRIP and TWIP steels become a major part of the solution to the challenges of the automotive community.

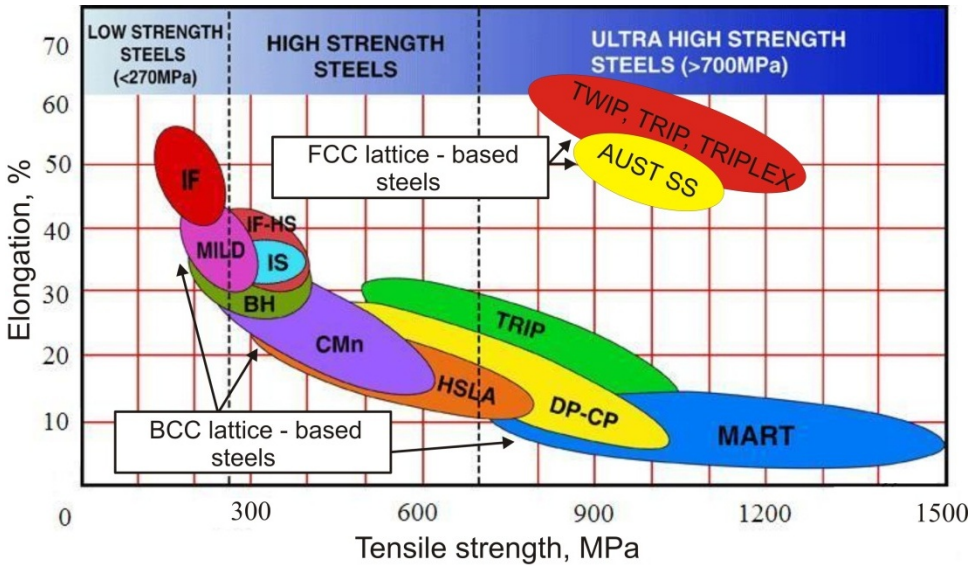

Figure 1-1 – Maximum elongation to failure in tension as a function of ultimate tensile strength (UTS) for several types of structural steels.

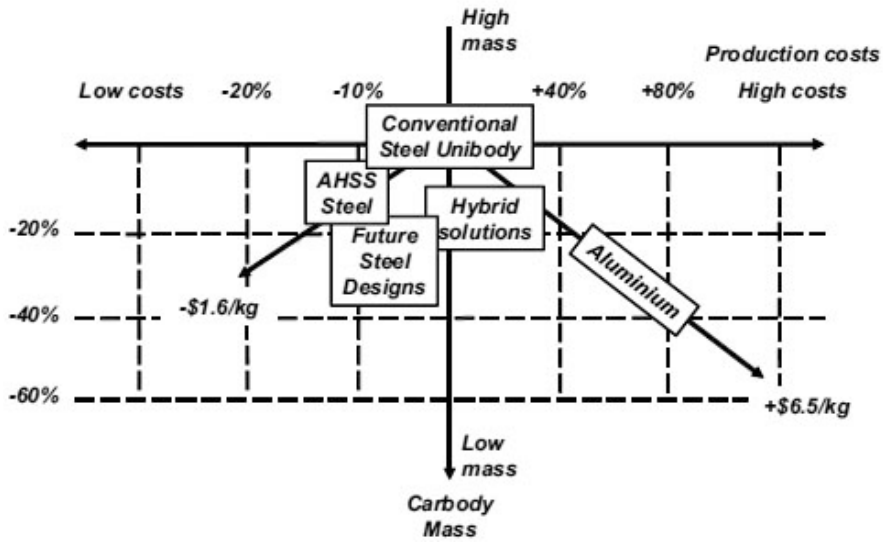

Figure 1-2 – Comparison of production costs and mass reduction for automotive designs based on different material solutions [11].

1.1 Deformation Mechanisms of TRIP and TWIP Steels

Transformation and twinning-induced plasticity steels are metastable and include high quantities of Mn in the range of 18-30 wt.% that allows for retention of the austenitic structure at room temperature (RT). Alloying additions of Al, Si, Cr, C and N are made to optimize mechanical properties [14] [15] [16] [17]. The primary reason for the excellent ductility and strain-hardening of high-Mn TRIP and TWIP steels are deformation mechanisms subsidiary to dislocation glide [4]. During straining of these materials, the austenite deforms by dislocation glide together with secondary deformation mechanisms including $\alpha_{bcc}/\varepsilon_{hcp}$-martensite formation and/or mechanical twinning [18]. These secondary deformation mechanisms are displacive transformations in that they are diffusionless and occur by the cooperative movement of many atoms [19]. They result in

transformation or re-orientation of the crystal structure in the case of martensite or mechanical twinning, respectively. On a micro scale, the martensite platelets and mechanical twins act as planar obstacles to dislocations gliding on non-coplanar slip systems. As the material begins to neck, secondary deformation mechanisms will preferentially occur in these volumes and locally harden the material. The hardening mechanism is considered to be a dynamic Hall-Petch effect, where strain-induced features like martensite and mechanical twins increasingly refine the grain structure as deformation progresses [5] [20] [21] [22] [23] [24] [25] [26] [27] [28]. As local volumes of the sample harden via this mechanism, further deformation will occur in other regions of the specimen with lower flow stress and the process repeats itself. The result is high strain-hardening rates which prevent local necking and lead to long uniform elongations, generally of ~60 to 80% [2]. In addition, since the entire volume of the specimen takes part in the deformation, high energy absorption is also achieved.

The possibility that mechanical twins could act as barriers to dislocation glide was first shown in the Fe-20/32Mn-0/5Cr-0.01/0.48C (wt.%) system by Remy and Pineau [29] in 1977. The authors noted increased work-hardening rates in alloys that exhibited ε-martensite transformation and mechanical twinning. Their work also suggested that the formation of ε-martensite and mechanical twinning were strongly related to temperature and stacking-fault energy (SFE), showing that ε-martensite occurred for SFE values below 11 mJ m^{-2} while mechanical twinning was active from about 5 to 40 mJ m^{-2}. Remy determined a SFE of 11 mJ m^{-2} at room temperature (RT) for an Fe-20Mn-4Cr-0.5C alloy by measuring the size of extended dislocation nodes with transmission electron microscopy (TEM). The Fe-20Mn-4Cr-0.5C alloy exhibited both ε-martensite and mechanical twinning. Kim et al. [28] studied the strain-hardening behavior of an

Fe-30Mn-5Al-0.3C low temperature alloy from -196°C to room RT. For this composition, the ultimate tensile strength (UTS) and ductility were the greatest at -196°C (1150 MPa and total elongation of 60%) where mechanical twinning was most intense. Conversely, the UTS and ductility were the smallest at 25°C (750 MPa and total elongation of 35%) where mechanical twinning was least intense. The authors specifically attributed the excellent ductility at low temperatures to the prevention of local necking by preferential mechanical twinning. Increases in deformation temperature reduced the amount of mechanical twinning and consequently, the strength and ductility. A follow-on study by Kim et al. [30] to investigate the influence of Al content on Fe-30Mn-xAl-0.1Nb-0.3C (x=0, 1, 2, 3, 4 and 5wt.%) steels showed that additions of Al up to 5wt.% improved the ductility at -196°C. Conversely, the Al-free alloy exhibited the best ductility at RT. Qualitatively, this observation may be understood in that reducing the aluminum content caused a strong decrease in the SFE [15] while increasing the temperature increased the SFE. These competing influences on the SFE would likely result in similar SFE values (which are optimal for mechanical twinning) for the Al containing alloy at-196°C and the Al free alloy at RT. The studies by Remy and Pineau [29] and Kim et al. [28] [30] demonstrated that by tailoring the alloy composition, the activation of ε-martensite or mechanical twinning could be obtained in the desired temperature ranges.

The work of Frommeyer at the Max-Planck-Institut für Eisenforschung in Dusseldorf, Germany (Grässel et al. [1] [2] and Frommeyer et al. [31] [32]) from 1997 to 2006 is largely credited with renewing interest in these materials [11]. This research group studied the microstructure and mechanical properties of several different Fe-15/20/25/30Mn-3Al-3Si TRIP and TWIP alloys that exhibited $\alpha_{bcc}/\varepsilon_{hcp}$-martensite formation and/or mechanical

twinning. The alloy which displayed the best RT elongation (Fe-25Mn-3Al-3Si) also showed the most intense mechanical twinning with no strain-induced ε-martensite (detectable by x-ray diffraction (XRD)). As the Mn content was reduced the secondary deformation mechanisms changed from mechanical twinning to martensite formation which increased the strength and reduced ductility. Correspondingly, increasing the Mn content from 25 to 30 wt% caused a slight reduction in both strength and ductility. Additions of Mn influence the plasticity mechanisms and mechanical properties indirectly through changes in the SFE since Mn has a negligible effect on solid solution hardening [6]. The authors concluded that the greatest ductility was achieved due to strong mechanical twinning and the absence of ε_{hcp}-martensite. The authors also suggested that a SFE energy above ~20 mJ m^{-2}, calculated by the regular solution model, was sufficient to prevent the formation of ε_{hcp}-martensite. While both TRIP and TWIP alloys exhibit exceptional ductility, the elongation of TWIP alloys is usually greater. This may be caused by the reorientation of the austenitic matrix by twinning which can result in more favorable orientations for dislocation glide and is termed “texture softening” [33]. Allain et al. [34] also studied the different mechanical behavior associated with ε-martensite formation, mechanical twinning, and pure dislocation glide by deforming an Fe-22Mn-0.6C alloy at -196, 25 and 400°C. At RT the alloy deforms by dislocation glide and mechanical twinning and exhibits substantially better ductility than the other two test temperatures. The authors calculated the SFE and suggested that ε-martensite forms below 18 mJ m^{-2}, mechanical twinning between 12 and 35 mJ m^{-2}, and only dislocation glide above 35 mJ m^{-2}. Saeed-Akbari et al. [35] developed a sub-regular thermodynamic model for predicting SFE and suggested a similar SFE value of 20 mJ m^{-2} as a target to achieve optimal mechanical twinning and suppress ε-martensite formation. The ability

to estimate the SFE through thermodynamic models has made it possible to design alloys that have specific deformation mechanisms and mechanical properties.

In the last decade or so research on TRIP and TWIP steel had primarily focused on the Fe-Mn-C-(Al), Fe-Mn-Cr-N and Fe-Mn-Al-Si systems. TWIP steels containing C exhibit superior flow stress as illustrated by the comparison of true-stress vs. true-strain curves of Fe-20Mn-1.2C and Fe-28Mn-2.8Al-3.5Si steels in Figure 1-3. Idrissi et al. [36] analyzed the structure of the mechanical twins in each alloy and found that twins in the C-containing alloy were thinner and contained a much larger amount of sessile dislocations. The authors suggested that in the context of the strain-hardening model proposed by Gil Sevillano et al. [37], which emphasizes the importance of twin thickness, that the critical stress required for plastic deformation of the twin lamellae will be greater in the C containing steel. In addition, Adler at al. [38] pointed out that the shear of atoms due to mechanical twinning will move atoms which are normally situated above unoccupied tetrahedral sites to positions above octahedral sites normally occupied by C, converting octahedral sites to tetrahedral. If carbon atoms in the octahedral sites become trapped (upon conversion to a tetrahedral site) a lattice distortion could ensue and cause an additional hardening mechanism [38]. Some atom probe tomographic (APT) studies have shown that C has a propensity to segregate to twin boundaries in Fe-Ni-C and Fe-C-Mn-Si alloys [39] [40]. However, a more recent study investigated the same bundle of mechanical twins in an Fe-22Mn-0.6C alloy using scanning transmission electron microscopy (STEM) and APT and found no evidence of C or Mn segregation at the twin boundaries [41].

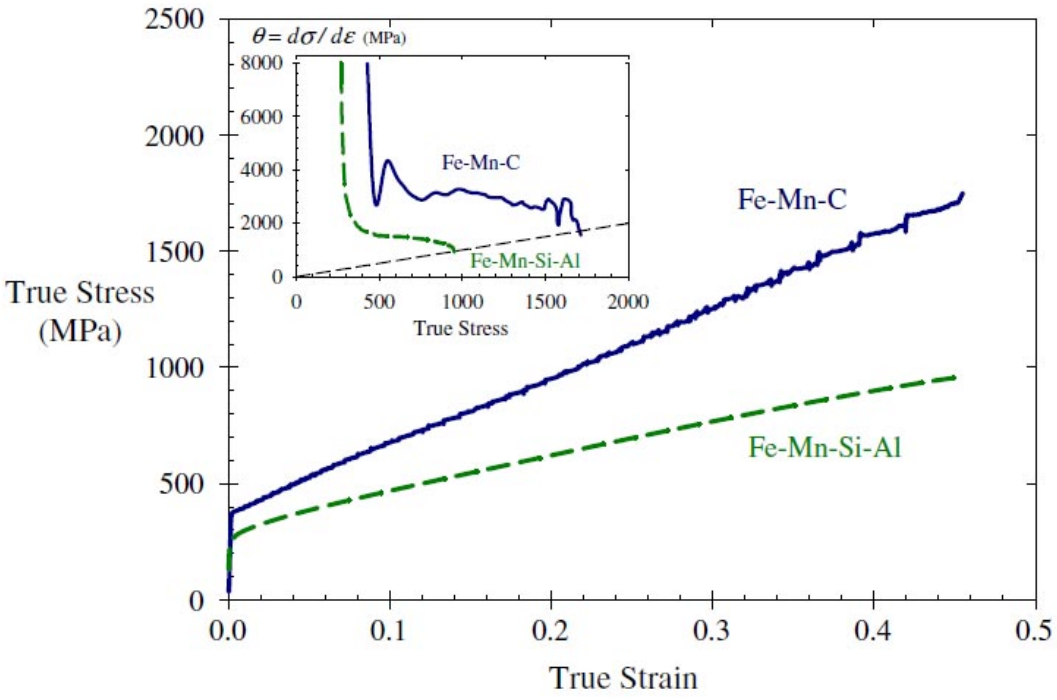

Figure 1-3 – Room temperature true stress vs. true strain curves and work hardening rate (dσ/dε) (inset) vs. true stress for Fe-20Mn-1.2C and Fe-28Mn-2.8Al-3.5Si alloys [36].

The microstructural and texture evolution Fe-22Mn-0.6 C TWIP steels has been studied in depth. Barbier et al. [42] showed that during deformation the volume fraction of grains oriented with <111> in the tensile direction increases substantially (from 20% in the recrystallized condition to 50% at failure) and that mechanical twinning was more intense in grains with <111> in the tensile direction, consistent with the highest Schmid factor for twinning. The influence of the re-orientation of the matrix by mechanical twinning on the texture was found to increase the amount of grains oriented with <100> in the tensile direction slightly. Gutierrez-Urrutia et al. [21] also noted strong twin formation in grains oriented with <111> in the tensile direction and general compliance with Schmid's law but only for true strains below 0.3. This work also noted that decreasing the grain size from ~50 to 3 μm reduced the activity but did not completely suppress mechanical twinning. Gutierrez-Urrutia and Raabe [14] investigated the dislocation and

twin substructure evolution using electron channeling contrast imaging (ECCI). At the earliest stages of plastic deformation (below 0.1 true strain) the microstructure was comprised of dislocation cells. The authors noted that mechanical twinning is not responsible for the initial inflection of the strain hardening rate (occurring at ~0.06 true strain) in TWIP steels as was previously thought by Barbier et al. [42]. Instead, the influence of mechanical twinning on the strain-hardening becomes significant after 0.1 true strain. From strains of 0.1 to failure the grains exhibited 3 different types of microstructures based on orientations with <111>, between <111> and <100>, and <100> parallel to the tensile direction. Grains in the <111> orientation exhibited mechanical twinning on multiple slip systems. Grains oriented between <111> and <100> contained mechanical twinning in one slip system corresponding to the highest Schmid factor. The microstructures of grains in the <100> orientation were dominated by dislocation cell (DC) structures where the cell size became smaller with increasing strain, highly dense dislocation walls (HDDWs), and minimal twinning activity. The authors quantified the contribution of each type of grain to the flow stress.

A noticeable difference in the flow stress of the Fe-Mn-C steel in Figure 1-3 is the presence of serrations in the stress-strain curve. The serrations are thought to be dynamic strain ageing (DSA) caused by point-defect complexes: C-vacancy complex, C-C complex and C-Mn complex instead of long range diffusion of C atoms to dislocation cores [43]. The DSA causes the deformation of Fe-Mn-C TWIP steels to be localized in deformation bands which cross the specimen [6] [44]. DSA in these materials causes several undesirable effects including limited post-uniform elongation [6], a negative strain-rate sensitivity [4] and surface roughness which can be difficult paint [45]. The addition of small quantities of Al (1.5 and 2.5 wt.%) to Fe-18Mn-

0.6C steel has been shown to effectively suppress the DSA at RT, lower the sensitivity to delayed fracture [11], slightly increase the yield strength due to solid solution hardening, and cause a moderate reduction in work-hardening and ductility due to a higher-than optimal SFE [46]. Therefore, in the last few years the influence of Al additions to TWIP steels has garnered significant attention [18] [47] [48] [46]. Jeong et al. [16] recently reported on the influence of Si additions to Fe-18Mn-0.6C steel and found that it suppressed DSA similar to Al but has the beneficial effect of increasing the work hardening rate. The authors attributed the better strain-hardening to a reduction in SFE due to Si additions which increased the formation of mechanical twins during deformation. Finally, a review of computational thermodynamic methods for the calculation of SFE on FeCrMnN alloys has recently been published by Mosecker and Saeed-Akbari et al. [17], suggesting increasing interest in TWIP steels with increased corrosion resistance.

1.1.1 Stacking Sequence in Close Packed Materials

In close-packed materials the stacking sequence of close-packed planes is ABCABC (for FCC materials) or ABAB for (HCP) materials. The differences in these structures are illustrated schematically in Figure 1-4. The atomic structure in each close packed plane is the same for FCC and HCP with each atom having six nearest (in-plane) neighbors as depicted in Figure 1-4a. The next layer is stacked above the voids in the structure in one of two orientations as shown in Figures 1-4b and c. The third plane of atoms can be stacked as in Figure 1-4d to generate the FCC structure or 1-4e to form the HCP structure.

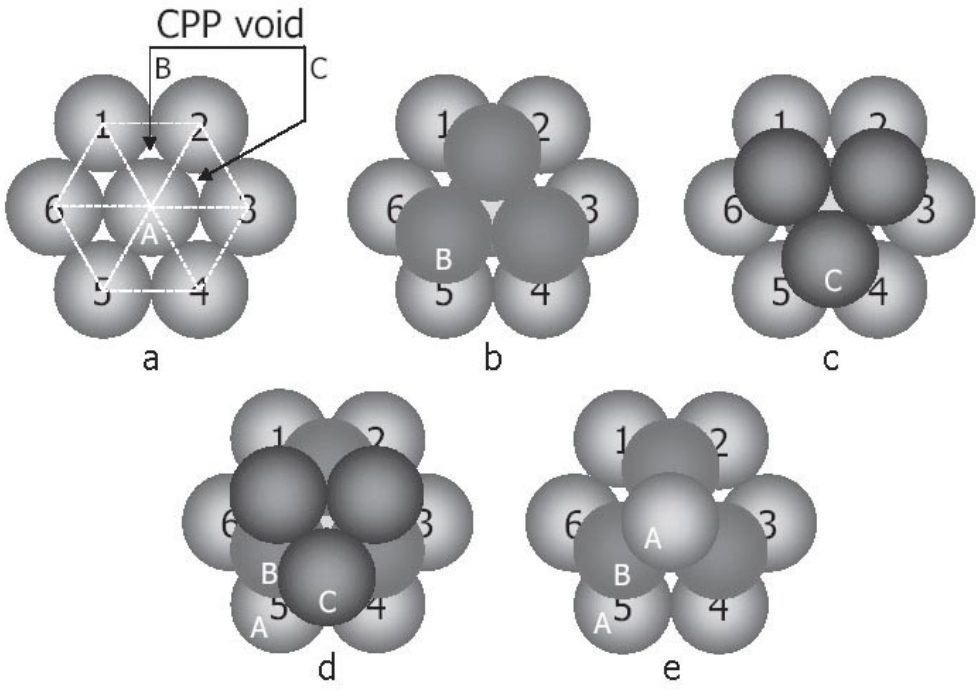

Figure 1-4 – Diagram of the stacking sequence in FCC and HCP crystals as viewed along a <111> direction [5]. (a) depicts the atomic configuration of a CPP in either FCC or HCP materials. (b) and (c) represent two choices of placement for the next CPP. Stacking the CPPs in the "c" sequence as shown in (d) or the "a" sequence as shown in (e) yields the FCC and HCP structures respectively.

1.1.2 Stacking Faults in FCC Materials

A single intrinsic stacking-fault can form in FCC materials by the dissociation of a perfect dislocation with total dislocation Burgers vector of type $b_T = \frac{a}{2}[-101]$ (where a_{FCC} is the lattice parameter of the FCC phase) into two Shockley partial dislocations of Burgers vector type $b_p = \frac{a}{6}[-1-12]$ and $b_p = \frac{a}{6}[-211]$ by the following dislocation reaction:

$$\frac{a}{2}[-101] \rightarrow \frac{a}{6}[-1-12] + \frac{a}{6}[-211] \quad (1\text{-}1)$$

The driving force for the above reaction is related to the strain energy of the individual dislocations. According to the Frank energy criterion [49], since the strain energy of a dislocation is proportional to the magnitude of its Burgers vector squared, the strain energy of single perfect

dislocation will be greater than the sum of the energies of the two Shockley partials, and the reaction in Equation (1-1) will be favored. The two Shockley partial dislocations exert an elastic repulsive force on one another that varies as a function of $1/d_{actual}$, where d_{actual} is the separation distance between the two partial dislocation cores [49]. Figure 1-5a schematically illustrates a perfect dislocation of edge character (as looking in the [111] direction), followed by the nucleation of two Shockley partial dislocations in 1-5b and their subsequent repulsion in 1-5c leading to an intrinsic stacking fault. Stacking faults may be intrinsic, extrinsic or twins. The formation of these types of faults could occur by the passage of Shockley partial dislocations as depicted in Figure 1-6. The passage of a single Shockley partial results in an intrinsic stacking-fault (Figure 1-6b). The passage of an additional Shockley partial on the next {111} plane causes an extrinsic stacking fault (Figure 1-6c). Finally, the passage of a third Shockley partial results in a 3-layer mechanical twin (Figure 1-6d). Figure 1-7 shows an intrinsic stacking fault, extrinsic stacking fault, and twinning fault (twin boundary) and illustrates which plane of atoms resides in a local HCP environment (dark circles).

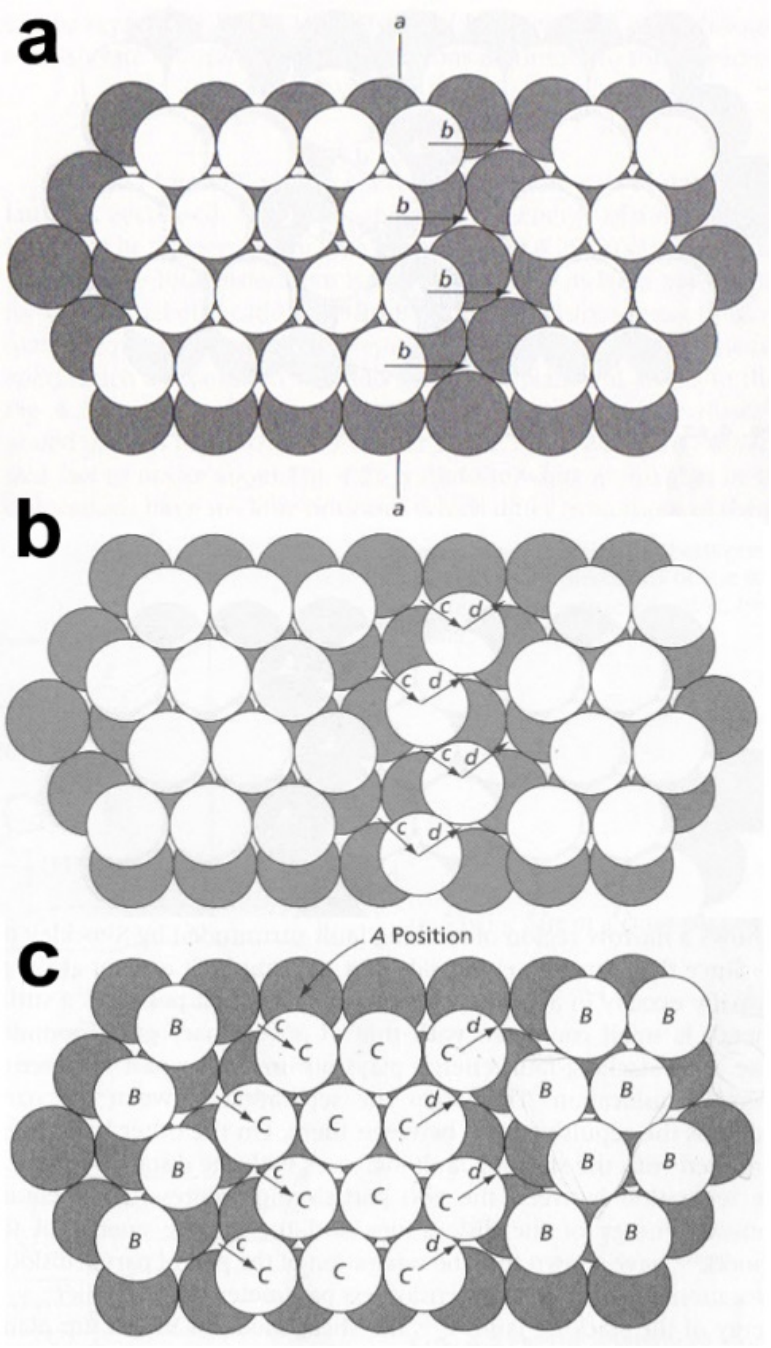

Figure 1-5 – (a) Perfect dislocation in an FCC crystal structure (dark circles represent atoms in the "a" stacking position). The vertical line designated "a" represents the perfect dislocation (i.e., the extra plane of atoms inserted into the crystal structure). (b) Partial dislocations in an FCC structure and (c) the formation of a stacking fault [19].

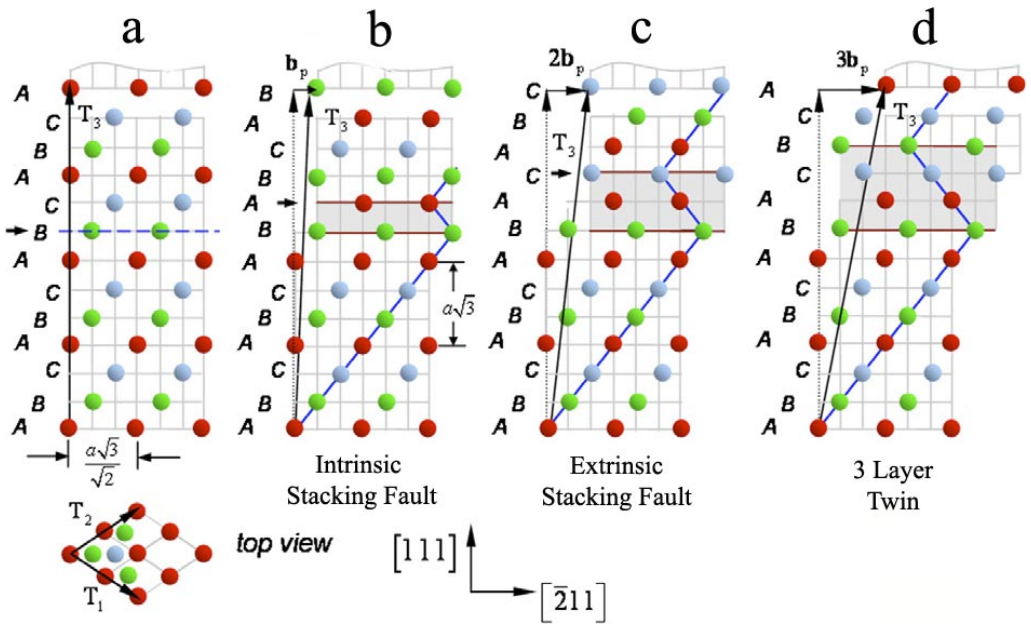

Figure 1-6 – Stages of nucleation of a mechanical twin by the passage of Shockley partial dislocations with $b_p = a/6[-211]$ on successive (111) glide planes (indicated by arrows). (a) Perfect FCC lattice, (b) intrinsic stacking-fault, (c) extrinsic stacking fault and (d) 3-layer twin. Displacement is indicated by the translation vector T_3 [50].

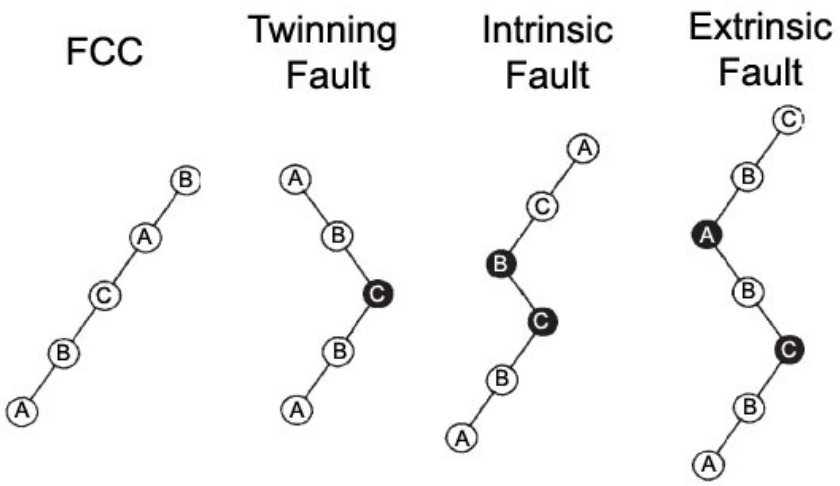

Figure 1-7 – Stacking sequence (from left to right) of a perfect FCC crystal, a twinning fault (twin boundary), intrinsic fault and extrinsic fault. Black circles denote a local HCP environment.

1.1.3 ε-Martensitic Transformation

Epsilon-martensite possesses an HCP structure and can form in certain steels spontaneously upon cooling below the martensite start temperature or as a result of deformation. This type of martensite forms in austenite with the $(111)_\gamma||(0001)_\varepsilon/[1\text{-}10]_\gamma||[1\text{-}210]_\varepsilon$ orientation relationship (i.e., close-packed planes and directions are parallel in both crystal structures). Lower SFE and increased stability of the HCP phase relative to the FCC phase increase the propensity for ε-martensite formation [51]. Ideally, the nucleation of ε-martensite could occur from the passage of a Shockley partial dislocation on every second close packed plane [51]. The nucleation during deformation was investigated in Fe-Cr-Ni austenitic steels using in-situ TEM by Brooks et al. [52] [53]. The authors observed that ε-martensite usually forms on the operating slip plane and nucleated from the conglomeration of irregularly spaced stacking faults which gradually (with more deformation) become thicker, leading to larger, more energetically favorable regions of ABAB stacking. In addition, the assembly of stacking faults minimizes the total austenite/ε-martensite interfacial energy. The authors calculated an approximate 1-2% contraction of the spacing perpendicular to the fault plane by comparing TEM electron micrographs of overlapping stacking-faults to computed micrographs of the same stacking-faults. The procedure for computing the electron micrographs is further detailed in [54]. X-ray diffraction on larger volumes of ε-martensite in binary Fe-Mn reveal a contraction in molar volume of ~1-2% relative to the austenite [55] [56]. The coherency strain energy that arises from the contraction of the fault plane within the FCC matrix was treated by Olson and Cohen [51] and Müllner and Ferreira [57] and will be discussed further in Section 1.3.2.

1.1.4 Mechanical Twinning

Mechanical twinning in FCC and HCP materials has been extensively reviewed by Christian and Mahajan [58]. The classical definition of twinning requires that the twin and matrix lattices be related by a reflection in some plane or by a rotation of 180° about some axis [58]. The nucleation and growth of mechanical twins could occur by the passage of Shockley partial dislocations on successive {111} planes as shown schematically in Figure 1-6. In this respect, mechanical twinning is closely related to the formation of ε-martensite transformation where Shockley partial would need to pass on every second {111} plane. A low-to-moderate SFE in the range of ~12 to 45 mJ m^{-2} is typically a necessary condition for mechanical twinning [3] [29] [34]. The "coherent" twin is separated from the matrix by two planar twin boundaries or twinning faults as depicted in Figure 1-7. While Figure 1-6 shows how a mechanical twin could form, several competing mechanisms have been proposed to describe the nucleation of mechanical twins. Steinmetz et al. [20] developed a multiscale dislocation-density type model for the strain-hardening behavior of TWIP steel which included a twin nucleation model developed by Mahajan and Chin [59]. The model of Steinmetz et al. exhibited quite good agreement with experimental results. The twin nucleation model of Mahajan and Chin [59] proposes that two perfect dislocations on neighboring {111} planes in the primary slip system split into fault pairs and react to produce three Shockley partial dislocations. Several other mechanisms for twin formation have also been proposed [60] [61] [62] [63]. Idrissi et al. [64] analyzed the mechanism of twin nucleation in an Fe-20Mn-1.2C steel and reported that the mechanism is best explained by the nucleation models of Miura, Takamura and Narita (MTN model) [62] or Cohen and Weertman [60] [61]. The MTN model is based on the pile-up of dislocations at a Lomer

dislocation at the primary and cross slip plane junction. The dislocations react to form two Shockley partial dislocations and a Frank sessile dislocation creating a double layer fault which serves as the twin nucleus. Cohen and Weertman proposed that the twin nucleus forms from the dissociation of a perfect dislocation into a sessile Frank partial screw dislocation and a glissile Shockley partial when interacting with a Lomer-Cottrell barrier.

1.2 Phase Stability of Binary Fe-Mn Alloys

The equilibrium phase diagram of binary Fe-Mn is shown in Figure 1-8 [65]. The eutectoid point corresponding to the FCC↔body centered cubic (BCC)(A2)+BCC(A12) reaction occurs at 528K and at 0.431 mol fraction of Mn [65]. Below the eutectoid temperature exists a two phase region of BCC(A2) and BCC(A12) for Fe-rich alloys. The BCC(A12) corresponds to the α-Mn structure which is comprised of a 58-atom unit cell and is based on a BCC lattice with each of the two lattice points comprised of a 29-atom basis [66].

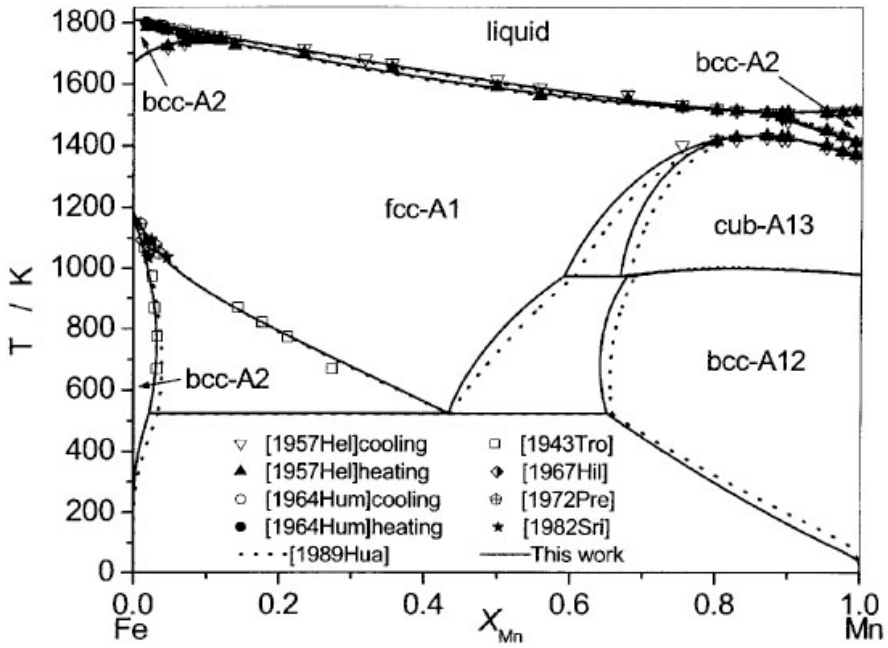

Figure 1-8 – Phase diagram of the Fe-Mn system calculated by Witusiewicz et al. [65] (for the work cited on this figure the reader is referred to the original reference [65]).

A fully austenitic metastable microstructure at room temperature (RT) is retained by cooling alloys with sufficiently high quantities of Mn (typically around 30 wt.%) [67]. Of significant importance to the plasticity mechanisms of Fe-Mn based steels is the relative stability between the metastable FCC and HCP phases due to its influence on the deformation mechanisms. The metastable phase diagram of the FCC and HCP phases is shown in Figure 1-9. The upper and lower solid lines of this figure represent the austenite (A_s) and martensite start (M_s) temperatures respectively. These temperatures correspond to the start of spontaneous martensitic (diffusionless) transformation of the crystal structure to HCP or FCC depending on the initial crystal structure and whether heating or cooling.

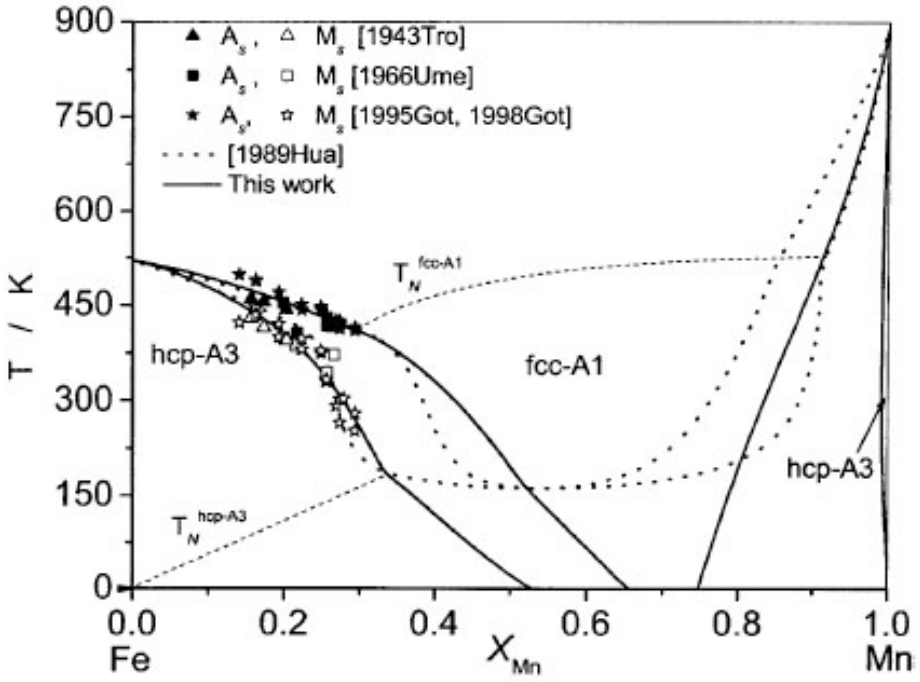

Figure 1-9 – Metastable phase diagram of the FCC and HCP phases of the Fe-Mn system from Witusiewicz et al. [65]. The solid lines represent the austenite (A_s) and martensite start (M_s) temperatures (for the work cited on this figure the reader is referred to the original reference [65]).

1.3 Stacking Fault Energy

The SFE is a composition- and temperature-dependent material property that significantly influences the mechanical properties of FCC materials [19]. The SFE arises due to a fault in the stacking sequence of a material and its value is specific to the type of fault (i.e., intrinsic SFE, extrinsic SFE, etc.). In the present work, the SFE will always refer to the intrinsic SFE unless otherwise noted. Since the SFE plays an important role in the properties of FCC materials there

has been significant interest in both measuring and calculating this parameter since the late 1950s.

1.3.1 Methods of Measurement

Several experimental methods exist for the determination of the SFE. The most prevalent are those that use transmission electron microscopy (TEM) for the direct observation of the size of faulted dislocation configurations. The specific dislocation configurations from which the SFE is typically measured are extended three-fold nodes and Shockley partial dislocation pairs. The method of SFE determination pertaining to each of these dislocation configurations will be discussed in detail in sections 1.3.1.1 and 1.3.1.2. Indirect methods of SFE measurement from X-ray diffraction line profiles and peak shifting are possible but will not be discussed in detail here [68] [69] [70].

1.3.1.1 Extended Three-Fold Nodes

It was first suggested by Whelan that the SFE could be determined from the size of an extended three-fold node in equilibrium by equating the force balance between the faulted region and the node arms by Equation (1-2) [71].

$$\gamma = {\mu b_P^2}/{2R} \tag{1-2}$$

where γ is the SFE, μ is the shear modulus, b_p is the partial dislocation Burgers vector and R is the outer radius of curvature of the node. This approach was refined by theories from Brown

[72], Brown and Tholen [73], Siems [74] and Jøssang et al. [75] which were reviewed by Ruff [76]. These refinements included additional measurable variables such as the inner node radius and total dislocation character angle of the node arms β. Equation (1-3) gives the relationship between these variables according to the theory of Brown and Tholen [72] [73]:

$$\gamma = \frac{\mu b_p^2}{y}\left[0.055\left(\frac{2-\nu}{1-\nu}\right) - 0.06\left(\frac{\nu}{(1-\nu)^2}\right)\cos 2\beta + \left\{0.018\left(\frac{2-\nu}{1-\nu}\right) + 0.036\left(\frac{\nu}{1-\nu}\right)\cos 2\beta\right\}\log\frac{R}{\epsilon}\right] \quad (1\text{-}3)$$

where ν is Poisson's ratio and ϵ is a cut-off parameter approximately equal to b_p [72] [73]. Figure 1-10, taken from reference [76], shows a schematic of an extended three-fold node. The node is made up of three separate partial dislocations which bound the stacking fault. The dislocation reactions required to form such nodes are described in detail by Whelan [71]**.** The relevant dimensions of the node needed to determine the SFE are labeled on Figure 1-10.

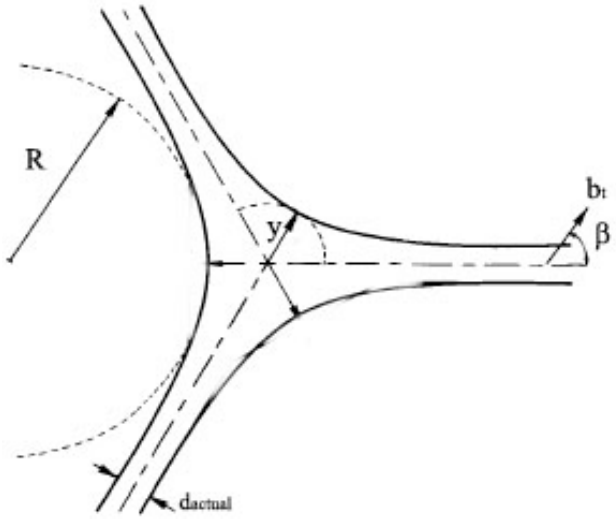

Figure 1-10 – Variables used calculate the SFE from an extended three fold node from several theories [73] [74] [75].

The node dimensions must be obtained by TEM with the node perpendicular to the beam direction or measurements such as the radius of curvature and inner radius must be corrected to their true values. A correction procedure is outlined by Ruff [76].

Results of SFE measurements using these methods have been reported by several authors on Fe-Cr-Ni alloys [77] [54]. Latanison and Ruff investigated the temperature dependence of the SFE in Fe-10Ni-18Cr and Fe-16Ni-19Cr alloys from RT to 325°C. At RT the SFE values are 16 and 24 mJ m^{-2}, respectively, indicating that additions of Ni, a strong austenite stabilizer, increase the SFE. In addition, the SFE of both alloys shows a positive temperature sensitivity from RT to 325°C, where the SFEs are 30 and 32 mJ m^{-2}, respectively. However, upon cooling to RT the nodes do not return to their initial size which the authors attributed to solute atmospheres which gathered around the dislocations at higher temperatures and impeded node expansion upon cooling. Therefore, the recovered nodes produced a higher apparent SFE at RT than the as-deformed nodes. An increase in SFE with temperature is common in steel since austenite typically becomes more stable as the temperature is increased above RT, as shown by Figure 1-8. Bampton et al. [54] measured the SFE of five different austenitic stainless steels with varying Cr and Ni content, finding that additions of Ni raised the SFE while the effect of Cr was complex (small increases and decreases in the SFE were observed with additions on Cr depending on other alloying constituents). The RT SFE of the austenitic steels in their study ranged from 18-35 mJ m^{-2} and heat treatments were performed at several different temperatures (300, 700 and 1050°C) to facilitate the formation of symmetrical nodes for SFE measurement. The authors found that the RT node size varied inversely with prior heat treatment temperature for individual compositions. For instance, RT average SFEs were 47.5 and 24.25 mJ m^{-2} for an Fe-21Cr-14Ni

steel for samples which were annealed at 1050 and 300°C, respectively. The authors attributed this finding to solute impedance forces limiting node expansion upon cooling [54]. Gallagher reviewed the experimental results for the magnitude of the SFE and its variation with temperature and alloying for many different FCC pure elements and alloys [78]. One conclusion from this review is that the apparent SFE measured from nodes in as-deformed samples is likely to be lower than the true value due to solute impedance forces. Interpreting the data from SFE measurements on extended nodes leads to a few important conclusion regarding this method. Prior thermo-mechanical history of the node to be measured can significantly influence the magnitude of the measured SFE and must be considered in any interpretation of data obtained by this method. SFE values from nodes which have formed upon annealing are likely to have higher apparent SFE than those in as deformed specimens. Trends in the SFE as a function of alloying additions are at least qualitatively valid when using this method so long as any thermo-mechanical treatments are consistent between samples being compared [54].

Three studies have reported SFE values for Fe-Mn based steels by measurement of extended dislocation nodes. Volosevich et al. reported SFE values as a function of temperature for binary Fe-16/18/20/22/25/30Mn (wt.%) [79] and a series of Fe-Mn-C [80] alloys with Mn and C contents ranging from 12-18 and 0.23 to 1.35 wt.%, respectively. Remy published SFE values of an Fe-20Mn-4Cr-0.5C alloy as a function of temperature from 100-390K [81]. The data from these studies are presented in Figure 1-11. Increases in temperature caused an increase in SFE for each alloy. In addition, the data show that for the Fe-12Mn-0.2-1.35C steels additions of C strongly increase the SFE by ~26 mJ m^{-2} $wt.\%^{-1}$. In the binary Fe-Mn alloys and the Fe-20Mn-4Cr-0.5C alloy the sensitivity of the SFE to temperature becomes less at lower temperatures. In

particular, the Fe-20Mn-4Cr-0.5C exhibits almost no change in SFE from -175 to 0°C. The SFE exhibits non monotonic behavior with additions of Mn content as shown from the results of Volosevich et al. [79], Figure 1-12, with a minimum in the SFE occurring at ~ 22 wt. Mn.

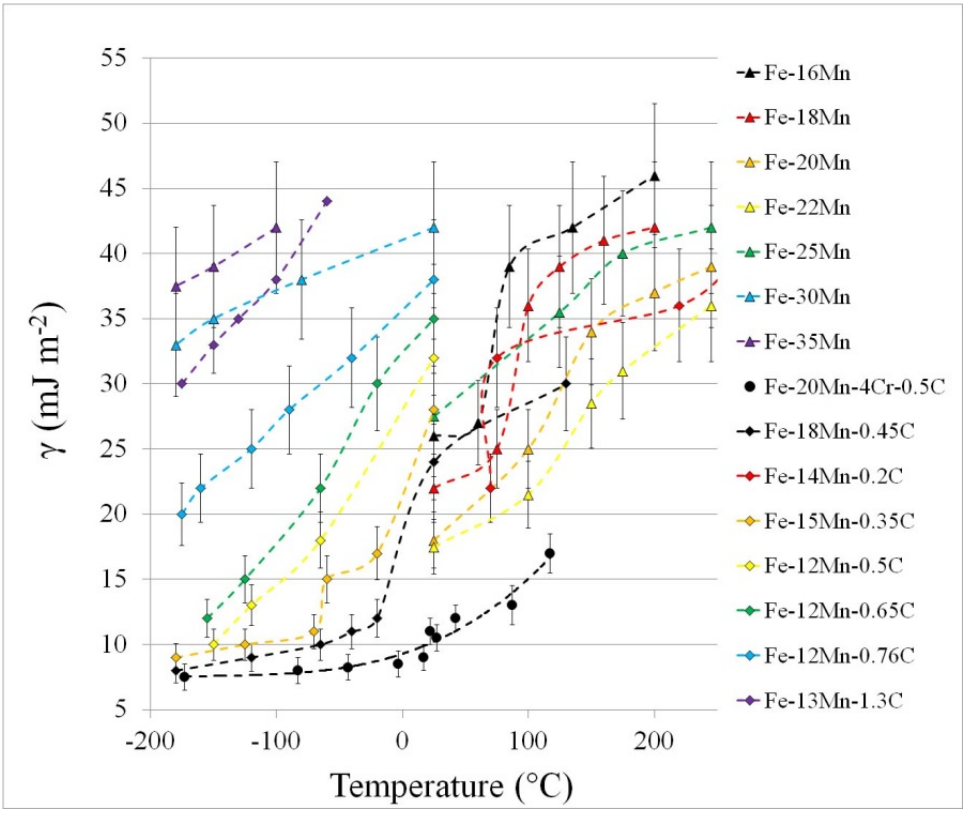

Figure 1-11 – Measured SFE values from the literature for binary Fe-Mn alloys (triangles) [79], Fe-Mn-C alloys (diamonds) [80] and an Fe-20Mn-4Cr-0.5C wt.% steel (circle) [81].

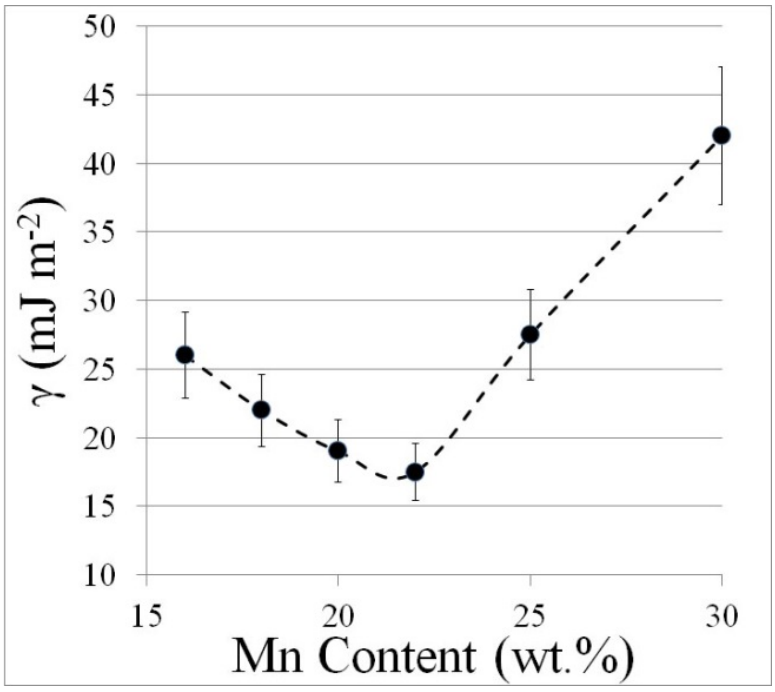

Figure 1-12 – SFE values measured from extended dislocation nodes for binary Fe-Mn alloys [79].

1.3.1.2 Partial Dislocation Separations

The SFE can also be determined from the separation distance of Shockley partial dislocation pairs. A repulsive force per unit length of dislocation line acts on the two partial dislocations and tends to separate them in order to minimize the total strain energy. The SFE from the newly created fault causes an attractive force per unit length of dislocation line (note: while SFE is typically provided in units of energy/area it is equivalent to force per unit length). The resulting force balance is illustrated in Figure 1-13. The classical equation based on isotropic elasticity theory relating the elastic repulsive force to the SFE is [49]:

$$\gamma_{exp} = \frac{\mu b_p^2}{8\pi d_{actual}} \frac{2-\nu}{1-\nu}\left(1 - \frac{2\nu cos2\beta}{2-\nu}\right) \quad (1\text{-}4)$$

where μ, ν, and b_p are the polycrystalline shear modulus, polycrystalline Poisson's ratio and $a_o/6<112>$ partial-dislocation Burgers vector, respectively. However, for materials that exhibit anisotropic elasticity, the elastic repulsive force is a function of the dislocation character angle (β) and the three single-crystal elastic stiffness constants, C_{11}, C_{12} and C_{44}. Therefore, the validity of Equation (1-4) for use on materials that show significant elastic anisotropy is questionable. Thus, a more accurate method to determine the elastic repulsive force is to account for anisotropic elasticity. Several authors have employed pure anisotropic dislocation theory to address this problem [82] [83] [84]. However, anisotropic elasticity theory is complex and yields solutions only for specific dislocation configurations. Therefore, an approximation of anisotropic theory for the repulsion of two partial dislocations was proposed by Aerts et al. [85]. In this approximation the polycrystalline elastic constants of Equation (1-4) are replaced with effective values of the shear modulus (μ_{eff}) and Poisson's ratio (ν_{eff}):

$$\mu_{\text{eff}} = \left(C_{44}\frac{(C_{11}-C_{12})}{2}\right)^{0.5} \tag{1-5}$$

Equations (1-6) and (1-7) denote the relationship between the effective Poisson's ratio, ν_{eff}, and the single-crystal elastic constants.

$$\frac{1}{1-\nu_{eff}} = \frac{1}{3\mu_{eff}}(C + C_{12})\left[\frac{C_{44}(C-C_{12})}{C_{11}(C+C_{12}+2C_{44})}\right]^{0.5}\left(1 + 2\frac{C_{11}}{C}\right) \tag{1-6}$$

$$C = \left[\frac{1}{2}C_{11}(C_{11} + C_{12} + 2C_{44})\right]^{0.5} \tag{1-7}$$

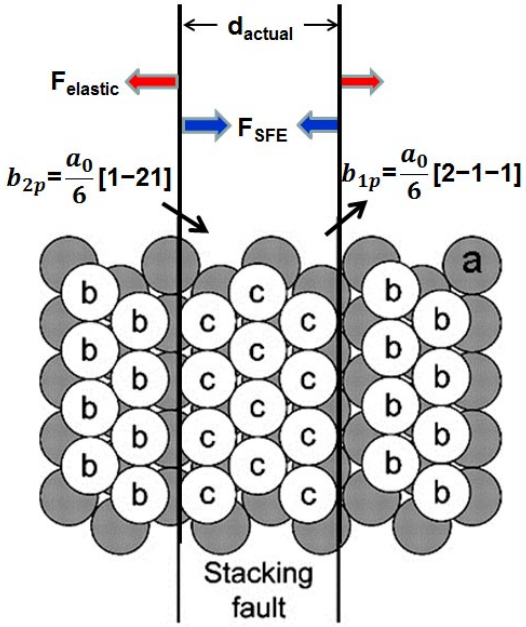

Figure 1-13 – Schematic of a dissociated dislocation of pure edge character and the resulting partial dislocations. The elastic repulsive force acting on the two partials and the restorative force due to the SFE and the Burgers vectors of each partial are labeled.

In the above analysis, the partial dislocation cores are treated as purely elastic defects, i.e. as singular Volterra type dislocations with a core width of zero. However, the core width of dislocations may not be zero and, at small partial-dislocation separations, core effects can influence SFE measurements as shown by Cockayne and Vitek [86]. The dislocation core thickness can influence the force acting between two partial dislocations and thus, their separation. The partial-dislocation separation obtained from a Peierls-type core model, $d_{Peierls}$, which accounts for core width, is related to the partial-dislocation separation of Equation (1-4), d_{actual}, by Equation (1-8) [86]:

$$d_{Peierls} = \frac{1}{2}\left(d_{actual} + \sqrt{{d_{actual}}^2 - 4\zeta^2}\right) \tag{1-8}$$

In this model, as core width increases, the repulsive force acting between the two partial dislocations decreases. Since the core width, ζ, is unknown, a reasonable approximation is twice the lattice parameter (0.724 nm), as employed by Cockayne and Vitek [86].

Bright-field (BF) TEM imaging is in many cases sufficient to resolve the inner diameter (2y) of extended nodes which typically ranges from 13 to 51 nm in low SFE austenitic steels [54] [79] [76]. However, the equilibrium separation distance of two parallel Shockley partial dislocations in low SFE alloys is usually on the order of 3-15 nm [54]. Weak-beam dark-field (WBDF) TEM imaging is necessary to resolve the individual partial dislocations. The development of the WBDF technique was first reported by Cockayne, Ray and Whelan [87] and has enabled the actual position of dislocations to be determined to within 1 nm [87]. Instructions for the use of this method are detailed in most TEM textbooks (e.g., Williams and Carter [88] and Edington [89]). The technique has been successfully used to measure SFE on pure metals with low-to-medium SFEs such as Ag (γ_{exp}=16.3±1.7 mJ m^{-2}) [90], Cu (γ_{exp}=41±9 mJ m^{-2}) [90], Cu (γ_{exp}=41 mJ m^{-2}) [91], Au (γ_{exp}=32±5 mJ m^{-2}) [92], Si (γ_{exp}=51±5 mJ m^{-2}) [93] and Ni [94]. As noted in the original reporting of this method, the separation distance of the intensity peaks of two Shockley partial dislocations will differ slightly from the separation of the actual dislocation cores. This discrepancy arises due to the asymmetry between the strain fields outside and inside the partial dislocations. Cockayne et al. [87] proposed the following relationship based on isotropic elasticity to determine the actual partial dislocation separation, d_{actual}, from the observed spacing, $d_{observed}$:

$$d_{observed} = \left(d_{actual}^2 + \frac{4}{c^2}\right)^2 \tag{1-9}$$

where $$c = -s_g \Big/ \left(\frac{g \cdot b_p}{2\pi} \left(1 + \frac{1}{2(1-\nu)} \right) \right) \quad (1\text{-}10)$$

and the deviation parameter, $$s_g = \frac{1}{2}(n-1)|g|^2\lambda \quad (1\text{-}11)$$

The term "n" is determined by the WBDF imaging conditions and is typically between 3 and 4 [88]. The wavelength of the electrons, λ, is dependent on the accelerating voltage and g is the magnitude of the reciprocal lattice vector [88]. The recommended value of s_g is ≥0.2 nm^{-1} [95].

Bampton et al. [54] measured the SFE of five different compositions of Fe-Cr-Ni austenitic steels from extended dislocation nodes and parallel partial dislocation pairs and compared the two methods. Heat treatments of 300 for 24 h, 700 for 3 h and 1050°C (slow cooled) were applied to facilitate the formation of symmetrical extended nodes and straight parallel partial dislocation pairs suitable for measurement. Post heat treatment the partial dislocation pairs were either completely constricted (no evidence of separation into two partial dislocations) or at their equilibrium partial dislocation separation. Conversely, the nodes were never completely constricted and exhibited wider scatter in the degree of extension. The authors concluded that for alloys where solute impedance forces are important the SFE is best determined by measurement of the separation of partial dislocation pairs.

SFE measurements on Fe-Mn based steels from partial dislocation separations using WBDF imaging are rare. The use of this method on Fe-Mn based alloys has been limited to two studies [15] [64]. Kim et al. [15] studied the effect of aluminum additions on the Fe-Mn-C system, publishing SFE values of 13±3 and 30±10 mJ m^{-2} for Fe-18Mn-0.6C and Fe-18Mn-0.6C-1.5Al steels, respectively, reporting an increase in SFE of 11.3 mJ m^{-2} per wt.% Al. Specimens in this

study were deformed to 2% engineering strain and the defects appear to be in close proximity to one another and the dislocations display significant curvature in some regions. Heat treatments were not applied to lessen these effects. Idrissi et al. reported a SFE of ~15 mJ m^{-2} for an Fe-20Mn-1.2C alloy [64]. In this study the dislocations also appear to be in closer proximity to each other than desired for SFE measurements. Neither study accounted for anisotropic elasticity, the difference between d_{actual} and $d_{observed}$ or dislocation core effects. The small difference in SFE values of the Fe-18Mn-0.6C and Fe-20Mn-1.2C alloy is surprising considering Volosevich et al. [80] reported an increase in SFE of ~26 mJ m^{-2} wt.% C^{-1} in Fe-12Mn-XC steel (where X is in wt.%). Based on the scarcity of SFE measurements using WBDF imaging in the literature and the technical concerns with the existing studies, additional SFE measurements of TRIP and TWIP steels are necessary to fill this gap.

1.3.2 Thermodynamic Calculation

With the use of thermodynamic modelling it is possible to calculate the SFE. A widely used method for thermodynamic SFE calculations in FCC alloys was proposed by Olson and Cohen [51] and treats the fault as n layers of hexagonal close-packed (HCP) phase separated from the face-centered cubic (FCC) matrix by two interfaces. The SFE can be calculated as:

$$\gamma_{\infty} = n\rho\left(\Delta G^{fcc\rightarrow hcp}\right) + 2\sigma^{\gamma/\varepsilon} \tag{1-12}$$

where γ_{∞} is the ideal SFE (mJ m^{-2}) of the fault (un-bounded by partial dislocations) and n is equal to 2 for an intrinsic stacking-fault (see Figure 1-7). The term $\Delta G^{fcc\rightarrow hcp}$ (mJ mol^{-1}) is the difference in Gibbs free energy of the FCC and HCP phases and is the sum of

chemical, $\Delta G_{Chem}^{fcc\rightarrow hcp}$, and magnetic contributions, $\Delta G_{Mag}^{fcc\rightarrow hcp}$. $\Delta G_{Chem}^{fcc\rightarrow hcp}$ is calculated by a sub-regular solution [3] [35] [34] [96] [97] or sub-lattice approximation [98] [17]. $\Delta G_{Mag}^{fcc\rightarrow hcp}$ arises from antiferromagnetic ordering that is present in Fe-Mn based alloys and is calculated based on the work of Hillert and Jarl [99] and Inden [100]. Its value is typically positive as antiferromagnetic ordering tends to stabilize the FCC phase [3] [35] [34] [96] [97] [98] [17]. The term $\sigma^{\gamma/\varepsilon}$ (mJ m^{-2}) is the interfacial energy between the FCC and HCP phase and ρ is the molar surface density (mol m^{-2}) of {111}, defined in Equation (1-13):

$$\rho = \frac{4}{\sqrt{3}a_{FCC}^2}\frac{1}{N_A} \tag{1-13}$$

The term N_A is Avogadro's number and a_{FCC} is the lattice parameter of the FCC phase.

This type of thermodynamic model has been used by several authors to correlate SFE values with deformation mechanisms in TRIP and TWIP steels. Allain et al. [34] studied an Fe-22Mn-0.6C wt.% steel and concluded that ε_{hcp}-martensite formation occurs for calculated SFEs below 18 mJ m^{-2} while mechanical twinning is active from 12 to 35 mJ m^{-2}. Thermodynamic SFE calculations by Saeed-Akbari et al. [101] indicate an upper limit of 20 mJ m^{-2} for strain-induced ε_{hcp}-martensite transformation in Fe-Mn-(C-Al) alloys. Nakano and Jacques [98] calculated SFE values for the Fe-Mn and Fe-Mn-C systems and correlated these with microstructural observations from other investigators, finding strain-induced ε_{hcp}-martensitic to occur at SFEs as high as 41 mJ m^{-2}. The lack of agreement between SFE value and deformation mechanism in the literature results from different thermodynamic parameters used in the calculation of $\Delta G_{Chem}^{fcc\rightarrow hcp}$ and different interfacial energies, with $\sigma^{\gamma/\varepsilon}$ varying from 9 mJ m^{-2} (Allain et al. [34]) to 16 mJ m^{-2} (Nakano and Jacques [98]). Saeed-Akbari et al. [35] utilized a value of $\sigma^{\gamma/\varepsilon}$=15 mJ m^{-2} but

acknowledged the uncertainty of this parameter in Fe-Mn based alloys, citing literature values that ranged from 5 to 27 mJ m^{-2}.

The uncertainty of the interfacial parameter in Fe-Mn based systems limits the effectiveness of thermodynamic SFE models. Olson and Cohen [51] proposed to indirectly calculate $\sigma^{\gamma/\varepsilon}$ using experimental SFE values, γ_{exp}. The term γ_{exp} includes a coherency strain energy, E_{str} (J/mol), arising from the contraction in molar volume of the HCP stacking fault relative to the FCC matrix (note: the same coherency strain energy is not accounted for in thermodynamic SFE values). The strain energy must be subtracted from the experimental SFE value as in Equation (1-14):

$$\gamma_{\infty} = \gamma_{exp} - n\rho E_{str} \tag{1-14}$$

to yield γ_{∞}. Combining Equations (1-12) and (1-14) gives:

$$\sigma^{\gamma/\varepsilon} = \frac{1}{2}\left(\gamma_{exp} - n\rho\left(E_{str} + \Delta G^{fcc\rightarrow hcp}\right)\right) \tag{1-15}$$

Both Olson and Cohen [51] and Müllner and Ferreira [57] have proposed methods to approximate E_{str}. The molar volume of the FCC and HCP phases are respectively defined in Equations (1-16) and (1-17) as:

$$V_{m,FCC} = \frac{a_{FCC}^3}{4} N_A \tag{1-16}$$

and

$$V_{m,HCP} = \frac{\sqrt{3}}{4} a_{HCP}^2 c_{HCP} N_A \tag{1-17}$$

where a_{FCC}, a_{HCP} and c_{HCP} are the lattice parameters of the FCC and HCP phases. The volumetric strain (*VS*) due to volume change from FCC to HCP phase is defined as:

$$VS = \frac{V_{m,HCP} - V_{m,FCC}}{V_{m,FCC}} \tag{1-18}$$

The strain (ε_{33}) corresponding to the contraction normal to the close packed planes of the HCP structure relative to the FCC matrix is defined as:

$$\varepsilon_{33} = (c_{HCP} - c_{FCC})/c_{FCC} \tag{1-19}$$

The terms c_{FCC} and c_{HCP} are twice the CPP spacing in the FCC and HCP structures, respectively. The strain terms ε_{11} and ε_{22} correspond to the contraction along <1-210> relative to <1-10> (close packed directions) and <1-100> relative to <11-2>, respectively, and are calculated similarly to ε_{33} (Equation (1-19)) as a function of the lattice parameters. Olson and Cohen [51] considered the strain energy term to be the sum of a dilatation energy, E_{dil}, and a shear energy, E_{sh}:

$$E_{str} = E_{dil} + E_{sh} \tag{1-20}$$

where

$$E_{dil} = \frac{2(1+\nu)}{9(1-\nu)} \mu V_{m,FCC} (VS)^2 \tag{1-21}$$

and

$$E_{sh} = \eta V_{m,FCC} 2\mu \left\{ \frac{1}{6} [(\varepsilon_{11} - \varepsilon_{22})^2 + (\varepsilon_{22} - \varepsilon_{33})^2 + (\varepsilon_{33} - \varepsilon_{11})^2] + \varepsilon_{12}^2 + \varepsilon_{23}^2 + \varepsilon_{13}^2 \right\} \tag{1-22}$$

The terms ν and μ represent the austenite phase polycrystalline Poisson's ratio and shear modulus, respectively; and η is the accommodation factor further described below. Equations (1-21) and (1-22) are based on the work of Eshelby [102] for determining the strain energy of an inclusion which undergoes a shape change within an infinite matrix. The Olson and Cohen model does not consider the interaction energy between the contracted stacking fault and the partial dislocations. However, Müllner and Ferreira [57] modeled the strain field generated by two parallel partial dislocations and a contracted stacking-fault using Somigliana dislocations to

compute the total energy including the interaction components. The interaction energy components involving the two Shockley partials were found to be small or vanishing compared to other components of the coherency strain energy. The Müllner and Ferreira model assumes that the coherency strain is volume preserving (i.e., VS=0), The strain energy (in units of energy per area) under the assumption that $d_{actual}>>(c_{HCP}/2)$ and the volume of the stacking fault remains constant is [57]:

$$E_{str} = \frac{n\mu c_{HCP}\varepsilon_{33}^2}{8(1-\nu)} \quad (1\text{-}23)$$

where n is 2 for an intrinsic stacking fault.

1.4 Elastic Properties of Fe-Mn based steels

Single-crystal elastic stiffness constants are necessary to make accurate SFE measurements in materials like austenitic steels that exhibit significant elastic anisotropy (see section 1.5.1.2). Austenitic stainless [103] and binary Fe-Mn [104] [105] [106] steels display anisotropy factors $2C_{44}/(C_{11}-C_{12})$ from 3.3 to 3.9. The role of elastic anisotropy in SFE measurements has been overlooked in the few studies in the literature [15] [64] partly due to the lack of available experimental single-crystal elastic constants for TRIP and TWIP steels. In binary Fe-Mn alloys, antiferromagnetic (AFM) ordering influences the elastic properties. Unlike most austenitic steels, Fe-Mn based alloys undergo an AFM to paramagnetic (PM) transition at Néel temperatures above 200K [4]. Lenkkeri [105] and Cankurtaran et al. [106] measured C_{11}, C_{12} and C_{44} of binary Fe-38.8/40Mn at.% single-crystal alloys as a function of temperature using an ultrasonic pulse overlap technique. Antiferromagnetic ordering suppresses the tetragonal shear modulus (C_{11}-

C_{12})/2, the resistance to shear on {110} in <1-10>. The shear term (C_{11}-C_{12})/2 increases uniformly with decreasing temperature from 800K to the Néel transition (~478K), then undergoes a step-like reduction, and continues to increase linearly to 200K in the AFM regime at a significantly reduced slope as observed in Figure 1-14. The normal shear modulus C_{44}, the resistance to shear on {100} in <010>, is relatively unaffected, displaying a slight increase due to the onset of AFM ordering. Correspondingly, the anisotropy ratio decreases with temperature to the Néel transition and then increases with further reductions in temperature in the AFM regime.

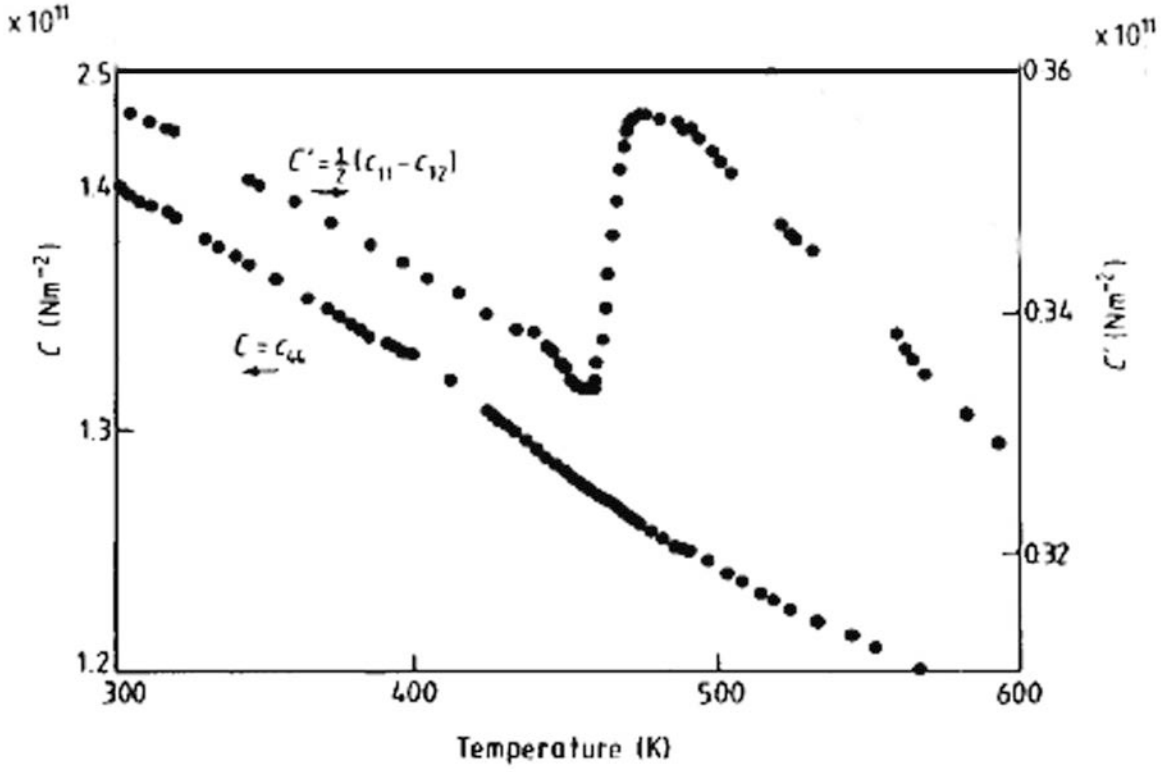

Figure 1-14 – Temperature dependence of the elastic constants C_{44} and (C_{11}-C_{12})/2 for an Fe-38.5 at.% alloy (image modified from Lenkerri [105])

A binary Fe-30Mn at.% alloy, with a Néel temperature of 412K, displays similar trends in the elastic behavior due to antiferromagnetic ordering [104]. In context with Fe-38.5/40Mn alloys, reducing the Mn content decreases C_{44}, the anisotropy ratio, and increases the bulk modulus, regardless of magnetic state. A reduction in Mn content had little effect on $(C_{11}-C_{12})/2$ at room temperature in the AFM state. However, the step-like reduction in $(C_{11}-C_{12})/2$ occurring at the Néel temperature increases with decreasing Mn content [107].

For TRIP/TWIP steels with Mn contents ranging from 18 to 28 wt.%, AFM ordering causes anomalies in the elastic properties closer to room temperature. Allain [108] observed a fluctuation in the polycrystalline shear modulus of ~20% at a Néel temperature of 321K in a Fe-22Mn-0.6C wt.% alloy. Similar anomalies occur below room temperature in Fe-18Mn-1.5/2.5Al-0.6C wt.% alloys, and become less intense with increases in Al content [48]. Music et al. [109] investigated the effect of Mn content on binary Fe-Mn alloys with ab-initio simulations, finding C_{44} to be relatively unaffected by Mn additions, while C_{11} and C_{12} decreased by 25.6 and 39.2%, respectively, with increases of Mn from 5 to 40 at.%. Gebhardt et al. [110] studied the elastic properties of binary Fe-Mn polycrystalline thin films with nanoindentation, finding the bulk modulus to decrease from 143 GPa to 105 GPa as the Mn content increases from 23 to 39 at.%. In a subsequent study, Gebhardt et al. [111] studied the individual effect of both Al and Si on the elastic properties of Fe-Mn alloys with nanoindentation and ab-initio calculations. In this study, ab-initio calculations indicated that the individual additions of both Al and Si to binary Fe-Mn alloys resulted in a significant increase in the single-crystal anisotropy. The bulk elastic properties of the Fe-Mn-C system have also been studied by nanoindentation and ab-initio

calculations [112]. However, the elastic anisotropy of high-Mn TRIP and TWIP steels has not been thoroughly characterized experimentally.

1.5 Goals and Objectives of Current Work

The previous sections illustrate several gaps in the knowledge of TRIP and TWIP steels that must be overcome in order to improve the understanding and further the development of these materials. This research will focus on several of these areas, including:

- Determining the optimal thermo-mechanical processing routes of specimens and best TEM methods for measuring the SFE to overcome current weaknesses in experimental procedures. Of the few SFE measurements of TWIP steels available in the literature [15] [64], the experimental procedures used in these studies are lacking and several areas for improvement are identified in section 1.3.1.2. New procedures and methods will be developed and evaluated to improve the accuracy of SFE measurements.
- Measuring the single-crystal elastic constants of Fe-22/25/28Mn-3Al-3Si alloys for use in experimental SFE measurements. The magnitude of the elastic repulsive force acting between two partial dislocations, which is needed to determine the SFE, is a function of the dislocation character angle and the three single-crystal elastic stiffness constants, C_{11}, C_{12} and C_{44} (see Equations 1-4 to 1-7) [82] [83] [85] [113]. Currently, there are no experimental values of single-crystal elastic constants in the literature for high-Mn TRIP/TWIP steels. Measurement of these elastic constants will allow the use of anisotropic elasticity theory and improve the accuracy of SFE measurements.

- Determining the SFE and FCC/HCP interfacial energy of three Fe-22/25/28Mn-3Al-3Si alloys. The development of quantitative relationships between the SFE, deformation mechanisms and mechanical properties is hindered by limited experimental SFE measurements and the uncertainty of $\sigma^{\gamma/\varepsilon}$ (which is used in thermodynamic calculations of the SFE). In most TRIP/TWIP steels $\sigma^{\gamma/\varepsilon}$ is the largest component of the SFE, and the value of this parameter for Fe-Mn based steels is thought to be in a range of ~5 to 27 mJ m^{-2} [35] (see section 1.3.2). Therefore, a major objective of this work will be to measure the SFE of three Fe-22/25/28%Mn-3Al-3Si alloys and use a combined theoretical and experimental approach to determine reliable values of $\sigma^{\gamma/\varepsilon}$ for these materials, thereby enabling more accurate calculation of the SFE.
- Develop of quantitative relationships between the SFE, deformation mechanisms and mechanical properties. These relationships will form design considerations for future TRIP/TWIP steels that will enhance the ability to optimize the properties of the materials prior to development.

CHAPTER 2

EXPERIMENTAL PROCEDURE

2.1 Materials

Three alloys were induction melted in an argon atmosphere and cast into ingots. The compositions are listed in Table 2-1. The steels with 25 and 28%Mn were fully austenitic, while the alloy with 22%Mn contained a small amount of ordered BCC phase (<1%). As-cast ingots were thermo-mechanically processed by hot rolling at 1100ºC to produce strips of 3 mm thickness and subsequently by cold rolling to 1.5 mm thickness. The resulting sheet was recrystallized at 800, 900 and 1000^{o}C for 30 min in an air atmosphere yielding a microstructure with equiaxed grains. Optical micrographs of the microstructures after cold rolling, and recrystallization at 800, 900 and 1000^{o}C for the 25%Mn alloy are presented in Figure 2-1. The grain sizes are ~16, 21 and 62 μm in diameter for recrystallization temperature 800, 900 and 1000^{o}C, respectively. The grain size was measured with the circle intercept method in accordance with ASTM E112 (measurements are shown in Figure 2-1 for the 25%Mn alloy recrystallized at 900^{o}C for 30 minutes). No significant differences were noted in the grain sizes for the different compositions. Sub-sized flat tensile specimens with a 20 mm gauge length and 5 mm width were cut from the sheet in the direction parallel to the rolling direction using electro-discharge machining (EDM) and were used for mechanical testing and microstructural characterization. An image of a sub-sized tensile specimen is shown in Figure 2-2. In addition, large tensile specimens with a 12.5 mm width, 75 mm reduced section length and 50 mm gauge length (initial extensometer length) were also cut from the sheet in the direction parallel to the

rolling direction using EDM. These specimens were used with an extensometer for some testing conditions in order to remove the elastic strain associated with the tensile testing machine.

Table 2-1 – Chemical compositions of the steels in wt.% unless otherwise specified.

Designation	Material	Mn	Al	Si	C	O (ppm)	Fe
22%Mn	Fe-22Mn-3Al-3Si	22.2	2.76	2.92	0.0093	<5	Bal.
25%Mn	Fe-25Mn-3Al-3Si	24.7	2.66	2.95	0.0053	<5	Bal.
28%Mn	Fe-28Mn-3Al-3Si	27.5	2.74	2.89	0.0071	<5	Bal.

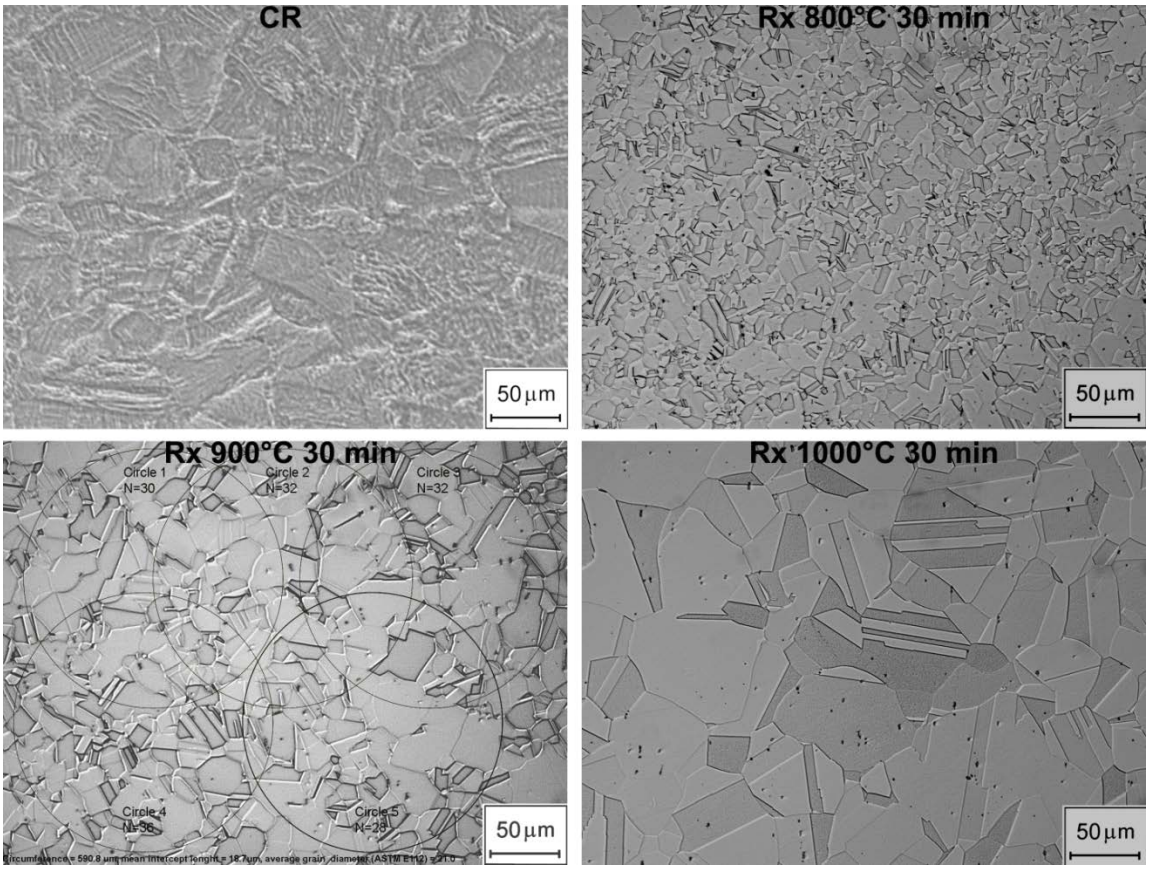

Figure 2-1 - Cold rolled (CR) and recrystallized (Rx) microstructures at 800°C, 900°C and 1000°C for 30 minutes. The grain size calculation is shown for the material recrystallized at 900°C.

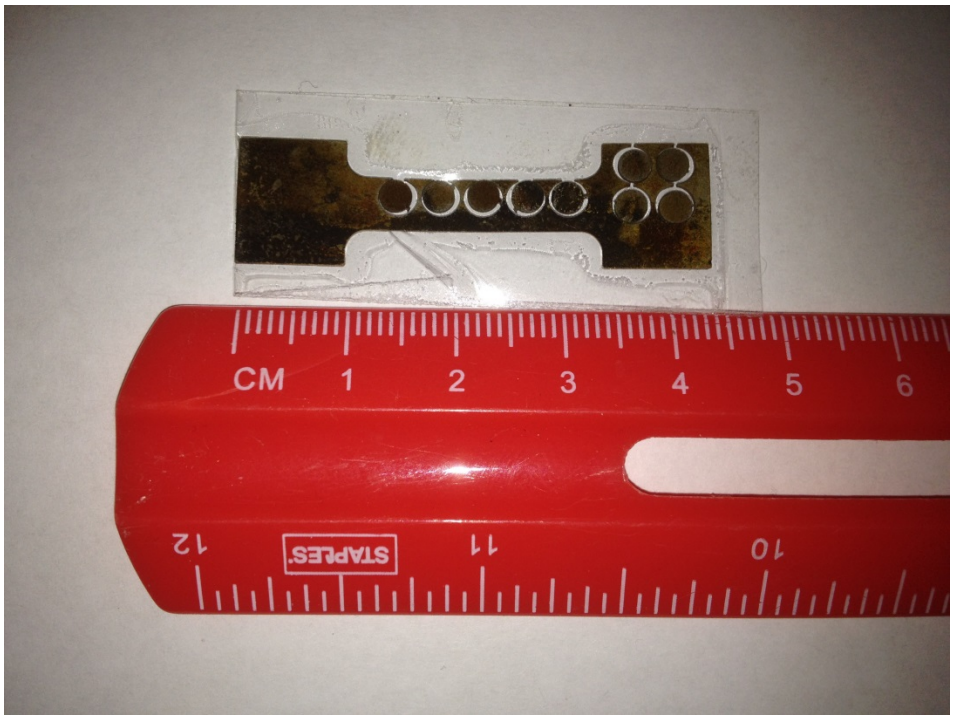

Figure 2-2 - – Tensile specimen deformed to the yield point (YP) with 3-mm-diameter disks cut from the gage length and shoulder using electo-discharge machining (EDM).

2.2 Mechanical Testing

The sub-sized specimens of the 22, 25 and 28%Mn alloys were strained in tension at RT, 100, 200, 300 and 400°C at a rate of 4×10^{-4} s^{-1}. The initial gauge lengths of the sub-sized tensile specimens was 20 mm and the cross-sectional area was measured for each specimen prior to testing to account for small variations in sheet thickness. The tensile-test machine provides values of load and displacement which are used in conjunction with the sample geometry to determine the engineering and true stress/strain. The instantaneous cross-sectional area, calculated as function of displacement assuming the sample volume remains constant during tensile testing, is used to determine the true stress. Therefore, the true stress/strain values are only valid up to maximum uniform elongation (just before the sample begins to neck). The point

of maximum uniform elongation is determined from the Considère criterion (the point at which the true stress and strain-hardening rate are equal). The displacement data from the tensile machine include elastic displacement from the machine and both elastic and plastic displacement of the sample being tested. The influence of elastic deformation of the machine is partially mitigated by only considering the plastic deformation of the sample in the present work (i.e., plastic strain or plastic true strain). However, elastic strain from the machine cannot be entirely mitigated without the use of an extensometer and the values of strain reported in the present work will slightly overestimate the actual value. Therefore, comparisons of the elongation data should only be made between the present materials or ones with similar test configurations. Tests at RT and 400°C were interrupted at 0.03, 0.1, 0.18, 0.34, 0.44 and 0.47 plastic true strain (i.e., the strain was measured from the beginning of plastic deformation) for microstructural characterization by optical microscopy (OM), x-ray diffraction (XRD) and TEM. Several large tensile specimens were deformed and the displacement was measured using a high resolution macro extensometer from Zwick. The arms of this extensometer are in direct mechanical contact with both sides of the specimen via knife edges to compensate for superimposed bending strains. The extensometer displacement data (along with the load data) were used in the calculation of Young's modulus.

2.3 Optical Microscopy

Specimens for OM were prepared by standard metallographic procedures. Manual grinding was accomplished using successively finer SiC abrasive paper (240, 600, 1000 then 2400 grit) with a

constant supply of water to lubricate and remove grinding debris. The sample was placed in ethanol immediately after grinding and ultrasonically cleaned. An automatic system was used to polish the samples. The intermediate polishing steps were carried out with 3 μm disk/diamond paste with 25 N load followed by a 1 μm disk (MD Nap from Struers)/diamond paste with 20 N load. The sample was polished for ~5 minutes and a constant drip of blue polishing lubricant was used for each step. At the completion of each step, the sample was immediately rinsed with water, sprayed with ethanol, immersed in ethanol and ultrasonically cleaned (the samples must be cleaned and immersed in ethanol quickly to prevent corrosion). Low loads were used during this process, and successively decreased from 25 to 10 N for the final polish. The final polish utilized a suspension of 0.05 μm colloidal silica for chemical-mechanical polishing (CMP) and 10 N load for 5 minutes to ensure a flat surface with minimal deformation. The CMP was mixed with water-based (oil-free) soap for lubricant (note: blue lubricant used in the previous steps is not used here as it causes conglomeration of the colloidal silica particles). In the last 30 seconds of the final polish water is used to flush the sample. The sample is immediately removed and cleaned with ethanol in an ultrasonic cleaner. If etching was required, a 10% Nital (10/90% nitric acid/methanol) solution was used for ~30 seconds. The sample was then immersed in ethanol and cleaned ultrasonically before being blown dry.

2.4 Nanoindentation

Specimens of the 22 and 25%Mn alloys recrystallized at 1000^{o}C (largest grain size) were used for nanoindentation. The samples were polished using the same procedure as specimens for optical microscopy. An average surface area roughness value, S_a, of 3 nm within grains was

measured via digital holographic microscopy (DHM). The samples were marked with indents from a microhardeness indenter in order to define an area. The orientations of grains at the surface of the defined area were characterized with a Zeiss scanning electron microscope (SEM) equipped with electron back-scatter diffraction (EBSD) orientation image mapping (OIM) capability. A grain orientation map (OM), along with a SEM image of an indented grain oriented in <101>, is shown in Figure 2-3, for the Fe-25Mn-3Al-3Si alloy.

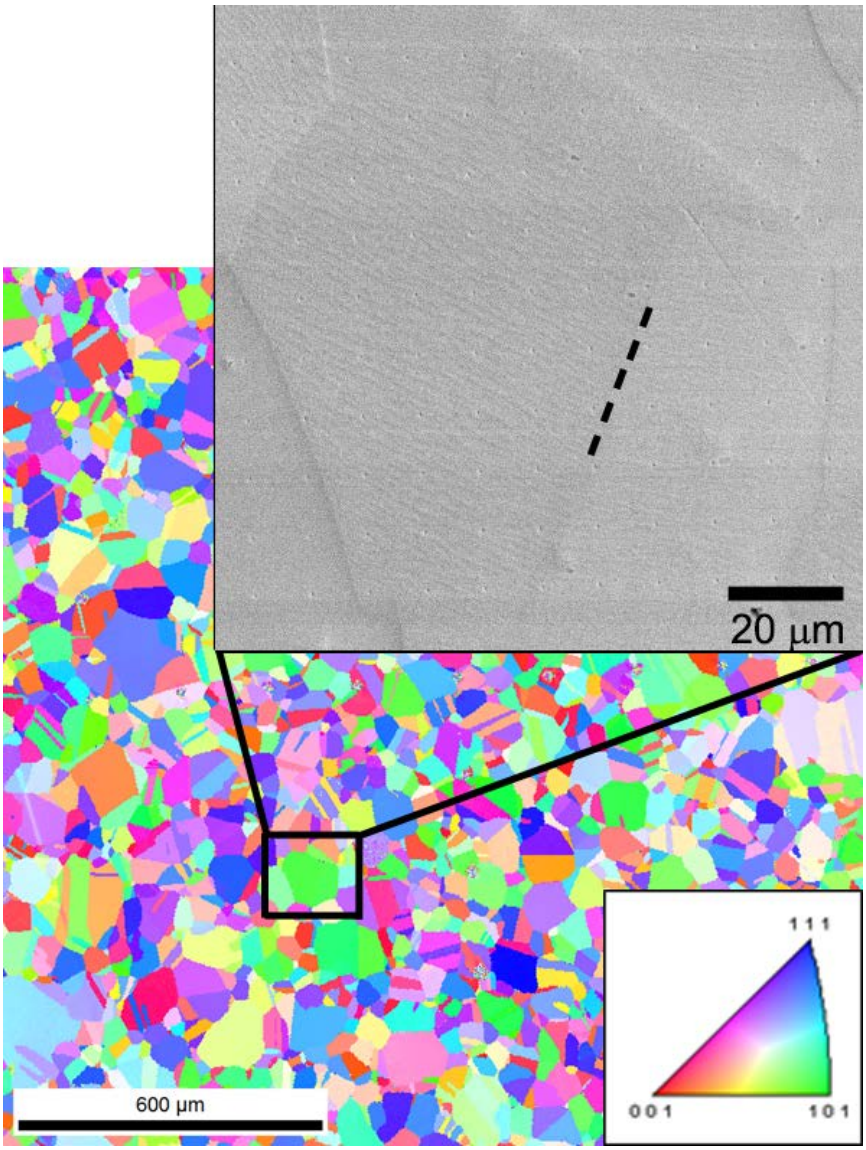

Figure 2-3 - Grain OM of the Fe-25Mn-3Al-3Si sample recrystallized at 1000°C for 0.5 h, with SEM image of an indented grain in the <101> orientation. The dashed line marks the boundary of an annealing twin plane perpendicular to the surface.

Indentation experiments were performed using an Ubi indenter (Hysitron, Minneapolis, USA) equipped with a diamond Berkovich indenter tip and working in load controlled mode. The area function of the tip was calibrated by indenting in a material of known modulus (fused quartz, 72 GPa). The Ubi indenter includes an optical microscope which was used to identify specific grains (within the previously mapped area) for indentation (note: prior etching of the grain boundaries facilitated finding the proper grains for nanoindentation). Larger grains with orientations closest to the <100>, <110> and <111> orientations were selected for indentation. Mechanical properties are extracted from the unloading curve using the Oliver-Pharr method [114]. The load-time profile of each indentation consisted of a 5 second loading, 2 second pause and 5 second unloading phase. In order to minimize interaction between indents and grain boundaries, they were spaced a minimum of 10 μm apart or from grain boundaries as can be seen in the SEM image from Figure 2-3.

2.5 Stacking Fault Energy Measurements

Disks 3 mm in diameter were cut from the gauge length of deformed samples using EDM. The 3-mm disks were ground to 100 μm thickness (final grit should be 600 or finer) and then jet electro-polished to electron transparency with a TenuPol-5 using a solution of 70% methanol and 30% nitric acid at -30°C and 15 V. Partial dislocations were analyzed with a Philips CM20T TEM operating at 200 kV and equipped with an Advanced Microscopy Techniques XR42HTVcharge-coupled device (CCD) camera.

Measurements of Shockley partial-dislocation separations were made with a beam direction near the [111] zone on defects in the (111) habit plane using <-220> type g-vectors. Bright-field (BF) and WBDF imaging modes were employed with WBDF diffracting conditions set at g(3g) or g(4g) with no non-systematic reflections excited. The g(3g) configuration results in a deviation parameter s_g=0.15 nm^{-1} and w= $\xi_g s_g$=12.4 where ξ_g is the extinction distance. The value of s_g in the g(3g) configuration is slightly less than the recommended value of 0.2 nm^{-1} [95] and results in slightly larger-than-ideal image widths. For partial-dislocation separations below ~4 nm, as in the 28%Mn alloy, the g(4g) configuration (s_g=0.23 nm^{-1}, w= $\xi_g s_g$=18.5) was utilized to improve resolution of the partial dislocations. Measurements were made every 5-10 nm along the length of long, straight sections of isolated dislocations in areas not significantly affected by image forces and constrictions. The number of separation measurements per partial dislocation pair ranged from 7 to 70. Since the strain fields outside and between partial dislocations are asymmetrical, the intensity peaks are not equidistant from their respective dislocation cores and a correction is applied to determine the actual partial-dislocation spacing, d_{actual} [87] [88]. An average d_{actual} and standard deviation of the measurements were obtained for each partial-dislocation pair. Inside-outside contrast techniques (reversing the g-vector) were additionally applied to differentiate partial dislocations from dipoles. The total dislocation character angle, β, was determined from Burgers vector analysis on the partial dislocation Burgers vectors (b_p) in WBDF imaging mode. For Shockley partial dislocations in the [111]/(111) zone/habit plane configuration, $|g \cdot b_p|$ values are 1 or 0 and $|g \cdot b_p| = 1$ for both partials at only one g-vector. When the latter condition is achieved the total Burgers vector is parallel to the g-vector and the angle it makes with the dislocation line vector is the total dislocation character angle. The habit plane

was confirmed by stereographic analysis from BF images of the dislocation taken at three different orientations.

2.6 X-Ray Diffraction

Measurements of lattice parameters utilized a Bruker AXS D8 diffractometer equipped with a Co X-ray tube, Goebel mirror optics and a LynxEye Linear Position Sensitive Detector for ultra-fast XRD measurements. A current of 30 mA and a voltage of 40 kV were employed as tube settings. Operational conditions were selected to obtain XRD profiles of sufficient quality: namely, optimal counting statistics, narrow peaks and detection of small diffraction peaks of minor phases. The XRD data were collected over a 2θ range of 30 -120º with a step size of 0.02º.

For the application of the Rietveld refinement, instrument functions were empirically parameterised from the profile shape analysis measured under the same conditions for an AISI Type 316 stainless steel standard prepared by hot isostatic pressing. In this study, version 4.2 of the Rietveld analysis program TOPAS (Bruker AXS) was used for the XRD data refinement. The refinement protocol included the background, zero displacement, scale factors, peak width, unit cell parameters and texture parameters. The room-temperature structures used in the refinement were ferrite, austenite and ε_{hcp}-iron. The quality and reliability of the Rietveld analysis was quantified by the corresponding figures of merit: the weighted summation of the residual of the least-squares fit, $R_{wp,}$ the statistically expected least-squares fit, R_{exp}, the profile

residual, R_p, and the goodness of fit (sometimes referred to as chi-squared), GoF. Since GoF = R_{wp} / R_{exp}, a GoF = 1.0 means a perfect fitting.

CHAPTER 3

OPTIMAL METHODS FOR STACKING-FAULT ENERGY MEASUREMENTS BY TRANSMISSION ELECTRON MICROSCOPY

This chapter is heavily based on published papers [115] [116] [117] and the results are limited to the Fe-25Mn -3Al-3Si alloy. The specimens deformed to the YP contained low defect density and large stacking-faults were absent. Specimens deformed to 1.5% displayed a higher defect density with many large non-equilibrium stacking-faults as shown in Figure 3-1a. The majority of these faults were intrinsic in nature as determined by traditional diffraction-contrast methods (e.g., +/-g, BF/DF, Williams and Carter [88]) and depicted in the dark-field image in Figure 3-1b. The stacking-faults are thin sheets of ε-martensite. Brooks et al. have estimated the supplementary displacement that occurs in addition to the expected $a_o/3<111>$ at stacking faults in austenitic Fe-Cr-Ni steels and argued that a single intrinsic stacking fault is a ε-martensite embryo [52] [53]. Idrissi et al. [118] have postulated intrinsic stacking-faults as a precursor for mechanical twinning and extrinsic stacking-faults as precursor for the formation of strain-induced e-martensite laths. In that work it was shown that primarily extrinsic stacking-faults formed during room temperature deformation of a similar Fe-19.7Mn-3.1Al-2.9Si alloy. This result may indicate that Mn content has a strong influence on the nature of the stacking-faults in these alloys but extrinsic faults are unusual products of deformation and the results of Idrissi et al. [118] may warrant further scrutiny. At 1.5% strain, dislocation-dislocation interaction was observed and some dislocations displayed curvature beyond what is acceptable for quantitative SFE measurements. Extended-dislocation nodes were not observed in the as-deformed specimens.

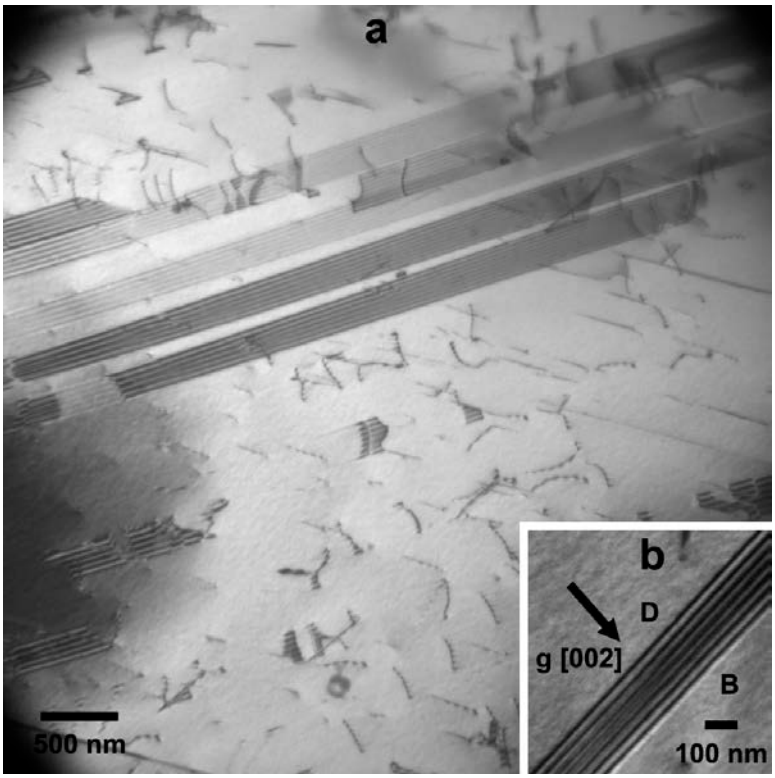

Figure 3-1 (a) Microstructure in a Fe-25Mn-3Al-3Si specimen deformed 1.5% and inset (b) a dark-field image displaying the intrinsic nature of one of the stacking faults (D and B indicate the positions of the dark and bright fringes, respectively).

The microstructure did not show a substantial change in defect distribution or density after annealing at 400ºC for 70h except for significantly fewer wide stacking-faults as shown in Figure 3-2. Most dislocations continued to display curvature and appeared to be completely constricted when viewed in WBDF mode. Extended nodes did not form during this heat treatment.

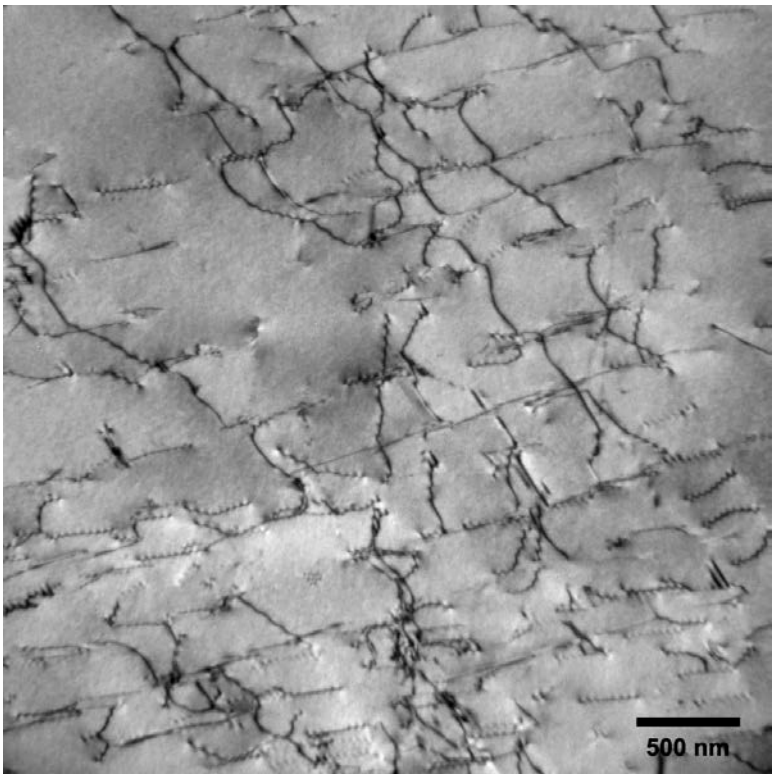

Figure 3-2 Microstructure in a Fe-25Mn-3Al-3Si specimen deformed 1.5% and heat treated at 400 °C for 70 h.

In specimens heat treated at 650 and 700°C the dislocation density was reduced and isolated dislocations were straighter. Wide stacking-faults were rarely observed and the majority of dislocations were constricted (displayed no evidence of separation) when viewed in WBDF mode. The annealing behavior of the Fe-24.7Mn-2.66Al-2.92Si alloy is different from that reported for austenitic Fe-Ni-Cr steel, for which nodes have been observed after a treatment at temperatures as low as 300ºC [54]. In current work, extended nodes did not form during the heat treatment at 400ºC. Annealing at 650ºC or higher is required in order to provide sufficient thermal activation to form nodes, but only in limited quantities. Nodes typically formed in arrays as shown in Figures 3-3a and b for the specimens annealed at 650°C for 6 h and 70 h,

respectively. Isolated nodes preferable for SFE determination were rarely observed. The majority of nodes displayed asymmetric character as typified by Figure 3-3a.

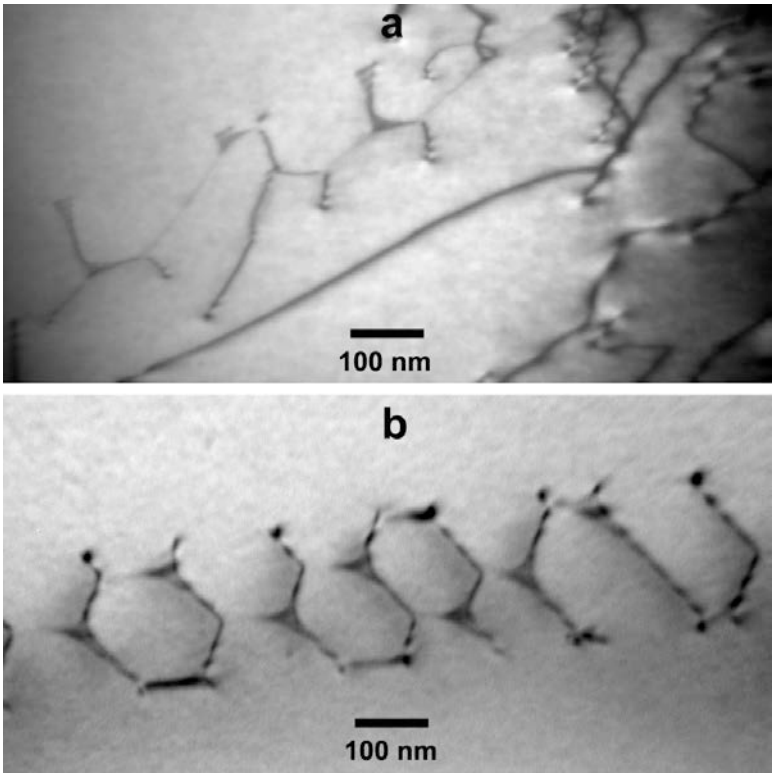

Figure 3-3 - Arrays of dislocation nodes formed in specimens after (a) heat treatment at 650 °C for 6 h and (b) heat treatment at 650 °C for 70 h.

Measurement of SFE from partial-dislocation separations proved more reliable than from nodes. Figures 3-4a and b show a BF image and the corresponding WBDF image of typical partial dislocations observed in a specimen deformed to the YP. The dislocation spacing is uniform and does not present any constrictions whereas specimens deformed to 1.5% generally displayed constrictions due to the greater likelihood of dislocation interactions from the increased dislocation density. Dislocations suitable for measurement were only observed in samples deformed to the YP and those deformed 1.5% and annealed at 650°C for 70 h.

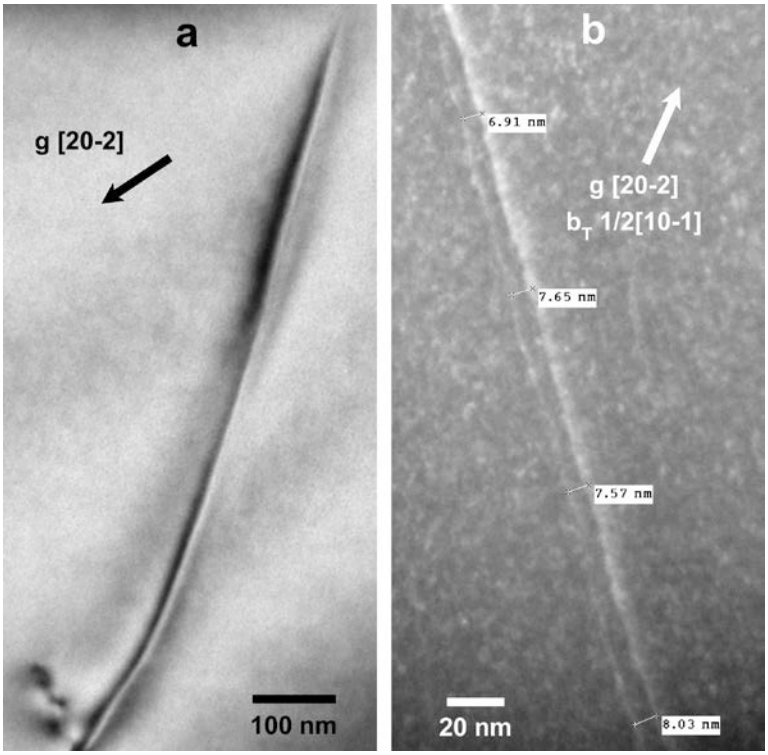

Figure 3-4 - BF image (a) and WBDF image (b) of a dissociated dislocation in a sample deformed to the YP. The reciprocal lattice vectors and total Burgers vector are defined as g and b_T, respectively.

Samples deformed 1.5% generally required heat treatments to reduce the incidence of anomalously wide stacking-faults, as observed in Figure 3-1, and to straighten dislocations. Conversely, the heat treatments also appeared to have the undesirable effect that the majority of observed dislocations failed to dissociate upon cooling. The impedance to dissociation in the Fe-Mn-Al-Si system is more pronounced than that for Fe-Ni-Cr steels, for which many dislocations are able to dissociate after similar heat treatment [54]. However, consistent with the work on Fe-Ni-Cr steels [54], heat treatments of 650°C did not appear to affect the final equilibrium spacing of dislocations that were able to dissociate. Deforming samples only to the YP reduced the

internal strain in each grain and the incidence of anomalously wide stacking-faults which led to a greater number of partial-dislocations suitable for measurement.

Stacking-fault energy determination by the node method is extremely challenging in this alloy. Significant impedance to node formation, in comparison with the Fe-Ni-Cr steels [54], must be overcome with higher-temperature heat treatment (≥650°C). Even at high temperatures node formation was limited. The heat treatment can have undesirable effects such as interstitial and substitutional solute pinning and segregation. The SFE measured from the node method on Fe-Ni-Cr steels revealed wide scatter within specific heat treatments and a noticeably higher apparent SFE in specimens that had been heat treated at higher temperatures [54]. Prior work on an Fe-20Mn-4Cr-0.5C alloy showed irreversible effects in node size when cooling from 390 to 300K which was attributed to interstitial carbon pinning [81]. Similar effects were observed in Fe-Cr-Ni alloys and attributed to atmospheres of substitution solutes that formed around the node arms at elevated temperatures [77]. In the present work, a wide range of node sizes were observed indicating that the same effects related to the heat treatments observed in other studies may be present here as well which precludes the application of theories assuming isolated, symmetric nodes [72] [73] [74] [75].

3.1 Conclusions

The following conclusions were drawn from this work:

1. The thermo-mechanical treatments utilized to prepare the tensile samples, coupled with tensile deformation to only the YP, resulted in the best microstructure (optimal grain size with minimal internal strain) for measuring partial-dislocation separations.

2. Determination of the SFE by TEM is best performed on this alloy by measuring partial-dislocation separation using WBDF imaging techniques. Extended nodes that formed in this alloy appeared asymmetric with varying sizes and were rarely isolated, precluding any meaningful measurements.

CHAPTER 4

DETERMINATION OF SINGLE-CRYSTAL ELASTIC CONSTANTS FROM NANOINDENTATION

This chapter is heavily based on published papers [119] [120] although the relevant introductory material and experimental procedures are covered in chapters 1 and 2.

4.1 Determination of Young's Modulus from Tensile Testing

Young's modulus is obtained from the slope of the elastic region of the stress-strain curve, as depicted in Figure 4-1. Five tensile tests on each material produced mean values of 179 ±3 and 179 ±5 GPa for the 22 and 25%Mn alloys respectively, with error constituting the standard deviation of the measurements. Results of EBSD OIM revealed a texture index (TI) of 1.05, indicating crystallographic texture is not significantly influencing the bulk elastic properties.

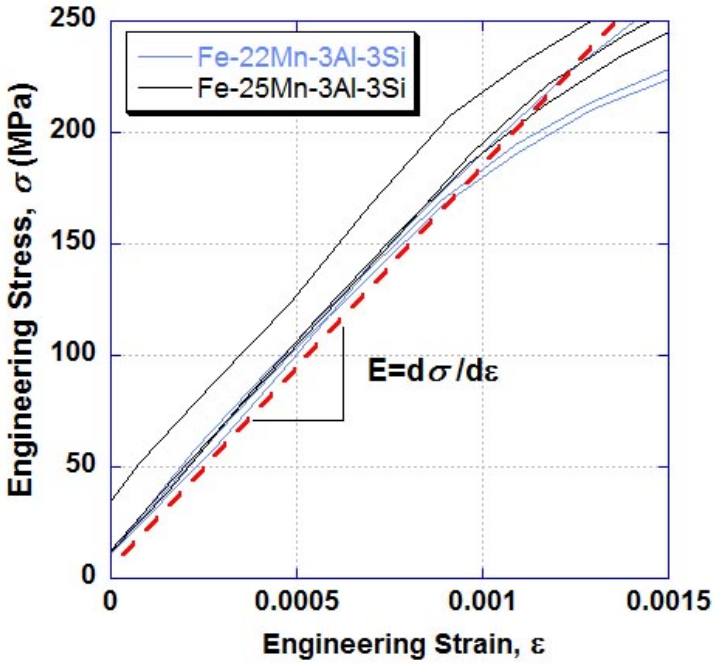

Figure 4-1 - The elastic portion of the engineering stress(s) vs. strain(ε) curves for six tensile tests of the Fe–22/25Mn–3Al–3Si alloys. The red dashed line represents the linear fit to the elastic region, the slope of which is Young's modulus(E).

The values of Young's modulus are similar to those reported for other compositions of TWIP steel (175 for Fe-18Mn-0.6C and 174 GPa for Fe-18Mn-0.6C-1.5Al), which were measured by room temperature resonant frequency of samples under torsional vibration [15]. The high-Mn steels in this research and those in [15] exhibit E values ~10% less than the typical ~200 GPa for type 304 Fe-Cr-Ni austenitic steels [121]. Several authors report that alloying Mn with Fe-Cr-Ni steel decreases all bulk elastic constants, including Poisson's ratio. In a study of Fe-Cr-Ni-Mn alloys, Young's modulus values ranging from 190 to 200 GPa decreased with additions of Mn [122]. Ledbetter [123] showed that additions of up to 6 wt.% Mn in an Fe-Cr-Ni stainless steel resulted in a ~2% decrease in Young's modulus.

4.2 Nanoindentation

The reduced modulus, M_r, is determined from the unloading portion of the load-displacement curves in accordance with the Oliver-Pharr method [114]. A series of ten load-displacement curves are displayed in Figure 4-2 for a grain oriented near <111> in the Fe-25Mn-3Al-3Si alloy. The slope of the unloading curve at maximum depth, dP/dh, is related to the projected indenter contact area, A, and M_r by Equation (4-1).

$$S = \frac{dP}{dh} = \frac{2\sqrt{A}}{\sqrt{\pi}} \frac{M_r}{1} \tag{4-1}$$

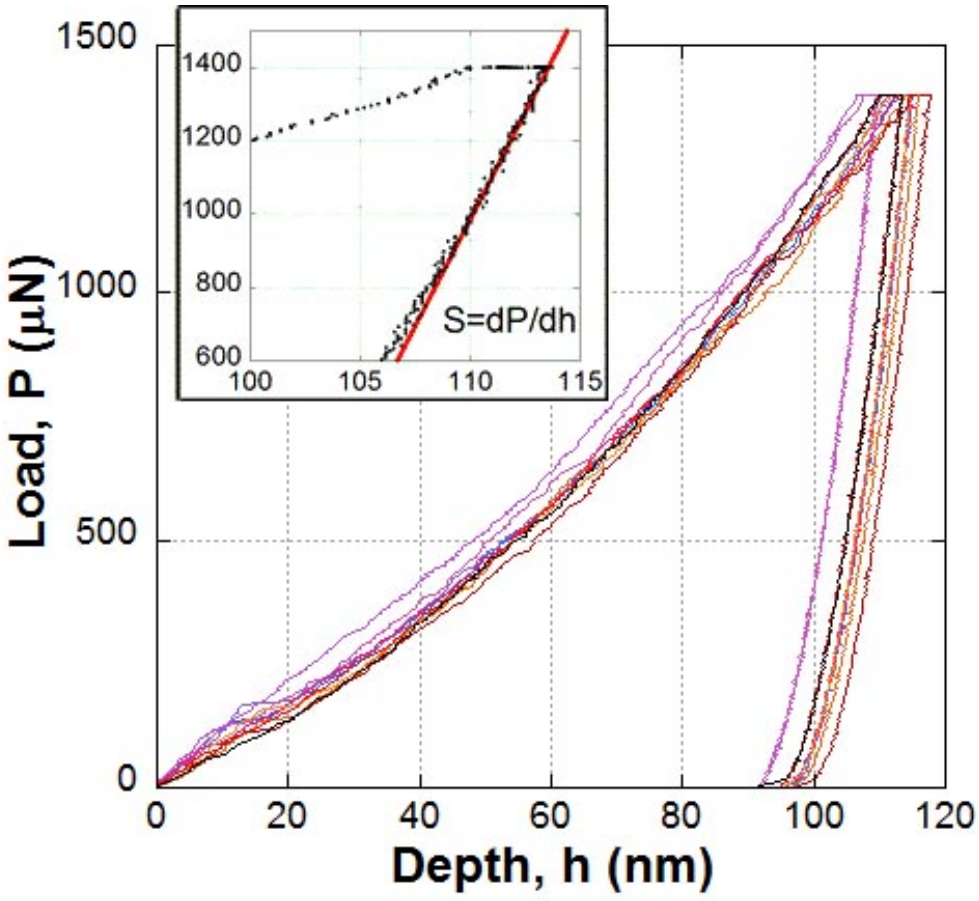

Figure 4-2 - Load vs. depth curves from ten individual indentations in a grain with surface normal in the <111> direction in the Fe–25Mn–3Al–3Si alloy. The stiffness, S, is measured from the slope of the unloading portion of the curve at maximum depth as depicted in the inset.

Vlassak and Nix [124] [125] confirmed that, for elastically anisotropic materials and axisymmetric indenters, the reduced modulus is related to the orientation dependent indentation modulus, M_{hkl}, by Equation (4-2).

$$\frac{1}{M_r} = \left(\frac{1}{M_{(hkl)}}\right) + \left(\frac{1-\nu_i^2}{E_i}\right) \tag{4-2}$$

where E_i and ν_i are the Young's modulus and Poisson's ratio of the indenter tip and are equal to 1140 GPa and 0.07 respectively. The average values of M_{111}, M_{110}, and M_{100} for the Fe-(22/25) Mn-3Al-3Si alloys are 196.6/195.4/177.9 and 198.2/197.0/178.4 GPa, respectively, and are displayed in Figure 4-3.

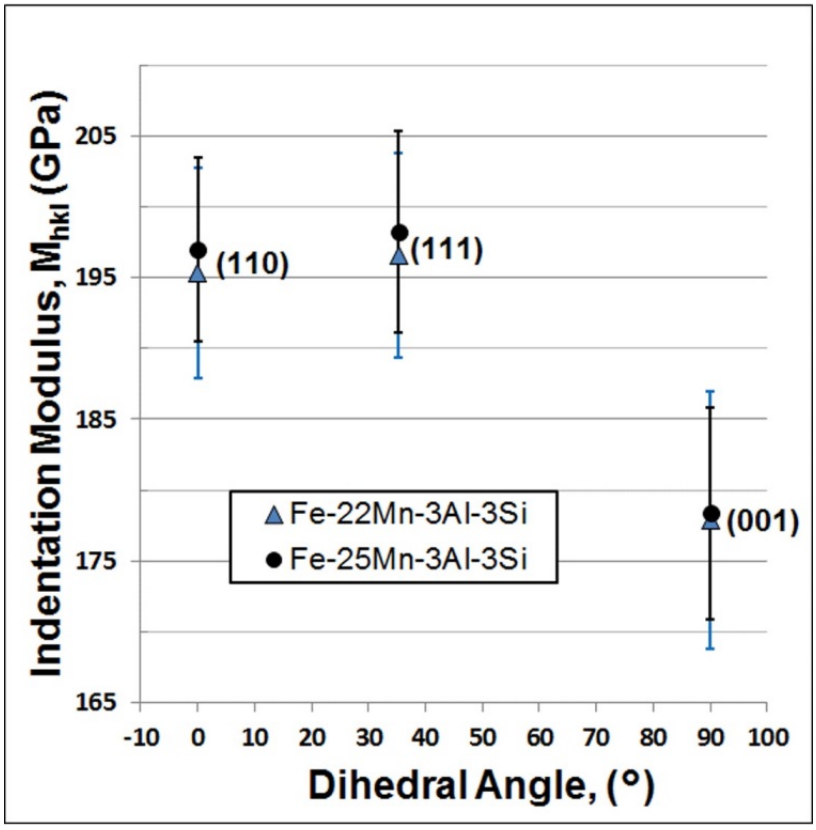

Figure 4-3 - Indentation modulus for grains with crystallographic planes {110}, {111} and {001} parallel to the specimen surface. Error bars represent the standard deviation of measurements. The dihedral angle is the angle between the planes as measured from the {110} plane and rotating about a <−110> axis.

In both alloys, the <111> orientation is slightly more rigid than <110>, while the <100> orientation is ~10% softer. Since the Berkovich indenter is not axisymmetric, the susceptibility of the indentation modulus to in-plane rotation was investigated. In the SEM image of Figure 2-3 an annealing twin boundary (identified by dashed line) is present with habit plane perpendicular to the surface as confirmed by EBSD investigation. The crystal orientation is rotated by ~71° about <101> across the twin boundary. The average indentation modulus, M_{110}, on the left and right side of the twin is 198 and 195 GPa respectively, differing by about 1.5% which is within the uncertainty of the technique. For grains with a three- or four-fold rotation axis perpendicular to the surface, such as {111} and {100} planes, the uncertainty due to in plane rotation is expected to be less [124].

4.3 Calculation of Elastic Constants

The orientation-dependent indentation modulus, M_{hkl}, of an elastically anisotropic material is a complex function of the single-crystal elastic constants of the material, the shape of the indenter and other experimental factors [124] [125]. A model developed by Vlassak and Nix [124] [125] calculates M_{hkl} from single-crystal elastic constants, assuming an axisymmetric indenter. In theory, determining the contact stiffness in three different directions should enable one to calculate the three single-crystal elastic constants. However, as Vlassak and Nix observed [124], poor conditioning of the problem prevents this. In this work, we use a second mathematical model in conjunction with that of Vlassak and Nix. The Hershey-Kroner-Eshelby (HKE) method [103] calculates poly-crystal elastic properties from mono-crystal elastic constants and of numerous similar methods reviewed by Ledbetter, the HKE model was the most accurate when tested on Fe-19Cr-10Ni steel [103] and Cu [126]. By combining these methods and using an

iterative calculation process, the three single-crystal elastic constants are determined from indentation and poly-crystalline elasticity data.

The HKE method [103] calculates the bulk shear modulus by considering an anisotropic non-homogeneity in an isotropic matrix leading to a cubic equation of the form:

$$G^3+\alpha G^2+\beta G+\gamma=0 \tag{4-3}$$

where G is the shear modulus,

$$\alpha=\frac{5C_{11}+4C_{12}}{8}, \tag{4-4}$$

$$\beta=-\frac{C_{44}(7C_{11}-4C_{12})}{8}, \tag{4-5}$$

and

$$\gamma=-\frac{C_{44}(C_{11}-C_{12})(C_{11}+2C_{12})}{8}. \tag{4-6}$$

The Vlassak and Nix model relates M_{hkl} to the polycrystalline indentation modulus, $E/(1-\nu^2)$, by the correction factor $\beta_{(hkl)}$.

$$M_{(hkl)}=\beta_{(hkl)}\left(\frac{E}{1-\nu^2}\right) \tag{4-7}$$

where ν is the polycrystalline Poisson's ratio and

$$\beta_{(hkl)}=a+c(A-A_0)^B \tag{4-8}$$

The value of constants a, c, A_0 and B, tabulated in [125], depend on the grain orientation and the Poisson's ratio in the <100> direction, defined as $\nu_{<100>,}$ and equal to $C_{12}/(C_{11}+C_{12})$. The theoretical model assumes an axisymmetric indenter but multiple studies have shown that it displays excellent agreement with experimental values of M_{hkl} obtained with a Berkovich indenter, for a variety of cubic materials [125] [127]. By assigning a value to $\nu_{<100>, in}$, the constants a, c, A_0 and B of Equation (4-8) are defined from [125] for each crystal orientation.

The anisotropy ratio, A, is solved for in Equation (4-9) [125] with the use of the experimentally determined values M_{111} and M_{100}:

$$\frac{M_{(111)}}{M_{(100)}} = \frac{a_{111}+c_{111}\left(\boldsymbol{A}-A_{0,111}\right)^{B_{111}}}{a_{100}+c_{100}\left(\boldsymbol{A}-A_{0,100}\right)^{B_{100}}} \tag{4-9}$$

The anisotropy ratio is related to the single-crystal elastic constants by Equation (4-10) [128]:

$$A = \frac{2C_{44}}{C_{11}-C_{12}} \tag{4-10}$$

The polycrystalline indentation modulus is calculated from experimentally measured values of M_{111} and M_{100} in (4-11):

$$\left(\frac{M_{(111)}}{\beta_{(111)}} + \frac{M_{(100)}}{\beta_{(100)}}\right)/2 = \left(\frac{E}{1-\nu^2}\right) \tag{4-11}$$

The polycrystalline Poisson's ratio is calculated from the polycrystalline indentation modulus from (4-11) and the values of Young's modulus determined from tensile testing. The bulk modulus, K, and shear modulus G are calculated using the standard elastic moduli relationships. The polycrystalline bulk modulus and single-crystal bulk modulus for cubic materials are assumed to be equal as shown in (4-12) and are typically near 1% of each other for austenitic steels [103].

$$K = \frac{E}{3(1-2\nu)} = \frac{C_{11}+2C_{12}}{3} \tag{4-12}$$

The polycrystalline shear modulus is related to E and ν as shown in Equation (4-13) [128].

$$G = \frac{E}{2(\nu+1)} \tag{4-13}$$

Solving for C_{11}, C_{12} and C_{44} is accomplished with the three independent Equations (4-3), (4-10) and (4-12). Since Equation (4-3) is a trivariate polynomial of the 2nd order (in the current context with G known and C_{11}, C_{12} and C_{44} variables), the system of Equations produces two sets of solutions, one of which can be eliminated as it fails one or more of the mechanical stability requirements for cubic materials ($C_{44}>0$, $C_{11}-C_{12}>0$, $C_{11}>0$ and $C_{11}+C_{12}+2C_{44}>0$) [128]. The term

$v_{<100>, out}$ is calculated from C_{11} and C_{12} of the real solution set. Iterating the process above until $v_{<100>, out} = v_{<100>, in}$, yields the final values of C_{11}, C_{12} and C_{44}, which are listed in Table 4-1, and brings the HKE and Vlassak and Nix methods into agreement. The shear modulus is equal to 72 GPa for both alloys while the bulk modulus is 114 and 115 for the 22 and 25%Mn grades respectively.

Table 4-1 – Indentation moduli (M_{111} and M_{100}), polycrystalline elastic constants (E and ν) and calculated single-crystal elastic constants for three TRIP/TWIP steels, W, Al, Cu, type 316L and β-brass are listed. Established values of single-crystal elastic constants for Fe-Mn binary alloys, W, Al, Cu, steel type 316L and β-brass, from the literature, are provided for comparison.

	Indentation Modulus (GPa)		**Poly Crystalline Modulus**		**Calculated Elastic Constants (GPa)**					**Literature Values of Elastic Constants (GPa)**				
Mat.	**M_{111}**	**M_{100}**	**E (GPa)**	**ν**	**C_{11}**	**C_{12}**	**$(C_{11}-C_{12})/2$**	**C_{44}**	**A**	**C_{11}**	**C_{12}**	**$(C_{11}-C_{12})/2$**	**C_{44}**	**A**
Fe-22Mn-3Al-3Si	196.6[1]	177.9	179±3	0.24±0.01	175 ±7	83±3	46±4	97±4	2.11±0.23					
Fe-25Mn-3Al-3Si	198.2[1]	178.4	179±5	0.24±0.01	174±7	85±3	45±4	99±4	2.22±0.24	Unavailable				
Fe-18Mn-1.5Al-0.6C	200.7[2] [129]	180.8	173.8 [15]	0.24	169±6	82±3	43±4	96±4	2.21±0.24					
Fe-30Mn										200 [104]	127	36.5	130	3.56
Fe-38.5Mn	Unavailable									169.2 [105]	97.7	35.8	140.1	3.92
Fe-40Mn										170 [106]	98	36	141	3.92
W	438[1] [125]	439	409.8 [128]	0.28	524	204	160	160	1.00	522.4 [125]	204.4	159	160.8	1.01
Al	79[1] [125]	77	70.4 [128]	0.35	108	63	22.5	29	1.29	106.8	60.4	23.2	28.3	1.22
Cu	137[1] [125]	124	128.7 [128]	0.35	179	125	27	69	2.60	169.7 [128]	122.6	23.6	74.5	3.16
316L	218[3] [130]	190	193	0.3	208	137	36	118	3.32	196 [130]	129	33.5	116	3.46
β-Brass	130[1] [125]	104	93 [131]	0.36	122	105	8.4	75	8.85	126.5 [125]	107.7	9.4	80.3	8.54

[1]Berkovich indenter
[2]Conical indenter
[3]Vickers indenter

The elastic constants for the 22 and 25%Mn alloys are listed in Table 4-1, along with elastic constants from a third TWIP steel, Fe-18Mn-1.5Al-0.6C, calculated from indentation data in [129] and polycrystalline data in [15]. Elastic constants for binary Fe-30/38.5/40Mn at.% alloys from the literature [104] [105] [106] are displayed for comparison. The tetragonal shear modulus ,$(C_{11}-C_{12})/2$, of the TRIP/TWIP steels ranges between 43-46 GPa compared to 35.8-36.5 GPa for the binary Fe-Mn steels. The large discrepancy can be primarily explained by the difference in magnetic states of the alloys. Experimental evidence by several authors on the influence of Al, Si and C additions on the Néel temperature of Fe-Mn based alloys [48] [132] [133] indicate the three TRIP/TWIP steels are in a magnetically disordered state, whereas the binary Fe-Mn alloys are in the AFM regime at room temperature. In the binary alloys, AFM ordering suppresses $(C_{11}-C_{12})/2$. Cankurtaran et al. [106] quantified the effect by extrapolating $(C_{11}-C_{12})/2$ from data in the PM state to room temperature, predicting the tetragonal shear modulus to be ~43 GPa at room temperature in the absence of AFM ordering, similar to the range of 43-46 GPa for the TRIP/TWIP steels.

The normal shear moduli range from 96-100 GPa for the TRIP/TWIP steels and 130-141 GPa for the binary alloys. In both the TRIP/TWIP and binary Fe-Mn alloys, increasing Mn content resulted in an increase in C_{44}, and the term was not significantly affected by magnetic state. The factors above result in anisotropy ratios ranging from 2.11 to 2.22 in the TRIP/TWIP steels compared to ~3.3-3.9 for binary Fe-Mn alloys [105] [106] and type 316L austenitic stainless steel [103]. In addition, the anisotropy ratios of the three steels are substantially lower than those predicted by ab-initio simulations for Fe-Mn alloys [109] and Fe-Mn-Al/Si alloys [111]. In the latter study, the anisotropy ratio of a Fe-19.6Mn-2Al (at.%) alloy is calculated to be 5.2, strongly

disagreeing with the experimental value obtained for an Fe-18Mn-1.5Al-0.6C alloy in the present work.

4.4 Calculation Validation

The nanoindentation technique is susceptible to experimental factors such as indenter type [125], surface finish, calibration procedures, etc. If two polycrystalline elastic constants are known in the proposed method, the nanoindentation technique is only necessary to calculate the anisotropy ratio from Equation (4-9), which is based on the ratio M_{111}/M_{100}, and less susceptible to the aforementioned uncertainties. If only one polycrystalline elastic constant is known, the second is calculated from the polycrystalline indentation modulus in (4-11), but should be verified for its accuracy with comparable materials. To test the accuracy of this technique, single-crystal elastic constants were calculated from indentation moduli and polycrystalline elastic constants available for W, Al, Cu, 316L steel and β-brass. The resulting values are compared to established values of elastic constants from the literature, in Table 4-1, for the respective materials. The materials present a large range of anisotropy. The calculated elastic constants, C_{11}, C_{12} and C_{44}, display good agreement with the literature values, differing by a standard deviation of ~4%. Even for a highly anisotropic material, such as β-brass, the model suffered no loss in accuracy. The calculated values of the tetragonal shear modulus and anisotropy ratio differ by standard deviations of ~9 and 11% respectively from established literature values.

4.5 Conclusions

The following results and conclusions were drawn from this work:

1. A method to derive single-crystal elastic constants from orientation-specific indentation moduli is proposed for use on polycrystalline cubic materials. The method generates single-crystal elastic constants to within a standard deviation of ~4% of established literature values.
2. The method generates values of C_{11}, C_{12} and C_{44} of 175±7/83±3/97±4 and 174±7/85±3/99±4 GPa for two Fe-(22/25)Mn-3Al-3Si wt.% TRIP/TWIP alloys, respectively. For a Fe-18Mn-1.5Al-0.6C wt.% steel, with indentation data in the literature, the method generates elastic constants of 169±6/82±3/96±4 GPa, showing good agreement with the Fe-Mn-Al-Si steels. These values represent some of the first experimental single-crystal elastic constants for TRIP/TWIP steels and can be utilized to account for anisotropic elasticity, as in [82] [83] [85], to increase the accuracy of SFE measurements.
3. Fe-(22/25)-3Al-3Si and Fe-18Mn-1.5Al-0.6C steels are magnetically disordered at room temperature and do not experience significant suppression of the shear term $(C_{11}-C_{12})/2$ caused by antiferromagnetic ordering. As a result, the anisotropy ratios of the TRIP/TWIP steels, 2.11-2.22, are significantly lower than those of ~3.5-3.9 for binary Fe-30-40Mn at.% alloys with similar composition but in the antiferromagnetic state. For TWIP steels in the antiferromagnetic regime at room temperature, such as the Fe-22Mn-0.6C grade, the elastic anisotropy is expected to be higher.

CHAPTER 5

THE INFLUENCE OF MANGANESE CONTENT ON THE STACKING-FAULT AND AUSTENITE/ε-MARTENSITE INTERFACIAL ENERGIES

This chapter is heavily based on accepted and published papers [115] [116] [117] [134] although the relevant introductory material and experimental procedures are covered in chapters 1 and 2.

5.1 Stacking-Fault Energy Measurements

Additions of Mn from 22 to 28 wt.% increase the SFE and reduce the partial-dislocation separations. Partial-dislocation core separations in the 22%Mn alloy ranged from 6 to 13 nm depending on character angle. Figure 5-1a displays a WBDF image of a partial-dislocation pair with a character angle of 39° in a specimen deformed to the YP. The average actual partial-dislocation core separation is 9.3 ±1.1 nm, in which the uncertainty is one standard deviation of all measurements along the length of the dislocation (note: measurements were taken every 5-10 nm along the length of dislocations but most are removed from the figures for clarity). The BF image in Figure 5-1b of the same dislocation illustrates the increased resolution of the WBDF technique. In Figure 5-1c, a dislocation pair in a 22%Mn specimen deformed to the YP with a smaller character angle of 26° exhibits an average core separation of 6.6 ±0.5 nm. Due to a low SFE, partial-dislocation separations in the 22%Mn alloy displayed greater variations and susceptibility to image forces, as evidenced by partial dislocations in specimens deformed to the YP in Figure 5-2. The width of the partials in Figure 5-2a fluctuates dramatically at the foil

surfaces, where the partials are constricted at one intersection while showing a large separation distance at the other. In Figure 5-2b, a partial-dislocation pair in the (111) habit plane normal to the [111] beam, imaged with a -220 g-vector, is interacting with a stacking fault on (-111). The partial dislocations in (111) experience a contraction in their separation at the intersection with the partial dislocation on the inclined plane. In an image of the same defects with a 02-2 g-vector (Figure 5-2c), one of the partials on (111) and SF on (-111) become invisible ($|g \cdot b_p| = 0$). This study avoided partial dislocations such as those in Figure 5-2 for quantitative measurements.

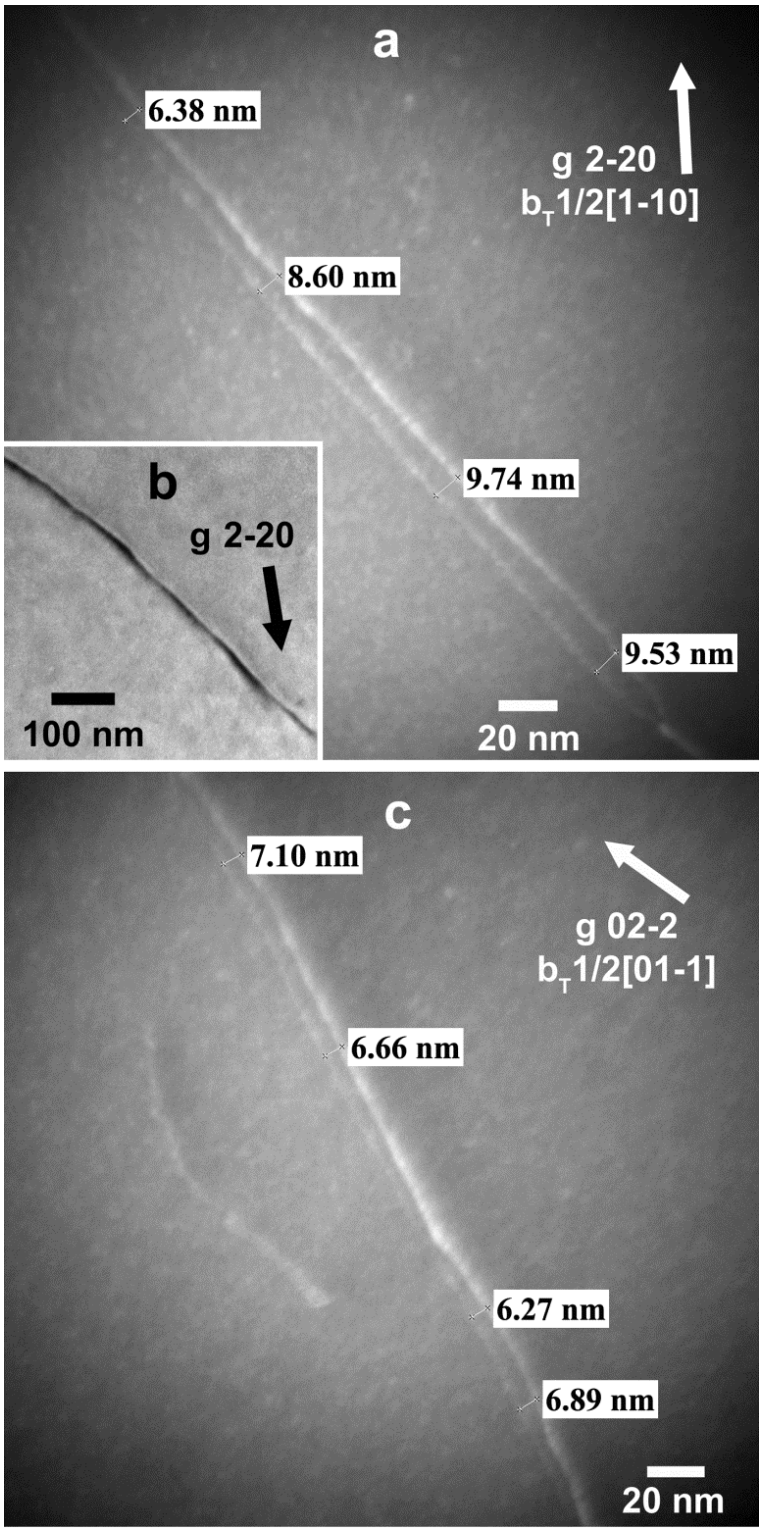

Figure 5-1 – Images of dislocations in 22%Mn specimens deformed to the YP. (a) WBDF and (b) corresponding BF image of a partial-dislocation pair. (c) WBDF image of a second partial dislocation pair closer to screw character and displaying reduced separation. Only a few representative separation measurements are shown.

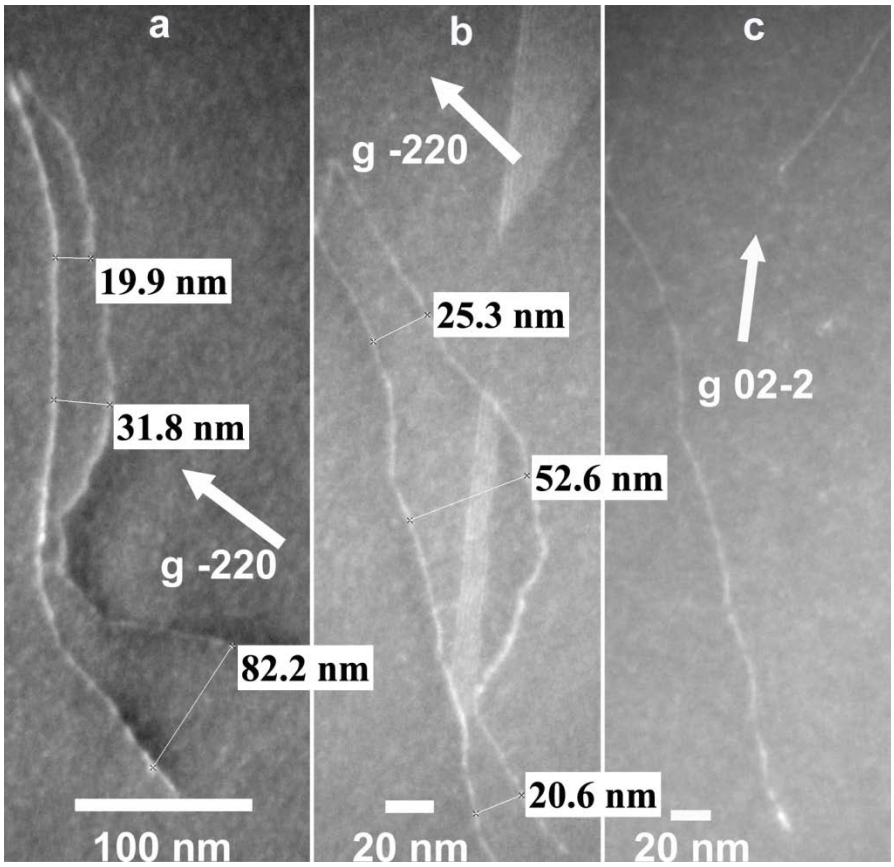

Figure 5-2 – WBDF images of partial-dislocation pairs in a 22%Mn alloy deformed to the YP. In (a) the partials display non-uniform separation, most dramatically at the intersections with the foil surfaces. In (b) a partial-dislocation pair residing in (111) normal to the [111] beam direction is interacting with a stacking fault on (-111). In (c), the defects in (b) are imaged with a 02-2 diffracting vector leading to invisibility of one of the partials in (111) and the SF on (-111).

The separation of partials in the 25%Mn alloy ranges from 4 to 7 nm, with Figure 5-3 showing a partial-dislocation pair with average actual spacing of 4.9 ±0.5 nm and a total character angle of 22°. Additional measurements of partial-dislocation separations in this alloy were reported in preliminary publication [115].

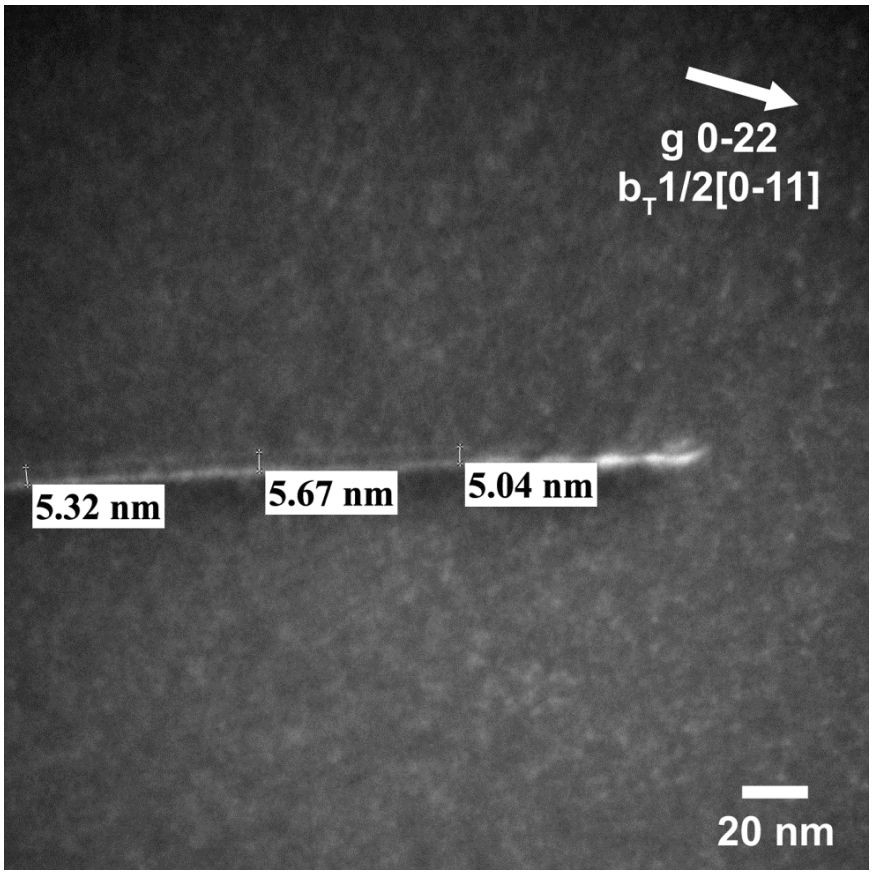

Figure 5-3 – A WBDF image of a partial-dislocation pair in an Fe-25Mn-3Al-3Si alloy deformed to the YP.

Partial-dislocation separations in the 28%Mn alloy ranged from 2.6 to 4.3 nm. Imaging with g(4g) diffracting conditions decreased image-widths and reduced the discrepancy between observed and actual partial-dislocation separations. In figure 5-4a, a partial-dislocation pair with kinks or jogs along its length and a character angle of 40° exhibits an average actual spacing of 3.3 nm on uniform sections. In Figure 5-4b a partial-dislocation pair with a character angle of 15° displays an average actual spacing of 2.5 nm. At small spacing the intensity of the partial-dislocation image located between the partial-dislocation cores becomes significantly weaker due to fewer atomic planes oriented for scattering, as clearly shown in Figure 5-4b.

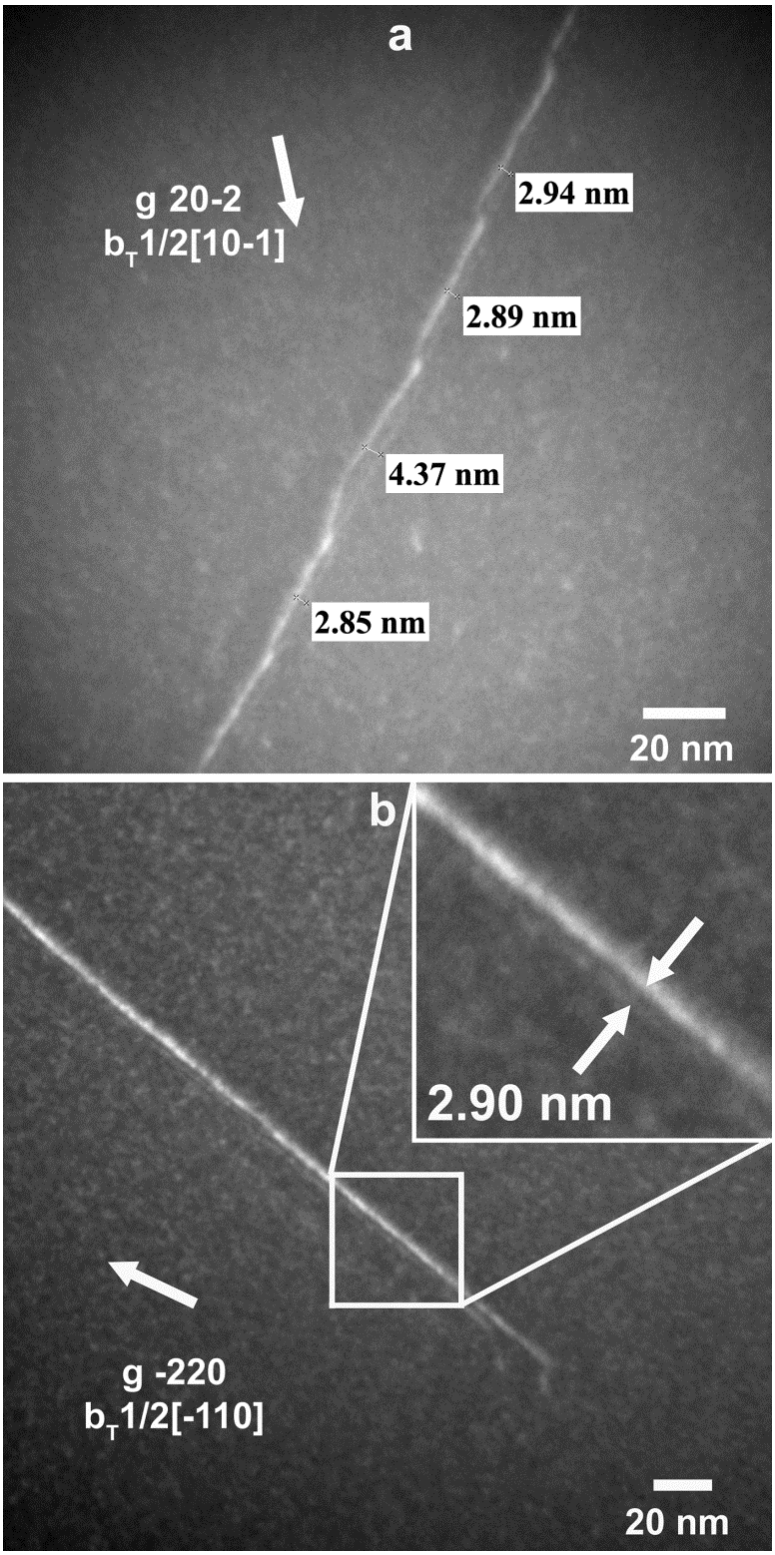

Figure 5-4 – WBDF images of partial-dislocation pairs in specimens of the 28%Mn alloy deformed to (a) the YP and (b) 1.5% with heat treatment of 650°C for 48 h.

The character of stacking faults (intrinsic vs. extrinsic) in the present alloys, as determined by typical diffraction contrast methods (e.g., Williams and Carter [88] and Edington [89]), is intrinsic. Figures 5-5a, b and c display three dark-field TEM micrographs of stacking faults corresponding to the 22, 25 and 28%Mn alloys respectively. In Figure 5-5a and c the 111 g-vector is pointing away from the bright fringe while in 5-5b the 002 g-vector is pointing towards the bright fringe indicating they are all intrinsic in nature. Of ~10 faults investigated for each alloy, all were intrinsic.

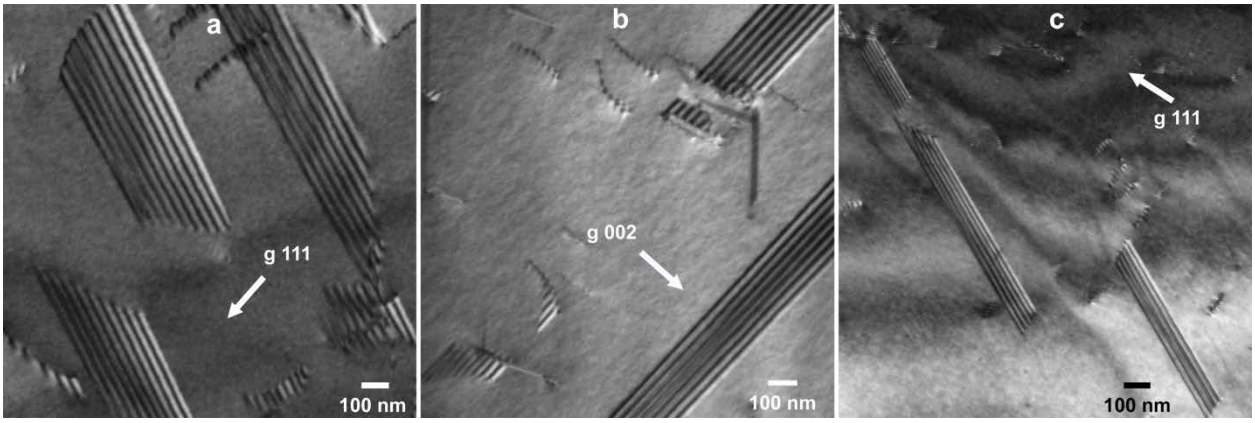

Figure 5-5 – Dark-field images of intrinsic SFs in (a) the 22%Mn, (b) the 25%Mn and (c) the 28%Mn alloys as identified by the procedure in [89] [88].

Figure 5-6 displays the average spacing of partial-dislocation pairs in the three alloys. Theoretical partial-dislocation spacing curves based on Equation (1-4) with the modification that effective values of the shear modulus and Poisson's ratio are utilized in lieu of polycrystalline values. The relationship for the effective shear modulus and Poisson's ratio are given in Equations (1-5) through (1-7), and account for elastic anisotropy in (111). The term b_p from Equation (1-4) is the $a_o/6<112>$ partial-dislocation Burgers vector, determined by XRD of recrystallized Fe-22/25/28Mn-3Al-3Si specimens to be 0.1476, 0.1477 and 0.1479 nm, respectively and the total dislocation character angle is β. The effective shear modulus, μ_{eff}, for

dislocations in {111} is a function of the single-crystal elastic stiffness constants C_{11}, C_{12} and C_{44}, and defined by Equation (1-5). Equations (1-6) and (1-7) denote the relationship between the effective Poisson's ratio, ν_{eff}, and the single-crystal elastic constants. For the 22, 25 and 28%Mn alloys, respectively, μ_{eff}=67±4, 66±4, 66±4 GPa and ν_{eff}=0.30, 0.31 and 0.31. The terms μ_{eff} and ν_{eff} account for anisotropic elasticity in {111} and are calculated from equations using single-crystal elastic constants determined in Chapter 4 ([119]). The experimental SFEs for the 22, 25 and 28%Mn alloys are 15±3, 21±3 and 40±5 mJ m^{-2}, respectively. The large increase in SFE energy above 25 wt.% Mn is consistent with experimental observations that show a sharp reduction in the ε-martensite start temperature for additions of Mn above 25 wt.% in binary Fe-Mn alloys [98] [135]. The uncertainty of the SFE is primarily due to the scatter of average d_{actual} values between different dislocations (data points in Figure 5-6) and uncertainties of ν_{eff} and μ_{eff}. The first two sources of uncertainty are accounted for by fitting upper and lower bounds (SFE curves) that encompass the majority of the data points for a given composition as shown in Figure 5-6. The uncertainty from these two sources was determined to be ±20.0, ±14.3 and ±12.5% of the SFE for the 22, 25 and 28%Mn alloys, respectively. The uncertainty of μ_{eff} is ±6.0%. The final uncertainty of the SFE for the 22, 25 and 28%Mn alloys was obtained from the root sum square of the two calculated values and is ±20.9 (e.g., $(20.0^2 + 6.0^2)^{\frac{1}{2}}$), ±15.5 and ±13.9% or ±3, ±3 and ±5 mJ m^{-2} (rounded to one significant figure). Volosevich et al. [79] reported SFE values of ~15 and 27.5 mJ m^{-2} for Fe-22/25Mn wt.% alloys, respectively, by TEM observation of extended nodes. These values likely overestimate the SFE, since the combined effect of adding 3 wt.% Al and Si would raise the SFE, yet the SFE values of the Fe-22/25Mn-3Al-3Si steels are equal or less. If isotropic elasticity is applied to the measurements on the 22%Mn alloy (i.e., using Equation (1-4) with polycrystalline shear modulus and Poisson's ratio

of 72 GPa and 0.24 [119], respectively) the SFE is 16 ±4 mJ m^{-2} (dashed lines in Figure 5-6). The SFE determined with isotropic elastic constants overestimates the anisotropic value by ~7% and results in a poorer data fit, producing a larger uncertainty of ±4 mJ m^{-2}. The overestimation of the SFE results from the use of the larger isotropic shear modulus and the poorer data fit stem from the large difference between the isotropic and effective values of the Poisson's ratio. The elastic anisotropy ratio ($2C_{44}/(C_{11}-C_{12})$) of the present materials is ~2.2 (See Chapter 4). For FCC materials, μ_{eff} and ν_{eff} will become increasingly smaller and larger, respectively, relative to the polycrystalline values, as the elastic anisotropy ratio increases [84].

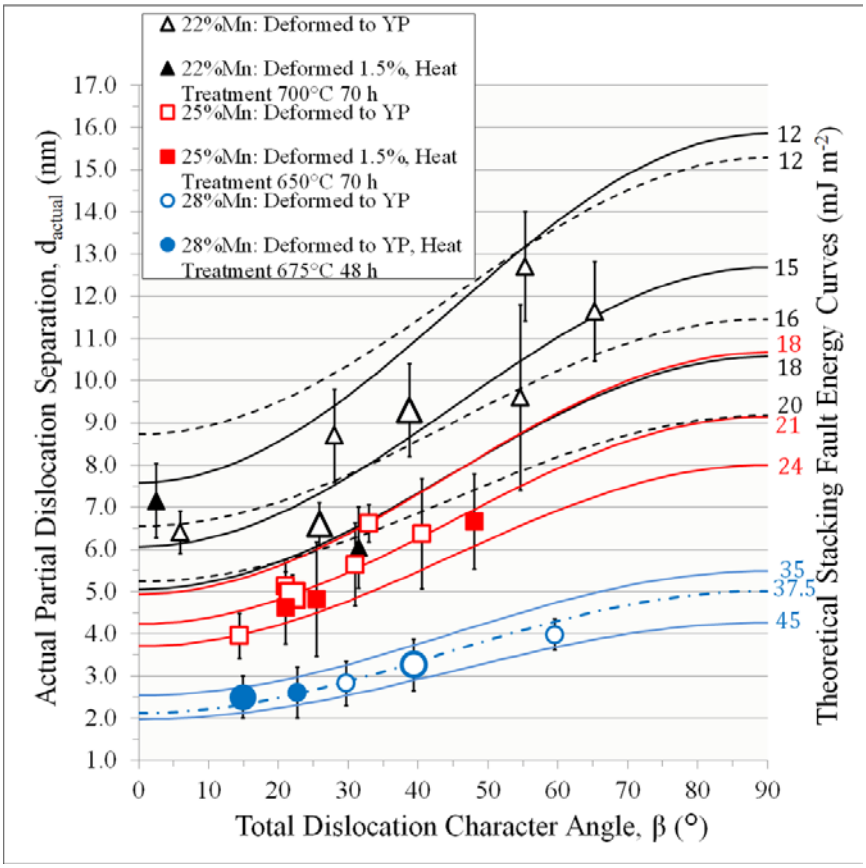

Figure 5-6 – Average actual partial-dislocation separations for the 22, 25 and 28%Mn alloys for specimens deformed to the YP and 1.5% with heat treatments. The error bars represent the standard deviation of the measurements on individual pairs. The dashed and solid curves represent theoretical partial-dislocation spacings based on isotropic and anisotropic elasticity, respectively. The dash dot line for the 28%Mn alloy assumes a Peierls core model. The larger symbols correspond to the partial dislocations from Figures 5-1, 5-3 and 5-4.

In the above analysis, the partial dislocation cores are treated as purely elastic defects, i.e. as singular Volterra type dislocations with a core width of zero. However, the core width of dislocations may not be zero and, at small partial-dislocation separations, such as those observed in the 28%Mn alloy, core effects can influence SFE measurements as shown by Cockayne and Vitek [86]. The dislocation core thickness can influence the force acting between two partial dislocations and thus, their separation. The partial-dislocation separation obtained from a Peierls-type core model, $d_{Peierls}$, which accounts for core width, is related to the partial-dislocation separation of Equation (1-4), d_{actual}, by Equation (1-8) [86]. In this model, as core width increases, the repulsive force acting between the two partial dislocations decreases. Since the core width, ζ, is unknown, a reasonable approximation is twice the lattice parameter (0.724 nm), as employed by Cockayne and Vitek [86]. Applying this model to the partial-dislocation separation measurements of the 28%Mn alloy yields a SFE of 37.5 mJ m^{-2} as depicted in Figure 5-6 (dash-dot line), which is slightly smaller than 40 mJ m^{-2} obtained assuming singular cores. The fit of Equation (1-8) to the partial-dislocation separation measurements of the 28%Mn alloy becomes increasingly worse as the core thickness is increased above 0.724 nm. Therefore, the true value of the partial-dislocation core width for the 28%Mn alloy is likely between 0 and 0.724 nm. As such, the SFE of the 28%Mn alloy is taken as the average of the two SFE values, 38.8 ±5 mJ m^{-2}. Since the partial-dislocation separations of the 22 and 25%Mn alloys are substantially larger, assuming a core width of 0.724 nm in these alloys produced no significant change in the SFE. Cockayne and Vitek [86] also suggested that partial-dislocation core widths greater than twice the lattice constant may lead to a less well defined image peak and an additional narrow image peak under certain circumstances [86]. No such features observed in the

WBDF images for each alloy could be attributed to these effects giving further confidence that the partial dislocation core thickness is below 0.724 nm.

5.2 Coherency Strain Energy Contribution

The FCC matrix and ε_{hcp}-martensite have the $(111)_\gamma||(0001)_\varepsilon/[1\text{-}10]_\gamma||[1\text{-}210]_\varepsilon$ orientation relationship. However, the ε_{hcp}-martensite phase displays a slightly smaller molar volume than the austenite phase. Brooks et al. [53] showed the local close packed plane (CPP) spacing of single stacking faults contracts ~2% relative to the CPP spacing of the austenitic matrix in Fe–Cr–Ni steels, and thus that stacking faults are ε_{hcp}-martensite embryos or nuclei. Marinelli et al. [55] [56] observed decreases in the molar volume of the ε_{hcp}-martensite structure of ~2% relative to austenite in binary Fe-Mn alloys. The propensity to contract is resisted by the matrix (i.e., austenite phase), which results in the deformation of both austenite matrix and the martensite phase. This *coherency* strain increases the energy of the stacking fault complex. It is desirable to remove the coherency strain-induced energy contribution from the SFE of experimental measurements so that comparison to theoretical SFE values is applicable. Two procedures for calculating the coherency strain energy were discussed in Section 1.3.2 [51] [57]. The Müllner and Ferreira [57] model assumes that the coherency strain is volume preserving (i.e., VS=0), which contrasts with our experimental measurements. Therefore, the method of Olson and Cohen [51] has been used to estimate the coherency strain energy in this study.

The orientation of the principal strain axes ε_{11}, ε_{22} and ε_{33} are assumed to remain unchanged by the transformation resulting in values of 0 for shear strains ε_{12}, ε_{23} and ε_{13} in Equation (1-22). The accommodation factor (η) is the ratio between the total energy per unit inclusion (i.e., martensite

phase) volume embedded in the austenite phase to the energy per unit inclusion volume embedded in a hypothetical rigid matrix [51] [102]. For pure dilatation η is constant regardless of particle shape and is built in to Equation (1-21). For shear strain, η may vary from 0 to 1 depending on particle shape and the strain state [102]. Following [51] [135], η for a spherical inclusion, which is independent of strain state, is employed:

$$\eta = \frac{7-5\nu}{15(1-\nu)} \tag{5-1}$$

Table 5-1 provides the lattice parameters of the FCC and ε_{hcp}-martensite phases obtained from the Rietveld refinement of XRD patterns from recrystallized specimens (for FCC) and those displayed in Figure 5-7 from specimens deformed to failure (for HCP), with uncertainty representing equipment error. The XRD patterns in Figures 5-7a, 5-7b and 5-7c are from the 22, 25 and 28%Mn samples after deformation to failure at RT, -25°C and -100°C, respectively. The presence of strain-induced ε-martensite is confirmed for each condition, while the formation of strain-induced α-martensite is noted in the 22 and 25%Mn alloys.

Table 5-1 – Lattice constants determined by XRD.

	FCC (Å)		ε_{hcp}-martensite (Å)	
Alloy	a_{fcc}	c_{fcc} ($2a_{FCC}/\sqrt{3}$)	a_{hcp}	c_{hcp}
22%Mn	3.615±0.001	4.175±0.002	2.548±0.003	4.153±0.005
25%Mn	3.617±0.001	4.177±0.002	2.547±0.003	4.151±0.005
28%Mn	3.620±0.001	4.180±0.002	2.545±0.003	4.152±0.005

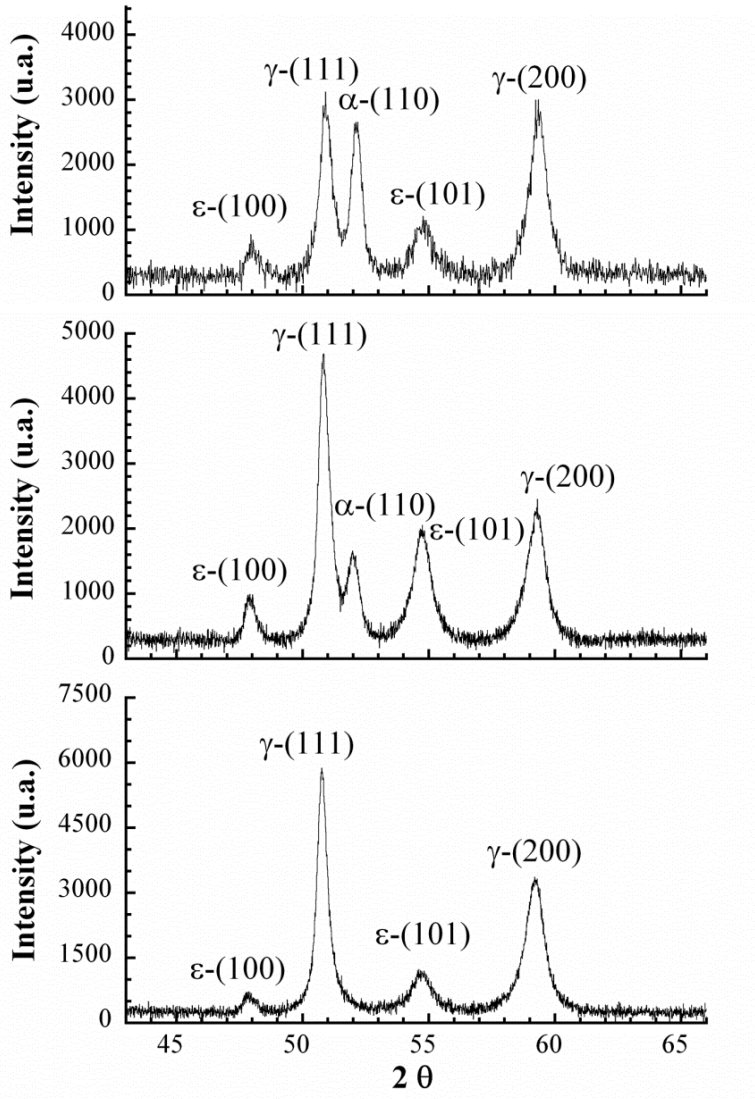

Figure 5-7 – XRD patterns for (top) an Fe-22Mn-3Al-3Si alloy deformed at room temperature, (middle) an Fe-25Mn-3Al-3Si alloy deformed at -25°C and (bottom) an Fe-28Mn-3Al-3Si alloy deformed at -100°C. All samples deformed to maximum uniform elongation. The peaks are labeled according to phase and reflection in miller indices.

A slight increase in the lattice parameters of the FCC phase with Mn content is observed while no trend in the HCP lattice parameters can be deduced over the current range of Mn. Utilizing the lattice parameters from Table 5-1 in conjunction with the method reported by Olson and Cohen [51] yields ε_{11}, ε_{22}, ε_{33}, VS, E_{dil}, E_{sh} and $2\rho E_{str}$ as shown in Table 5-2. The uncertainties,

calculated using a root sum square approach, are ~25% for ε_{11}, ε_{22} and ε_{33} and ~43% for *VS*. The uncertainties are ~62 and 79% for E_{dil} and E_{sh}. The value of E_{sh} is small compared to E_{dil} for the Fe-22/25/28Mn-3Al-3Si alloys and consequently, the uncertainty of $2\rho E_{str}$ is also ~62%. The values of VS ranged from -0.011 to -0.018 (-1.1 to -1.8%). Notwithstanding a substantial uncertainty in the calculation of the strain components, the experimental data suggest that contraction increases with Mn content. This is in line with the previous studies conducted on binary Fe-Mn steels [55] [56]. The value of $(E_{sh} + E_{dia})$ calculated by Olson and Cohen [51] is 41.9 mJ mol^{-1} for an Fe-Cr-Ni steel and similar to the values calculated here (see Table 5-2). In addition, Müllner and Ferreira [57] calculated a value of 4.3 mJ m^{-2} for $2\rho E_{str}$ for a type 316 austenitic steel which is similar to the values calculated in the present work of 1.4 ±0.87, 2.3±1.4 and 3.6 ±2.2 mJ m^{-2} for the Fe-22/25/28Mn-3Al-3Si alloys, respectively.

Table 5-2 – Parameters used in the calculation of E_{str} and $\sigma^{\gamma/\varepsilon}$ for Fe-Mn based alloys

Parameter	Fe-22Mn-3Al-3Si	Fe-25Mn-3Al-3Si	Fe-28Mn-3Al-3Si	Fe-16Mn	Fe-18Mn	Fe-20Mn	Fe-22Mn	Fe-25Mn	Fe-17.7Mn-0.62C	Fe-17.7Mn-0.59C-1.59Si	Fe-17.5Mn-0.58C-1.54Al	Fe-18Mn-0.6C	Fe-18Mn-0.6C-1.5Al	Fe-18Mn-0.6C-2.5Al
γ_{exp}(mJ m^{-2})[1]	15 ±3	21±3	38.8±5	26±3.1	22±2.6	18±2.2	15±1.8	27.5±3.3	19.3±2.5	13.8±2.5	29.1	13±3	30±10	40.4
μ (GPa)[2]	72	72	72	69	69	69	69	69	71	72.5	70.1	71	70.1	70.1
ν[2]	0.24	0.24	0.24	0.23	0.23	0.23	0.23	0.23	0.23	0.24	0.24	0.23	0.24	0.24
e_{11}[3]	-0.0032	-0.0041	-0.0058	-0.0029	-0.0029	-0.0025	-0.0033	-0.0033						
e_{22}[3]	-0.0032	-0.0041	-0.0058	-0.0029	-0.0029	-0.0025	-0.0033	-0.0033						
e_{33}[3]	-0.0051	-0.0061	-0.0067	-0.0145	-0.0144	-0.0146	-0.0153	-0.0154						
VS[3]	-0.011	-0.014	-0.018	-0.020	-0.020	-0.019	-0.022	-0.022						
E_{dil} (J mol^{-1})[4]	24.1	38.3	61.1	69.2	69.4	65.1	81.7	83.4	71.4	74.4	72.0	71.4	72.0	72.0
E_{sh} (J mol^{-1})[4]	0.6	0.7	0.2	21.8	21.4	24.0	23.3	24.0	22.0	22.6	21.8	22.0	21.8	21.8
$2\rho E_{str}$ (mJ m^{-2})[4]	1.4±0.9	2.3±1.4	3.6±2.2	5.4±0.5	5.4±0.5	5.3±0.5	6.2±0.5	6.4±0.5	5.5±0.5	5.8±0.5	5.6±0.5	5.5±0.5	5.6±0.5	5.6
T_{Neel}^{FCC}[5] (K)	267	282	298	310	332	352	370	395	289	237	268	289	268	261
T_{Neel}^{HCP}[5] (K)	123	137	153	94	106	118	129	147	101	100	99	104	102	101
$2\rho\Delta G_{chem}^{fcc\rightarrow hcp}$ (mJ m^{-2})[6]	-6.7	-0.2	9.1	-48.4	-43.9	-38.8	-33.3	-24.2	-11.4	-13.2	1.0	-11.9	2.6	11.4
$2\rho\Delta G_{Mag}^{fcc\rightarrow hcp}$ (mJ m^{-2})[6]	1.5	2.0	2.6	3.9	6.0	8.3	10.7	14.0	2.1	0.8	1.4	2.1	1.4	1.2
$\sigma^{\gamma/\varepsilon}$ (mJ m^{-2})[7]	9.3±1.6	8.6±1.7	11.8±2.7	32.5±1.6	27.3±1.3	21.6±1.1	15.7±0.9	15.7±1.7	11.5±1.3	10.3±1.3	10.6±1.3	8.6±1.5	10.2±5	11.1

[1]Experimental SFEs taken from present work and [15] [16] [79]. The term γ_{exp} for the Fe-18Mn-0.6C-2.5Al alloy is calculated.
[2]Shear modulus and Poisson ratio taken from [15] [16] [79] [119]. Assumed to be the same for Fe-18Mn-0.6C-1.5/2.5Al alloys.
[3]Strain values obtained from lattice parameters determined in the present work and [55] [56].
[4]Strain energy terms are calculated using the strain values in accordance with the methodology discussed in Chapters 1 and 5 (strain values for Fe-18Mn grade used for Fe-18Mn-0.6C-0/1.5/2.5(Al/Si) alloys). Uncertainties for the Fe-22/25/28Mn-3Al-3Si and binary Fe-Mn alloys are based on the uncertainty of the lattice parameters and the standard deviation of $2\rho E_{str}$ (for Fe-16/18/20/22/25Mn alloys), respectively.
[5]T_{Neel}^{FCC} is obtained from [48] [98] [132] [136]. T_{Neel}^{HCP} is obtained from Equation (5-12) [137].
[6]Terms $2\rho\Delta G_{chem}^{fcc\rightarrow hcp}$ and $2\rho\Delta G_{Mag}^{fcc\rightarrow hcp}$ were determined with the model developed in the present work.
[7]Calculated interfacial energy in accordance with Equation (1-15). Interfacial energy for Fe-18Mn-0.6C-2.5Al steel is calculated using Equation (5-13).

Figure 5-8 shows the experimental (γ_{exp}) and ideal (γ_{∞}) SFE values. The dependence of γ_{exp} and γ_{∞} on Mn content above 24.7 wt.% is approximated as linear functions displayed in Figure 5-8. The use of linear functions (rather than higher order polynomials) to describe the increase in SFE for Mn contents greater than 24.7 wt.% is consistent with other experimental SFE measurements which exhibit quasi-linear behavior from 25 to 35 wt.% Mn [79] [138]. Quadratic polynomial functions of γ_{exp} and γ_{∞} as a function of Mn content (displayed in Figure 5-8) were employed to approximate the SFE in the range of 22.2 to 24.7 wt.%Mn. The data indicate that a plateau of γ_{exp} and γ_{∞} occurs near 22wt.% Mn which is in good agreement with the experimentally observed minimums of 22 wt.%Mn by Volosevich et al. [79] and between 20 and 25 wt.% (depending on purity of the Fe-Mn alloys) by Petrov et al. [138].

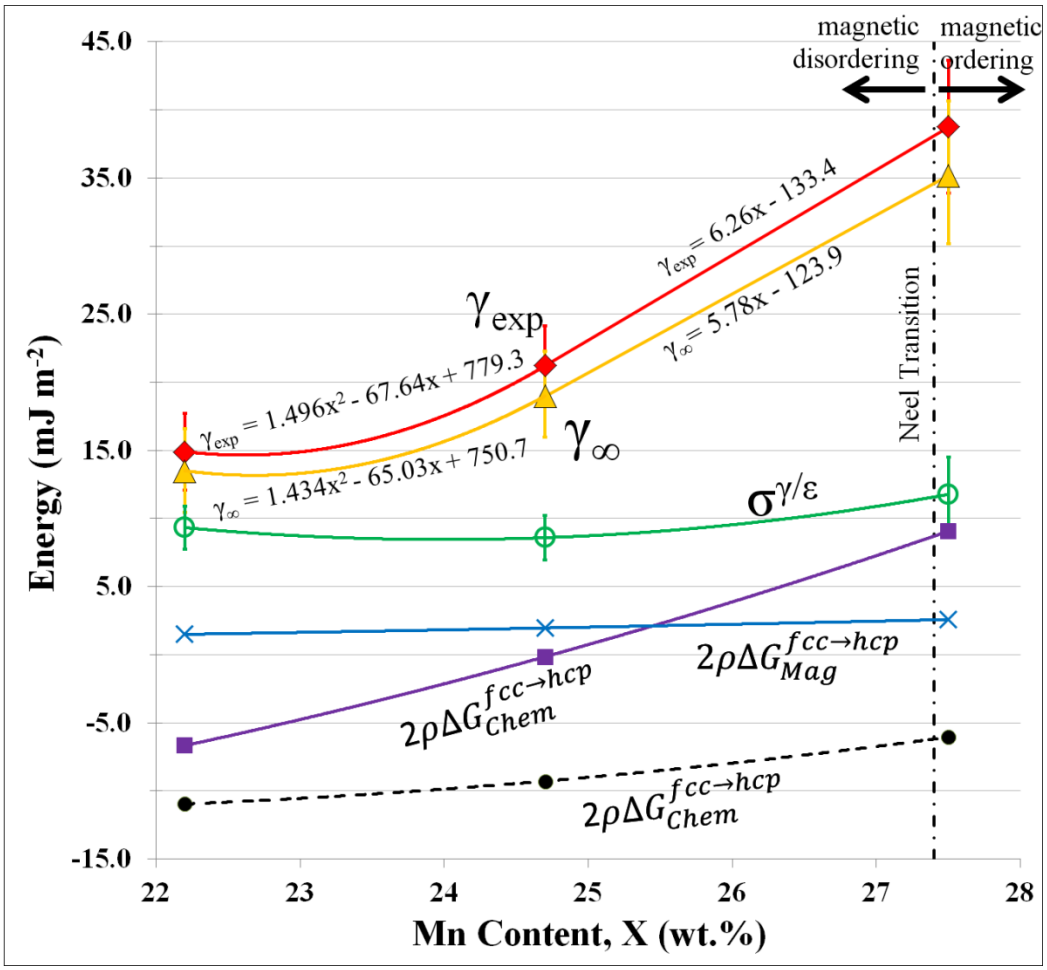

Figure 5-8 – Experimental effective SFE (γ_{exp}) and ideal SFE (γ_{∞}) values with error bars representing the standard deviation of the measurements. Chemical ($n\rho\Delta G_{Chem}^{fcc\rightarrow hcp}$) and magnetic ($n\rho\Delta G_{Mag}^{fcc\rightarrow hcp}$) contributions to the difference in Gibbs free energy from the FCC to HCP phase transformation determined by thermodynamic model (note: the values of $n\rho\Delta G_{Chem}^{fcc\rightarrow hcp}$ denoted by the dashed line were calculated using $L_{Fe,Mn:Va}^{HCP}$ proposed by Djurovic et al. [139]). Interfacial parameters $\sigma^{\gamma/\varepsilon}$ calculated from the experimental and theoretical data. All values are plotted as a function of Mn content. The dash-dot line indicates Mn content at which the Néel transition occurs at 298K for an Fe-XMn-2.7Al-2.9Si wt.% steel [132].

5.3 Thermodynamic Modeling

To determine the interfacial energy from Equation 1-15, a new thermodynamic model was developed to calculate $\Delta G_{Chem}^{fcc\rightarrow hcp}$ and $\Delta G_{Mag}^{fcc\rightarrow hcp}$ for the present Fe-Mn-Al-Si-C system.

Existing thermodynamic models [3] [17] [35] [96] [98] for Fe-Mn based steels were evaluated and deemed unsuitable for the present study for several reasons. The models of Saeed-Akbari et al. [35], Mosecker and Saeed-Akbari [17] and Nakano and Jacques [98] address the Fe-Mn-Al-C, Fe-Cr-Mn-N and Fe-Mn-C systems, respectively, but do not attempt to specifically address the influence of Si. Experimental studies on Fe-18Mn-0.6C-0/1.5Si [16] wt.% and Fe-31Mn-xSi-0.77C at.% [140] alloys report decreases in the SFE with additions of Si. However, the model of Dumay et al. [96] shows that additions of Si up to ~4 wt.% increase the SFE of an Fe-22Mn-0.6C steel, disagreeing with the experimental results. The model of Curtze et al. [3] utilizes the same thermodynamic parameters as used by Dumay et al. [96] for both pure Si and its interaction with Fe. A thermodynamic model by Tian and Zhang [141] also predicts an increase in SFE for Fe-31Mn-xSi-0.77C (x=at.%) alloys for Si additions up to 10.2 at%. The more recent thermodynamic models of Nakano and Jacques [98] and Mosecker and Saeed-Akbari [17] show that the treatment of interstitial elements like C is enhanced by the use of a sub-lattice type thermodynamic model. Finally, improved thermodynamic parameters for the Mn-C and Fe-Mn-C systems have recently been published by Djurovic et al. [139] [142]. For the new model, the FCC and HCP phases were treated as randomly mixed substitutional solutions with two sublattices: substitutional and interstitial [17] [98]:

$$(Fe, Mn, Al, Si)_1(C, Va)_\lambda \tag{5-2}$$

with λ equal to 1 for FCC and 0.5 for HCP, assuming that interstitial elements do not occupy neighboring octahedral sites in the HCP structure [98] [143]. The term “Va” stands for vacancy. The terms G_m^{hcp} and G_m^{fcc} are the molar Gibbs free energy of the individual phases, Φ (FCC or HCP) [17] [98]:

$$G_m^\phi = y_{Fe}^\phi y_C^\phi \, {}^0G_{Fe:C}^\phi + y_{Fe}^\phi y_{Va}^\phi \, {}^0G_{Fe:Va}^\phi + y_{Mn}^\phi y_C^\phi \, {}^0G_{Mn:C}^\phi + y_{Mn}^\phi y_{Va}^\phi \, {}^0G_{Mn:Va}^\phi +$$

$$y_{Al}^{\phi}\left(\frac{y_{Va}^{FCC}+y_{Va}^{HCP}}{2}\right)\,{}^{0}G_{Al:Va}^{\phi}+y_{Si}^{\phi}\left(\frac{y_{Va}^{FCC}+y_{Va}^{HCP}}{2}\right)\,{}^{0}G_{Si:Va}^{\phi}+RT\begin{pmatrix}y_{Fe}^{\phi}lny_{Fe}^{\phi}+y_{Mn}^{\phi}lny_{Mn}^{\phi}+\lambda y_{C}^{\phi}lny_{C}^{\phi}+\\ \lambda y_{Va}^{\phi}lny_{Va}^{\phi}+y_{Al}^{\phi}lny_{Al}^{\phi}+y_{Si}^{\phi}lny_{Si}^{\phi}\end{pmatrix}+$$

$${}^{ex}G_{m}^{\phi} \tag{5-3}$$

In Equation (5-3), R is the gas constant and T is the temperature in K. The site fractions of the individual elements, y_i, in the substitutional lattice are calculated as:

$$y_i = \frac{x_i}{(1-x_C)} \tag{5-4}$$

and for C in the interstitial lattice as:

$$y_C = \frac{x_C}{\lambda(1-x_C)} \tag{5-5}$$

where *x* is the mole fraction of each element. Equation (5-6) defines the correlation between the individual site fractions:

$$y_{Fe}+y_{Mn}+y_{Al}+y_{Si} = y_C+y_{Va} = 1 \tag{5-6}$$

The thermodynamic parameters $G_{i:Va}^{\phi}$ and $G_{i:C}^{\phi}$ in Equation (5-3) are listed in Table 5-3. They represent the Gibbs energy of substitutional element *i* in phase *Φ* when all available interstitial sites are vacant (Va) or occupied by C, respectively. The terms ${}^{0}G_{Al:C}^{\phi}$ and ${}^{0}G_{Si:C}^{\phi}$ were not included in Equation (5-3) due to a lack of data for the HCP phase. In addition, average vacancy site fractions, $\left(\frac{y_{Va}^{HCP}+y_{Va}^{FCC}}{2}\right)$, were used for Si and Al and resulted in significantly better agreement with experimental results for steels with Si and C. The combined term $\Delta\,{}^{0}G_{Si:Va}^{HCP\rightarrow FCC}$ replaces ${}^{0}G_{Si:Va}^{HCP}$, ${}^{0}G_{Si:Va}^{FCC}$ and $RTy_{Si}^{\phi}lny_{Si}^{\phi}$ in the calculation of $\Delta G_{Chem}^{fcc\rightarrow hcp}$. The excess free energy is described as [98]:

$$^{ex}G_m^{\phi} = y_{Fe}^{\phi} y_{Mn}^{\phi} y_C^{\phi} L_{Fe,Mn:C}^{\phi} + y_{Fe}^{\phi} y_{Mn}^{\phi} y_{Va}^{\phi} L_{Fe,Mn:Va}^{\phi} + y_{Fe}^{\phi} y_C^{\phi} y_{Va}^{\phi} L_{Fe:C,Va}^{\phi} + y_{Mn}^{\phi} y_C^{\phi} y_{Va}^{\phi} L_{Mn:C,Va}^{\phi} +$$

$$y_{Fe}^{\phi} y_{Al}^{\phi} (\frac{y_{Va}^{FCC} + y_{Va}^{HCP}}{2}) L_{Fe,Al:Va}^{\phi} + y_{Mn}^{\phi} y_{Al}^{\phi} (\frac{y_{Va}^{FCC} + y_{Va}^{HCP}}{2}) L_{Mn,Al:Va}^{\phi} + y_{Fe}^{\phi} y_{Si}^{\phi} (\frac{y_{Va}^{FCC} + y_{Va}^{HCP}}{2}) L_{Fe,Si:Va}^{\phi} +$$

$$y_{Mn}^{\phi} y_{Si}^{\phi} (\frac{y_{Va}^{FCC} + y_{Va}^{HCP}}{2}) L_{Mn,Si:Va}^{\phi} \quad (5\text{-}7)$$

where $L_{i,j:C,Va}^{\phi}$ is the interaction parameter for the elements in phase *Φ*, listed in Table 5-3. Parameters describing the interaction of Al and Si with C were not available for the HCP phase. Average vacancy site fractions were used for $L_{Fe,Al:Va}^{\phi}$, $L_{Mn,Al:Va}^{\phi}$, $L_{Fe,Si:Va}^{\phi}$ and $L_{Mn,Si:Va}^{\phi}$ to improve agreement with experimental SFE measurements of steels with interstitial C. For aluminium, the combined term $\Delta L_{Fe,Al:Va}^{HCP \rightarrow FCC}$ replaces $L_{Fe,Al:Va}^{\phi}$ in Equation (5-7) for the calculation of $\Delta G_{Chem}^{fcc \rightarrow hcp}$.

Table 5-3 – Thermodynamic parameters used to determine $\Delta G_{Chem}^{fcc \rightarrow hcp}$[a]

FCC phase	Ref.
${}^{0}G_{Fe:Va}^{FCC} = -236.7 + 132.416T - 24.664\,T\,ln(T) - 0.00376T^{2} - 5.893E^{-8}T^{3} + 77358.5\,T^{-1}$	[144]
${}^{0}G_{Mn:Va}^{FCC} = -3439.3 + 131.884T - 24.5177T\,ln(T) - 0.006T^{2} + 69600T^{-1}$	[144]
${}^{0}G_{Fe:C}^{FCC} - {}^{0}G_{Fe:Va}^{FCC} - G_{C}^{Gra.} = 77207 - 15.877T$	[145]
${}^{0}G_{Mn:C}^{FCC} = {}^{0}G_{Mn:Va}^{\alpha} + G_{C}^{Gra.} + 13.659T$	[142]
${}^{0}G_{Al:Va}^{FCC} = -7976.15 + 137.093\,T - 24.367\,T\,ln(T) - 1.8846E^{-3}T^{2} - 0.87766E^{-6}T^{3} + 74092\,T^{-1}$	[144]
$L_{Fe:Va,C}^{FCC} = -34671$	[145]
$L_{Mn:Va,C}^{FCC} = -41333$	[142]
$L_{Fe,Mn:C}^{FCC} = 20082 - 11.6312T$	[139]
$L_{Fe,Mn:Va}^{FCC} = -7762 + 3.865T - 259(y_{Fe} - y_{Mn})$	[137]
$L_{Mn.Al:Va}^{FCC} = -84517 + 29.999T + (-19665 + 12.552T)(y_{Mn} - y_{Al})$	[146]
$L_{Fe,Si:Va}^{FCC} = -125248 + 41.116T - 142708(y_{Fe} - y_{Si}) + 89907(y_{Fe} - y_{Si})^{2}$	[147]
$L_{Fe,Si:C}^{FCC} = 226100 - 34.25T - 202400(y_{Fe} - y_{Si})$	[148]
$L_{Mn,Si:Va}^{FCC} = -88555 + 2.94T - 7500(y_{Mn} - y_{Si})$	[149]
HCP phase	
${}^{0}G_{Fe:Va}^{HCP} = -2480.08 + 136.725T - 24.664\,T\,ln(T) - 0.00376T^{2} - 5.893E^{-8}T^{3} + 77358.5\,T^{-1}$	[144]
${}^{0}G_{Mn:Va}^{HCP} = -4439.3 + 133.007T - 24.5177T\,ln(T) - 0.006T^{2} + 69600T^{-1}$	[144]
${}^{0}G_{Fe:C}^{HCP} - {}^{0}G_{Fe:Va}^{HCP} - 0.5\,{}^{0}G_{C}^{Gra} = 52905 - 11.9075T$	[98] [145]
${}^{0}G_{Mn:C}^{HCP} = {}^{0}G_{Mn:Va}^{\alpha} + 0.5\,{}^{0}G_{C}^{Gra} - 9000 - 1.0651T$	[142]
${}^{0}G_{Al:Va}^{HCP} = -2495.15 + 135.293\,T - 24.367\,T\,ln(T) - 1.8846E^{-3}T^{2} - 0.87766E^{-6}T^{3} + 74092\,T^{-1}$	[144]
$L_{Fe:Va,C}^{HCP} = -17335$	[98] [145]
$L_{Mn:Va,C}^{HCP} = -5006$	[142]
$L_{Fe,Mn:C}^{HCP} = 21742 - 50.2703T - 32608(y_{Fe} - y_{Mn})$	[139]
$L_{Fe,Mn:Va}^{HCP} = -69.41 + 2.836T + \left((-14271.46 + 13.884T)(y_{Fe} - y_{Mn})\right)$	[98]
$L_{Mn.Al:Va}^{HCP} = -87027 + 17.154T + (-5774 + 8.786T)(y_{Mn} - y_{Al}) + (83931 - 47.279T)(y_{Mn} - y_{Al})^{2}$	[146]
$L_{Fe,Si:Va}^{HCP} = -106149 + 41.116T - 191658(y_{Fe} - y_{Si}) + 123574(y_{Fe} - y_{Si})^{2}$	[150]
$L_{Fe,Si:C}^{HCP} = unavailable$	
$L_{Mn,Si:Va}^{HCP} = -86775 + 2.94T - 7500(y_{Mn} - y_{Si})$	[151]
Other	
$\Delta G_{Si}^{fcc \rightarrow hcp} = {}^{0}G_{Si:Va}^{HCP} - {}^{0}G_{Si:Va}^{FCC} = -560 - 8T$	[96]
$\Delta L_{Fe,Al:Va}^{HCP \rightarrow FCC} = L_{Fe,Al:Va}^{HCP} - L_{Fe,Al:Va}^{FCC} = 3326$	[152]
${}^{0}G_{Mn:Va}^{\alpha} = -8115.28 + 130.059T - 23.4582T\,ln(T) - 7.3476E^{-3}T^{2} + 69827.1\,T^{-1}$	[144]
$G_{C}^{Gra.} = -17368.441 + 170.73T - 24.3T\,ln(T) - 4.723E^{-4}T^{2} + 2562600\,T^{-1} - 2.643E^{8}T^{-2} + 1.2E^{10}\,T^{-3}$	[144]

[a]Values in J mol^{-1}.

The magnetic contribution to the Gibbs energy of a phase is described by the model proposed by Inden [100] as modified by Hillert and Jarl [99]:

$$G_{Mag}^{\phi} = RTln\left(\beta^{\phi} + 1\right)f^{\phi}\left(\tau^{\phi}\right) \tag{5-8}$$

The term β^{Φ} is the magnetic moment of phase Φ divided by the Bohr magneton μ_b and given by Equations (5-9) and (5-10) [96].

$$\beta^{FCC} = 0.7x_{Fe} + 0.62x_{Mn} - 0.64x_{Fe}x_{Mn} - 4x_C \tag{5-9}$$

$$\beta^{HCP} = 0.62x_{Mn} - 4x_C \tag{5-10}$$

The term $f^{\phi}\left(\tau^{\phi}\right)$ is a function of the scaled Néel temperature $\tau^{\phi} = T/T_{Neel}^{\phi}$, found elsewhere in the literature [3] [35] [144] [99] [100]. The Néel temperature for the FCC phase of Fe-Mn-Al-Si steels is described by King and Peters [132] as:

$$T_{Neel}^{FCC} = 199.5 + 6.0X_{Mn} - 10.4X_{Al} - 13X_{Si} \qquad \text{(K)} \tag{5-11}$$

where X is the wt.% of the individual elements and for the HCP phase by Huang [137] as:

$$T_{Neel}^{HCP} = 580x_{Mn} \qquad \text{(K)} \tag{5-12}$$

In Equation (5-12), x_{Mn} is the molar fraction of Mn. If the lattice parameters of the materials are unknown, they may be estimated as a function of composition and temperature from equations listed in reference [35].

At room temperature (25°C), the model predicts ($\Delta G_{Chem}^{fcc\rightarrow hcp} + \Delta G_{Mag}^{fcc\rightarrow hcp}$) to be -88 J mol^{-1} for the alloy with 22%Mn. This is a reasonable value, considering thermal ε_{hcp}-martensite is not present, yet mechanical ε_{hcp}-martensite forms upon deformation. Thermal ε_{hcp}-martensite typically occurs when ($\Delta G_{Chem}^{fcc\rightarrow hcp} + \Delta G_{Mag}^{fcc\rightarrow hcp}$) < -100 J mol^{-1} [96] while mechanical ε_{hcp}-martensite is generally observed in Fe-Mn based alloys where ($\Delta G_{Chem}^{fcc\rightarrow hcp} + \Delta G_{Mag}^{fcc\rightarrow hcp}$) is

negative [17]. Thermal ε_{hcp}-martensite forms in a similar alloy (Fe-20Mn-3Al-3Si wt.%) with slightly less Mn content [1]. At 25%Mn, the term ($\Delta G_{Chem}^{fcc\rightarrow hcp} + \Delta G_{Mag}^{fcc\rightarrow hcp}$) is 31 J mol^{-1} and the dominant secondary deformation mechanism is mechanical twinning [1]. These results are consistent with previous observations that Fe-Mn based alloys with negative or positive values of ($\Delta G_{Chem}^{fcc\rightarrow hcp} + \Delta G_{Mag}^{fcc\rightarrow hcp}$) tend to exhibit strain-induced ε_{hcp}-martensite or mechanical twinning, respectively [17].

Figure 5-8 displays the trends in $2\rho\Delta G_{Chem}^{fcc\rightarrow hcp}$, $2\rho\Delta G_{Mag}^{fcc\rightarrow hcp}$ and $\sigma^{\gamma/\varepsilon}$ as a function of Mn content. The chemical contribution, $2\rho\Delta G_{Chem}^{fcc\rightarrow hcp}$, increases with increasing Mn content from 22 to 28 wt.%, exhibiting a slight concave up trend due to the stabilizing effect that Mn has on the FCC phase relative to the HCP. For the compositions analyzed, the increase in $2\rho\Delta G_{Chem}^{fcc\rightarrow hcp}$ is ~3 mJ m^{-2} per wt.% Mn, agreeing well with the experimentally observed SFE between 22 and 25 wt.% Mn. The calculation of $2\rho\Delta G_{Chem}^{fcc\rightarrow hcp}$ was also performed using the thermodynamic parameter $L_{Fe,Mn:Va}^{HCP}$ proposed by Djurovic at al. [139] (dashed line in Figure 5-8). However, the calculated value of $2\rho\Delta G_{Chem}^{fcc\rightarrow hcp}$ using the $L_{Fe,Mn:Va}^{HCP}$ proposed by Nakano and Jacques [98] more closely agreed with the present experimental SFE measurements.

The HCP phase in each alloy is in the paramagnetic state at RT (the Néel temperatures are 123, 137 and 153K for the 22, 25 and 28% Mn alloys, respectively, based on Equation (5-12). Consequently, the influence of antiferromagnetic ordering on the HCP phase is insignificant at RT and $G_{Mag}^{HCP} \approx 0$ J mol^{-1} for the three alloys. The FCC phases of the alloys with 22 and 25% Mn are paramagnetic at RT (Néel temperatures are 267 and 282K, respectively) while the FCC phase of the 28%Mn has a Néel temperature of ~298K based on Equation (5-11). The calculated

values of G_{Mag}^{FCC} are -26, -34 and -45 J mol^{-1} for the 22, 25 and 28%Mn alloys, respectively. Therefore, $2\rho\Delta G_{Mag}^{fcc\rightarrow hcp}$ is small and increases from 1.5 to 2.6 mJ m^{-2} with increasing Mn content (see Figure 5-8). For the present range of Mn content, the term ($2\rho\Delta G_{Chem}^{fcc\rightarrow hcp} + 2\rho\Delta G_{Mag}^{fcc\rightarrow hcp}$) increases by 3.2 mJ m^{-2} per wt.% Mn, a slight increase compared to the rise due only to the chemical contribution. As Fe-Mn based alloys are cooled below T_{Neel}^{FCC}, the influence of antiferromagnetic ordering on properties such as electrical resistance and stiffness are gradual [48] [106] [132]. Accordingly, increasing T_{Neel}^{FCC} through room temperature by additions of Mn should produce only a gradual stabilization of the FCC phase due to magnetic ordering as the model currently predicts. However, $\Delta G_{Mag}^{fcc\rightarrow hcp}$ becomes large for alloys that are cooled significantly below T_{Neel}^{FCC} [3] and partially counteracts the reduction in $\Delta G_{Chem}^{fcc\rightarrow hcp}$ with cooling. This explains why low deformation temperatures (-25 and -100°C) are required to form sufficient quantities of ε_{hcp}-martensite in the 25 and 28%Mn alloys. The sensitivity of the SFE to temperature becomes less below T_{Neel}^{FCC} [98] due to the competing nature of $\Delta G_{Chem}^{fcc\rightarrow hcp}$ and $\Delta G_{Mag}^{fcc\rightarrow hcp}$. The Néel transition of most high-Mn TWIP and TRIP steels (especially those with Al and Si additions) is slightly below room temperature [48], save for the Fe-22Mn-0.6C wt.% grade [4]. Interestingly, stabilization of the FCC phase due to antiferromagnetic effects still occurs, owing to the gradual nature of this transition [4] [48] [106] [132].

5.4 Interfacial Energy Calculation and Behavior

In each alloy the interfacial energy is the major component of the SFE. The term $\sigma^{\gamma/\varepsilon}$ is 9.2 ±1.6, 8.6 ±1.7 and 11.8 ±2.7 mJ m^{-2} for the Fe-22/25/28Mn-3Al-3Si alloys, respectively, from

Equation (1-15). The uncertainty of $\sigma^{\gamma/\varepsilon}$ is obtained from the root sum square of the uncertainties of γ_{exp} and $2\rho E_{str}$ then dividing this quantity by two. Using the same methodology, interfacial energy values were calculated for binary Fe-16/18/20/25Mn, Fe-18Mn-0.6-0/1.5Al and Fe-18Mn-0.6C-0/1.5Si alloys from existing data in the literature. The calculation of $\sigma^{\gamma/\varepsilon}$ used values of γ_{exp} reported by Volosevich et al. [79] (Fe-16/18/20/25Mn), Kim et al. [15] (Fe-18Mn-0.6-0/1.5Al) and Jeong et al. [16] (Fe-18Mn-0.6C-0/1.5Si). Values of E_{str} were calculated using lattice parameters in references [55] and [56] and the procedure outlined in Chapters 1 and 5. Lattice parameters of the FCC and HCP phase of the Fe-18Mn-0.6C-0/1.5(Al/Si) alloys were assumed to be equal to the binary Fe-18Mn alloy for the purpose of calculating E_{str}. The shear modulus and Poisson's ratio used in the calculation of E_{str} are provided in Table 5-2. The values of $2\rho(\Delta G_{chem}^{fcc\rightarrow hcp} + \Delta G_{Mag}^{fcc\rightarrow hcp})$ were determined with the thermodynamic model developed in section 5.3. A summary of some of the parameters used in the calculation of $\sigma^{\gamma/\varepsilon}$ are listed in Table 5-2. The interfacial energies of the Fe-18Mn-0.6C-0/1.5(Al/Si) range from 8.6 to 11.5 mJ m^{-2} and are consistent with a range of 8.6 to 11.8 mJ m^{-2} for the Fe-22/25/28Mn-3Al-3Si alloys. Interstitial C segregation may influence the experimental SFE measurements but is not accounted for in $\Delta G_{Chem}^{fcc\rightarrow hcp}$ and $\Delta G_{Mag}^{fcc\rightarrow hcp}$ (due to the assumption of homogenous compositions). Therefore, Mosecker and Saeed-Akbari [17] proposed that the effects of interstitial segregation on γ_{exp} would be accounted for in the calculation of $\sigma^{\gamma/\varepsilon}$. However, no substantial differences in the calculated values of $\sigma^{\gamma/\varepsilon}$ are observed between the Fe-22/25/28Mn-3Al-3Si and Fe-18Mn-0.6C-0/1.5(Al/Si) alloys, suggesting the influence of segregation on the SFE measurements is minor. The calculated interfacial energies of the binary Fe-16/18/20//22/25Mn wt.% alloys range from 15.7 to 32.5 mJ m^{-2} and are higher than for the other alloys. A comparison of the interfacial energies of Fe-22/25Mn and Fe-22/25Mn-3Al-3Si

indicates an offset of ~3 mJ m^{-2}. One explanation for the offset is that values of γ_{exp} [79] used in the interfacial calculation are higher than the actual values (as previously discussed) and therefore result in an overestimate of the interfacial energies for the binary Fe-Mn alloys. However, the trend in γ_{exp} vs. Mn reported by Volosevich at al. [79] is similar to other works [35] [153] and provides confidence that the general trend in $\sigma^{\gamma/\varepsilon}$ (which is calculated from γ_{exp}) with changes in Mn content reflects the actual behavior.

In Figure 5-9, the values of $\sigma^{\gamma/\varepsilon}$ are plotted as a function of $2\rho(\Delta G_{chem}^{fcc\rightarrow hcp} + \Delta G_{Mag}^{fcc\rightarrow hcp})$ for all alloys. The dependence of $\sigma^{\gamma/\varepsilon}$ on $2\rho(\Delta G_{chem}^{fcc\rightarrow hcp} + \Delta G_{Mag}^{fcc\rightarrow hcp})$ is consistent with parabolic behavior. In general, as $\left|2\rho(\Delta G_{chem}^{fcc\rightarrow hcp} + \Delta G_{Mag}^{fcc\rightarrow hcp})\right|$ increases, the term $\sigma^{\gamma/\varepsilon}$ also increases, indicating the interfacial energy is strongly related to $\left|\Delta G_{Chem}^{fcc\rightarrow hcp} + \Delta G_{Mag}^{fcc\rightarrow hcp}\right|$. Conversely, as $\left|\Delta G_{Chem}^{fcc\rightarrow hcp} + \Delta G_{Mag}^{fcc\rightarrow hcp}\right|$ approaches 0, where both FCC and HCP phases are equally favored, the resulting energy increase at the interface should be near a minimum, as is observed. Therefore, $\sigma^{\gamma/\varepsilon}$ can be approximated as a parabolic function of $2\rho(\Delta G_{Chem}^{fcc\rightarrow hcp} + \Delta G_{Mag}^{fcc\rightarrow hcp})$ with a minimum at $\sigma_{min}^{\gamma/\varepsilon}$:

$$\sigma^{\gamma/\varepsilon} = c(2\rho(\Delta G_{Chem}^{fcc\rightarrow hcp} + \Delta G_{Mag}^{fcc\rightarrow hcp}))^2 + \sigma_{min}^{\gamma/\varepsilon} \quad (\text{mJ m}^{-2}) \tag{5-13}$$

where *c* is a constant determined from fitting to experimental values. The term $\sigma_{min}^{\gamma/\varepsilon}$ is 9.5 mJ m^{-2} and results from the minimum fit for the Fe-22/25/28Mn-3Al-3Si and Fe-18Mn-0.6C-0/1.5(Al/Si) alloys. The constant "c" of 0.01 was determined by fitting a curve (dotted line in Figure 5-9) to the trend in $\sigma^{\gamma/\varepsilon}$ as a function of $2\rho(\Delta G_{Chem}^{fcc\rightarrow hcp} + \Delta G_{Mag}^{fcc\rightarrow hcp})$ for the Fe-Mn-Al-Si, Fe-Mn-Al-C and Fe-Mn alloys.

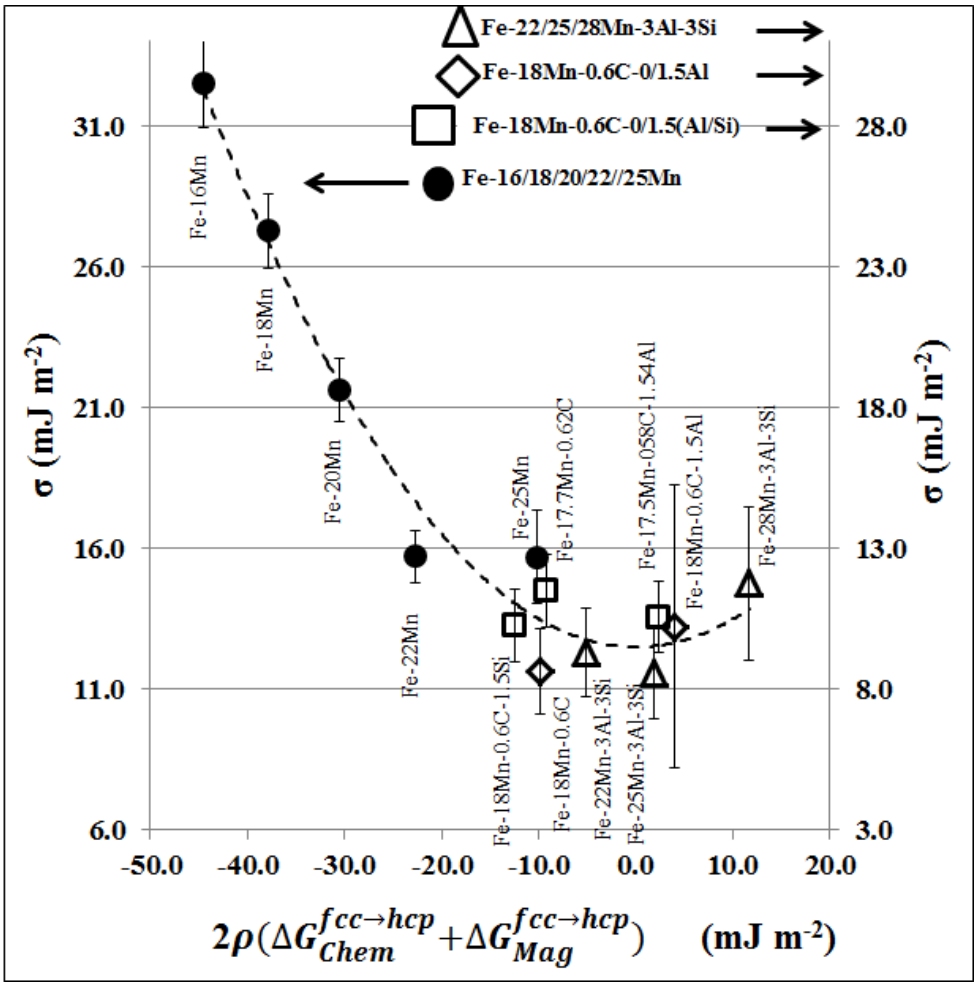

Figure 5-9 –Interfacial energy plotted as a function of $2\rho(\Delta G_{Chem}^{fcc\rightarrow hcp} + \Delta G_{Mag}^{fcc\rightarrow hcp})$ for Fe-22/25/28Mn-3Al-3Si, Fe-16/18/20/22/25Mn and Fe-18Mn-0.6C-0/1.5(Al/Si) wt.% steels. The dashed line represents the fit of the calculated interfacial energies.

Non-monotonic behavior of $\sigma^{\gamma/\varepsilon}$ as a function of composition has been reported by other authors. Cotes et al. [135] showed that $\sigma^{\gamma/\varepsilon}$ varies as a function of Mn content for binary Fe-Mn alloys and can be approximated as an upward opening parabolic curve, with a minimum $\sigma^{\gamma/\varepsilon}$ occurring between 20 and 25 wt.% Mn. Mosecker et al. [17] reported a similar behavior for the Fe-Mn-Cr-N system, where $\sigma^{\gamma/\varepsilon}$ displays parabolic behavior with additions of nitrogen from 0.2 to 0.9 wt.%. These studies provides additional confidence that the underlying cause of the parabolic behavior

is due to the relationship between $\sigma^{\gamma/\varepsilon}$ and $\left|\Delta G_{Chem}^{fcc\rightarrow hcp} + \Delta G_{Mag}^{fcc\rightarrow hcp}\right|$ as proposed in the present work.

5.5 Model Validation

The thermodynamic model was used in conjunction with the empirical relationship for $\sigma^{\gamma/\varepsilon}$ to predict values of γ_{exp} and compare them with values from the literature. The calculated values of γ_{exp} (note: the calculated value includes $2\rho E_{str}$) are 16.7 and 28.9 mJ m^{-2} for Fe-18Mn-0.6C-0/1.5Al alloys and exhibit good agreement with experimental values of 13±3/30±10 mJ m^{-2} [15] and 19.3±2.5/29.1±2.5 mJ m^{-2} [16], respectively. Jung and De Cooman [46] reported mechanical twinning in an Fe-18Mn-0.6C-2.5Al alloy. The calculated values of γ_{exp} and γ_{∞} for this alloy are 40.4 and 34.8 mJ m^{-2} which is in the SFE range for mechanical twinning as reported by Allain et al. [34]. The calculated SFE values are reasonable for C contents up to 0.6 wt.%. In addition, the present SFE measurements for the Fe-22/25/28Mn-3Al-3Si alloys give confidence that the model is valid for Al additions up to 3 wt.%.

The range of Si for which the model is valid was tested by predicting T_0 temperatures (in this work the T_0 temperature is defined as the average of the ε-martensite start (Ms) and austenite start (As) temperatures and corresponds to ($\Delta G_{Chem}^{fcc\rightarrow hcp} + \Delta G_{Mag}^{fcc\rightarrow hcp}$) = 0) of ternary Fe-Mn-Si alloys and comparing them to experimental values reported by Cotes et al. [150] [154]. The results of this comparison are reported in Table 5-4. Analysis of the data indicate that good agreement is achieved between the experimental and calculated T_0 temperatures (within 7%) for Si additions up to ~6 wt.% in ternary Fe-Mn-Si alloys. At high Mn contents (28-29 wt.%), a

greater deviation (~11-13%) is observed in the predicted vs. experimental T_0 temperatures. Therefore, the model is valid for a range of Mn content from 16 to 29 wt.% [98]. Jeong et al. [16] reported SFE measurements of 19.8 ±2.5 and 13.8 ±2.5 mJ m^{-2} for paramagnetic Fe-18Mn-0.6C and Fe-18Mn-0.6C-1.5Si wt.% alloys, respectively, finding that additions of Si resulted in a decrease of 3.5 mJ m^{-2} per wt.%. The current thermodynamic model predicts values of γ_{exp} of 17.0 and 15.4 mJ m^{-2} for the same alloys, corresponding to a decrease in γ_{exp} of ~1 mJ m^{-2} per wt.% addition of Si. Tian and Zhang [140] experimentally measured a decrease γ_{exp} of ~2.5 mJ m^{-2} per wt.% addition of Si in Fe-32Mn-0/4.6Si-0.2C alloys. Whereas the current model improves upon previous thermodynamic models which report an increase in SFE for small additions of Si, the present thermodynamic model would likely benefit from interaction parameters for Fe-Si-C for the HCP phase, an observation also shared by Jeong et al. [16]. Therefore, the model should be limited to Si concentrations of up to 1.5 wt.% for alloys with C contents of ~0.6 wt.%.

Table 5-4 – Experimental and predicted T_0 temperatures for Fe-Mn-Si ternary alloys.

	As (K)[1]	Ms (K)[1]	(As+Ms)/2[1] (K)	Calculated (As+Ms)/2 (K)	% diff[2]	T_{Neel}^{FCC} (K)[3]	T_{Neel}^{HCP} (K)[3]	$\Delta G_{chem}^{fcc\rightarrow hcp}$ (J mol^{-1})[4]	$\Delta G_{mag}^{fcc\rightarrow hcp}$ (J mol^{-1})[4]
Fe-17.5Mn-1.9Si	490	436	463	470	2	283	101	-6.0	6.0
Fe-17.4Mn-4.5Si	508	448	478	506	6	217	98	-1.1	1.1
Fe-19.5Mn-2.0Si	480	420	450	454	1	297	112	-8.6	8.6
Fe-22.2Mn-4.0Si	479	410	444.5	449	1	268	125	-5.1	5.1
Fe-24.2Mn-1.9Si	465	399	432	403	-7	336	140	-25.2	25.2
Fe-24.5Mn-4.2Si	465	396	430.5	421	-2	280	138	-8.2	8.1
Fe-26.5Mn-4.7Si	459	376	417.5	394	-6	282	149	-10.7	10.7
Fe-22.9Mn-6.1Si	470	402	436	455	4	222	127	-1.8	1.8
Fe-24.4Mn-6.4Si	464	379	421.5	433	3	226	135	-2.3	2.3
Fe-27.0Mn-5.9Si	453	363	408	387	-5	256	150	-6.8	6.8
Fe-19.9Mn-1.1Si	469	408	438.5	440	0	324	116	-15.2	15.2
Fe-22.1Mn-1.0Si	459	399	429	417	-3	344	129	-25.2	25.2
Fe-22.8Mn-2.8Si	468	401	434.5	429	-1	303	130	-11.4	11.4
Fe-28.4Mn-0.99Si	416	280	348	304	-13	390	165	-201.5	201.5
Fe-28.8Mn-4.74Si	443	351	397	353	-11	296	161	-20.9	20.9

[1]From references **[150]** and **[154]**
[2]Difference between calculated and experimental T_0 temperatures
[3]T_{Neel}^{FCC} and T_{Neel}^{HCP} calculated from [98] and [137], respectively.
[4] $\Delta G_{chem}^{fcc\rightarrow hcp}$ and $\Delta G_{mag}^{fcc\rightarrow hcp}$ calculated with present thermodynamic model

The values of $2\rho\Delta G_{Mag}^{fcc\rightarrow hcp}$, $2\rho\Delta G_{Chem}^{fcc\rightarrow hcp}$, $2\rho E_{str}$ and $\sigma^{\gamma/\varepsilon}$ determined in this work (Figure 5-8) provide a greater understanding of the physical phenomena behind the SFE evolution in Fe-Mn based steels. Of particular interest is the interfacial energy parameter, which is typically the largest parameter to contribute to the SFE in these materials at RT. This parameter exhibits a minimum near the point at which the Gibbs free energies of FCC and HCP phases are equal and increases when the absolute value of the term $2\rho(\Delta G_{Chem}^{fcc\rightarrow hcp} + \Delta G_{Mag}^{fcc\rightarrow hcp})$ becomes larger (see Figure 5-9). In the present Fe-22/25/28Mn-3Al-3Si steels, for Mn contents above ~ 23.5 wt.%, the terms $\sigma^{\gamma/\varepsilon}$, $2\rho\Delta G_{Mag}^{fcc\rightarrow hcp}$ and $2\rho\Delta G_{Chem}^{fcc\rightarrow hcp}$ all make positive contributions, resulting in a sharp rise of the SFE. However, for decreasing Mn content below ~23.5 wt.%, only the interfacial energy increases and makes a positive contribution to the SFE. This results in a much

flatter SFE curve or a minimum in this region, observed in both experimental [79] [80] and theoretical studies [35] [98], before a subsequent increase in SFE occurs with further reductions in Mn content.

5.6 Summary and Conclusions

In this study the effect of Mn content on the SFE was investigated by measuring dissociation widths of partial-dislocation pairs in three alloys (Fe-22/25/28Mn-3Al-3Si wt.%) using TEM. The experimental SFE values of 15 ±3, 21 ±3 and 39 ±5 mJ m^{-2} exhibit a super-linear increase in SFE from 22 to 28 wt.% Mn. The strain energy associated with the contraction in molar volume during the austenite to ε_{hcp}-martensite transformations was determined to be ~1-4 mJ m^{-2}, yielding ideal SFE values of 14±3, 20±3 and 37±5 mJ m^{-2}.

A new thermodynamic model for the Fe-Mn-Al-Si-C system is proposed which determines the chemical and magnetic components of the difference in Gibbs free energy of the FCC and HCP phases. The ideal SFE values were used in conjunction with the thermodynamic phase data to determine the FCC/HCP interfacial energies of the three Fe-Mn-(Al-Si) steels as well as Fe-Mn and Fe-Mn-C-Al/Si alloys for which experimental SFE data are available in the literature. Calculations of the FCC/HCP interfacial energy parameter yielded values ranging from 8.6 to 11.8 mJ m^{-2} for the Fe-22/25/28Mn-3Al-3Si and Fe-18Mn-0.6C-0/1.5(Al/Si) wt.% TRIP and TWIP alloys. The interfacial energy of the binary Fe-Mn alloys ranged from 15.7 to 32.5 mJ m^{-2}. The present work shows a strong correlation between the value of the interfacial energy of Fe-Mn-(Al, Si, C) steels and the difference in free energy of the FCC and HCP phases. To improve the accuracy of SFE calculations, an empirical relationship to describe the interfacial energy is

proposed for use in SFE calculations. The combined thermodynamic model and empirical relationship exhibit good agreement with the present SFE measurements, and those in the literature, making it a useful tool for the design of high-Mn TRIP/TWIP steels.

CHAPTER 6

THE INFLUENCE OF STACKING-FAULT ENERGY AND RELATIVE FCC/HCP PHASE STABILITY ON THE MICROSTRUCTURAL AND STRAIN-HARDENING EVOLUTION

A main objective of this research is to correlate the SFE and relative FCC/HCP phase stability, $\Delta G_{total}^{fcc \rightarrow hcp}$ (note: $\Delta G_{total}^{fcc \rightarrow hcp}$ is equivalent to $\left(\Delta G_{Chem}^{fcc \rightarrow hcp} + \Delta G_{Mag}^{fcc \rightarrow hcp}\right)$), to the temperature-dependent deformation mechanisms and mechanical properties. The Fe-22/25/28Mn-3Al-3Si alloys were strained in tension at RT, 100, 200, 300 and 400°C. The tests at RT and 400°C were interrupted at 0.03, 0.1, 0.18, 0.34, 0.47 (RT only) and 0.53 (RT only) plastic true strain (hereinafter referred to only as true strain) for microstructural observations by OM, TEM and XRD. Secondary deformations mechanisms such as martensitic transformation and mechanical twinning are suppressed at 400°C. Therefore, emphasis will be placed on the microstructural and strain-hardening evolution at RT and comparisons to the elevated temperature strain-hardening behavior will be made to illustrate important differences.

6.1 Strain-Hardening Behavior and Mechanical Properties

The Fe-22/25/28Mn-3Al-3Si steels exhibit an exceptional combination of strength and ductility at RT owing to intense strain-hardening. The RT true stress and strain-hardening rates vs. true strain for the 22, 25 and 28%Mn alloys are presented in Figures 6-1a and b, respectively. Three RT tests were performed for each composition and show excellent reproducibility (see Figure 6-1a). The 0.2% offset yield strengths of the 22, 25 and 28%Mn alloys are 293±3, 264±5 and

259±2 MPa, respectively. The yield strength of the 22%Mn alloy is ~12% higher than the yield strengths of the 25 and 28%Mn alloys. The rate of increase in the flow stress of the 22%Mn alloy is substantially greater than for the 25 and 28%Mn alloys up to ~0.1 true strain. Between 0.25 true strain and maximum uniform elongation (e_{unf}, as determined from the Considère criterion), the flow stress of the 22%Mn alloy is on average 73 MPa larger than the 25% Mn alloy, which is in turn ~23 MPa larger than the 28%Mn alloy. The true stress vs. true strain curves terminate at the true ultimate tensile strength (TUTS) at e_{unf}. The average TUTSs and maximum uniform elongations are 1172±19, 1136±9 and 1104±14 MPa and 72±2, 77±2 and 75±1% for the 22, 25 and 28%Mn alloys, respectively. Remarkably, the TUTSs and maximum uniform elongations of the 25 and 28%Mn alloys differ by less than 3%, despite a large difference in the SFEs (21 vs. 39 mJ m^{-2}). The tensile curves are smooth and the presence of dynamic strain aging (DSA), typically observed in high-Mn steels with greater C content [7] [14] [15] [42], is not observed here.

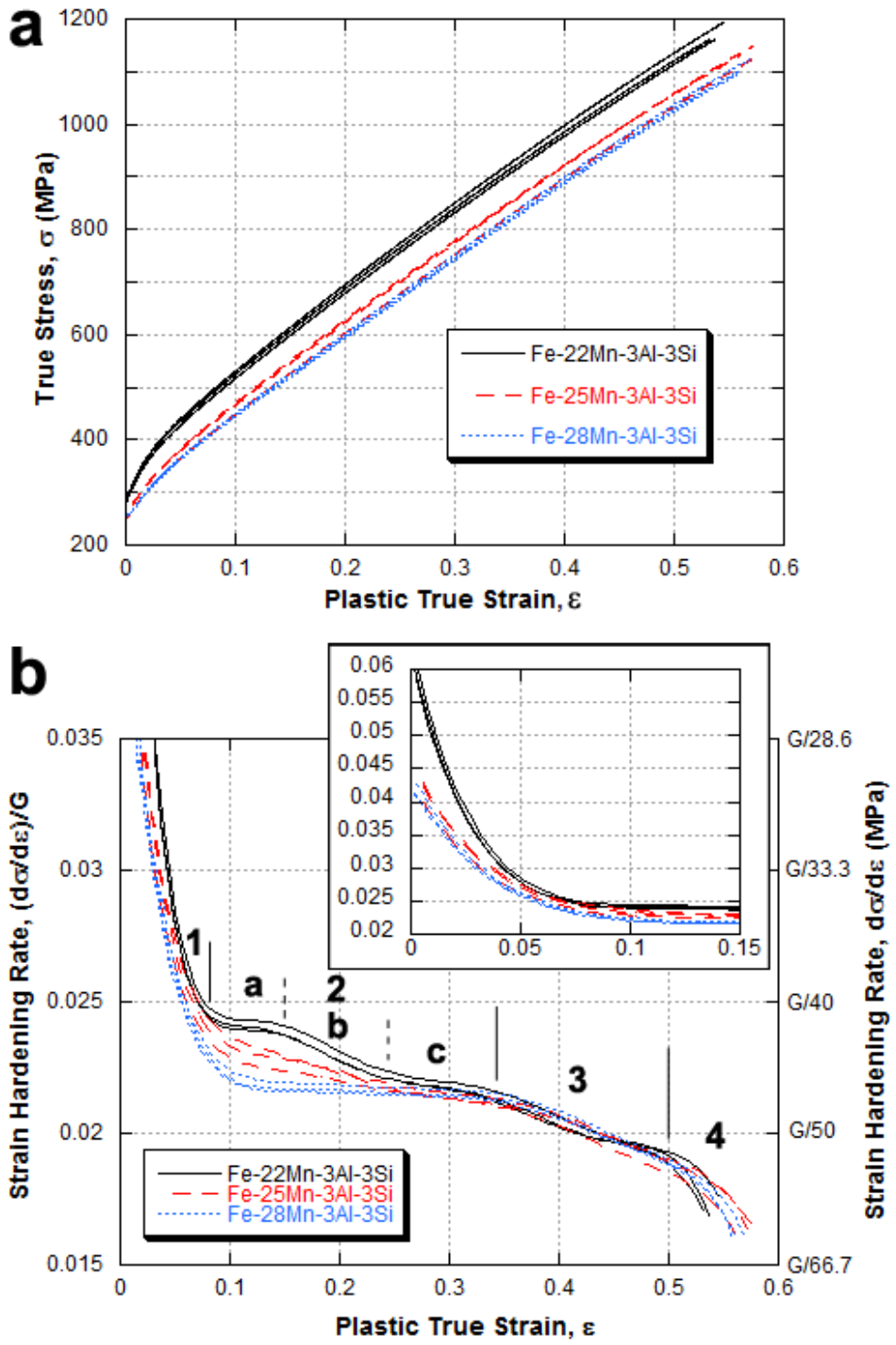

Figure 6-1 – (a) True stress vs. plastic true strain and (b) strain-hardening rate vs. plastic true strain for the Fe-22/25/28Mn-3Al-3Si steels at RT (3 tests performed for each composition). The strain-hardening stages are labeled 1-4 at their approximate locations. Stage 2 strain-hardening for the 22%Mn alloy is sub-divided into a, b and c. The inset shows the hardening rates at low strains.

Figure 6-1b displays the strain-hardening rate, $(d\sigma/d\varepsilon)/G$ (normalized by the shear modulus), vs. true strain for the 22, 25 and 28%Mn alloys at RT. The shear modulus is 69 GPa for each alloy from Appendix A. The strain-hardening rates are the derivatives of 9^{th} order polynomials which were fitted to the true stress vs true strain curves. Multi-stage work-hardening behavior, which is common in low SFE alloys that exhibit secondary deformation mechanisms [4] [14] [42] [47], is observed in the three alloys. The strain hardening rates of the 22, 25 and 28%Mn alloys decrease monotonically over the entire range which is in contrast to Fe-Mn-C [14] [42] [47] TWIP and Fe-15/20Mn-3Al-3Si TRIP steels, the latter which undergo significant $\gamma_{fcc} \rightarrow \alpha_{hcp}$ martensitic transformation [1] [2]. The 22%Mn alloy shows six distinct stages of strain-hardening (stage 2 is subdivided into a, b, and c) whereas the 25 and 28%Mn alloys exhibit four stages (note: the stages of strain-hardening described here should not be confused with classical work-hardening stages of single and poly crystals [155] [156]). In stage 1, a pronounced decrease in $(d\sigma/d\varepsilon)/G$ is observed in each alloy similar to stage III in classical work hardening of higher SFE alloys [155] [157]. The 22%Mn alloy exhibits significantly higher strain-hardening rates in stage 1, as shown in the inset in Figure 6-1b. At the onset of stage 2 (0.08 true strain), the strain-hardening rate is greatest in the 22%Mn alloy, followed by the 25%Mn alloy and then the 28%Mn alloy. The strain-hardening rate of the 25%Mn alloy shows a constant decrease from ~0.024 to 0.22 over the range of 0.08 to 0.34 true strain. In comparison, the strain-hardening rate of the 28%Mn alloy is constant at ~0.022 from ~0.12 to 0.34 true strain. All three alloys exhibit nearly identical strain-hardening rates in stage 3 (~0.34 to 0.5 true strain) which decrease from ~0.022 to 0.019. Stage 4 is characterized by an abrupt decrease in strain hardening for each alloy before maximum uniform elongation is reached.

The true stress and strain hardening rates vs. plastic true strain at 25, 100, 200, 300 and 400°C are presented in Figures 6-2a, b and c for the 22, 25 and 28%Mn alloys, respectively. As the deformation temperature is increased, secondary deformation mechanisms become energetically less favorable. In these circumstances several important changes in the strain-hardening behavior are observed: 1) the decrease in e_{unf} from RT to 100°C is most dramatic in the 28%Mn alloy with the largest RT SFE and the maximum uniform elongation of each alloy remains approximately constant from 200 to 400°C; 2) the strain-hardening rates at low strains (0 to 0.1 true strain) are nearly identical for all alloys and test temperatures, except for the RT rates of the 22 and 25%Mn alloys which are noticeably higher, indicating the deformation mechanisms at low strains are different in these two alloys at RT; 3) the strain at which the secondary deformation mechanisms begin to influence the tensile behavior is identified when the strain-hardening rate diverges from those at higher test temperatures (e.g., secondary deformation mechanisms are influencing the tensile behavior of the 28%Mn alloy only from about 0.1 true strain to failure).

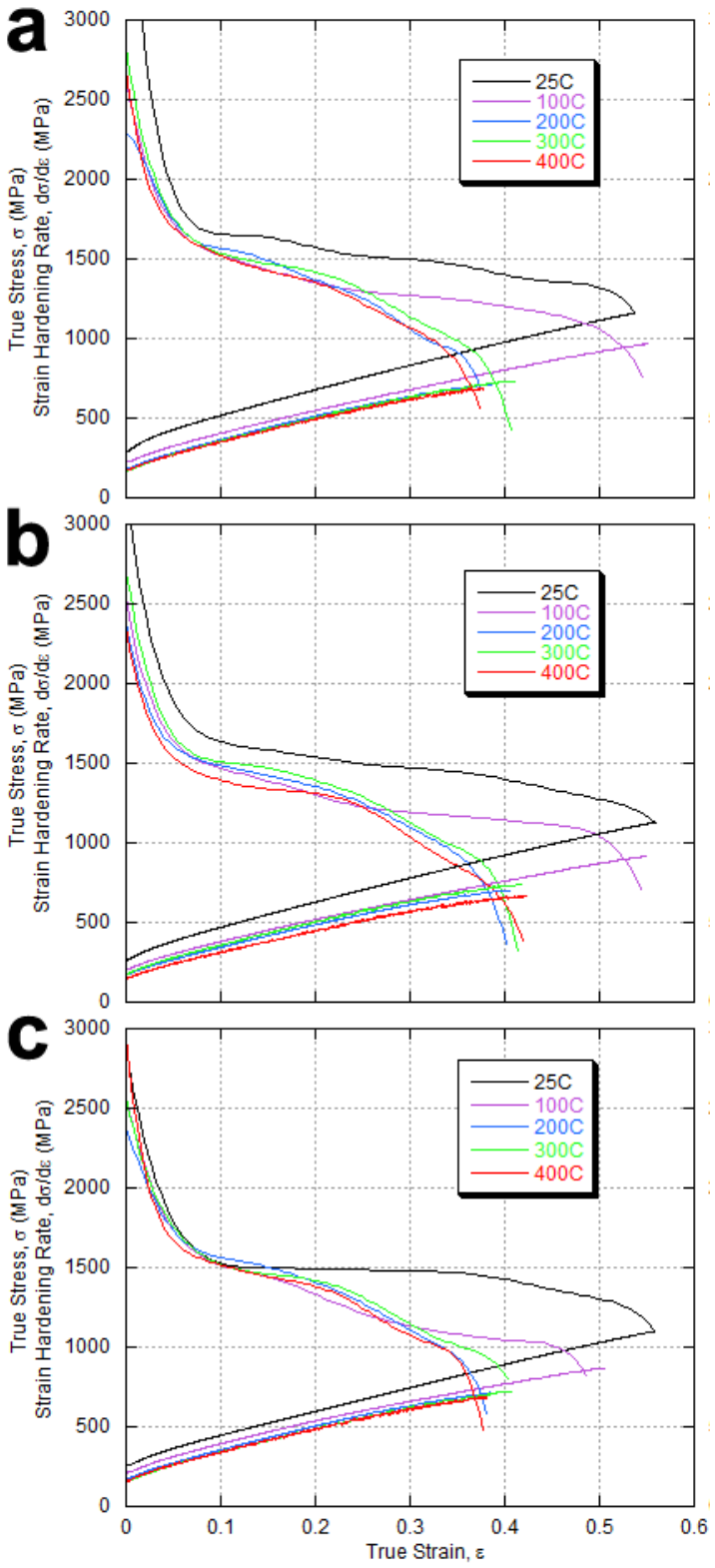

Figure 6-2 – True stress and strain-hardening rate vs true strain from tests at 25, 100, 200, 300 and 400°C for the (a) 22%Mn, (b) 25%Mn and (c) 28%Mn alloys.

The 0.2% offset yield strength, ultimate tensile strength, maximum uniform elongation and toughness (calculated from the integral of the engineering stress vs. strain curve) of the three alloys from RT to 400°C are summarized in Figures 6-3a, b, c, and d, respectively. Several important trends in the mechanical properties as a function of temperature are observed: 1) the yield strength decreases by ~108 MPa for the three alloys with increasing temperature up to 300°C, then further temperature increases up to 400°C produce minimal change in the yield strength; 2) the UTS of the 22%Mn alloy at RT is ~48 MPa larger than for the 25 and 28%Mn alloys. The UTS of each alloy is lowered by ~176 MPa when the temperature is increased from RT to 200°C but little changes occur with additional temperature increases up to 400°C; 3) the largest average uniform elongation at RT is 77±2% and occurs in the 25%Mn alloy, with slightly smaller values of 72±2 and 75±1% in the 22 and 28%Mn alloys, respectively. The decrease in maximum uniform elongation when the test temperature is increased from RT to 100°C is largest in the 28%Mn alloy (75 to 62%) and smallest in the 22%Mn alloy (72 to 69%). The maximum uniform elongation for each alloy decreases to between 45 to 47% when the deformation temperature is raised to 200°C and remains ~constant with further temperature increases up to 400°C; 4) The toughness of the 22, 25 and 28%Mn alloys at RT is 513±23, 506±9 and 470±16 mJ mm^{-3}, respectively, and exhibits a slight decrease with increasing SFE from 15 to 39 mJ m^{-2}. The toughness of each alloy is reduced by a factor of ~2.3 by increasing the test temperature from RT to 200°C.

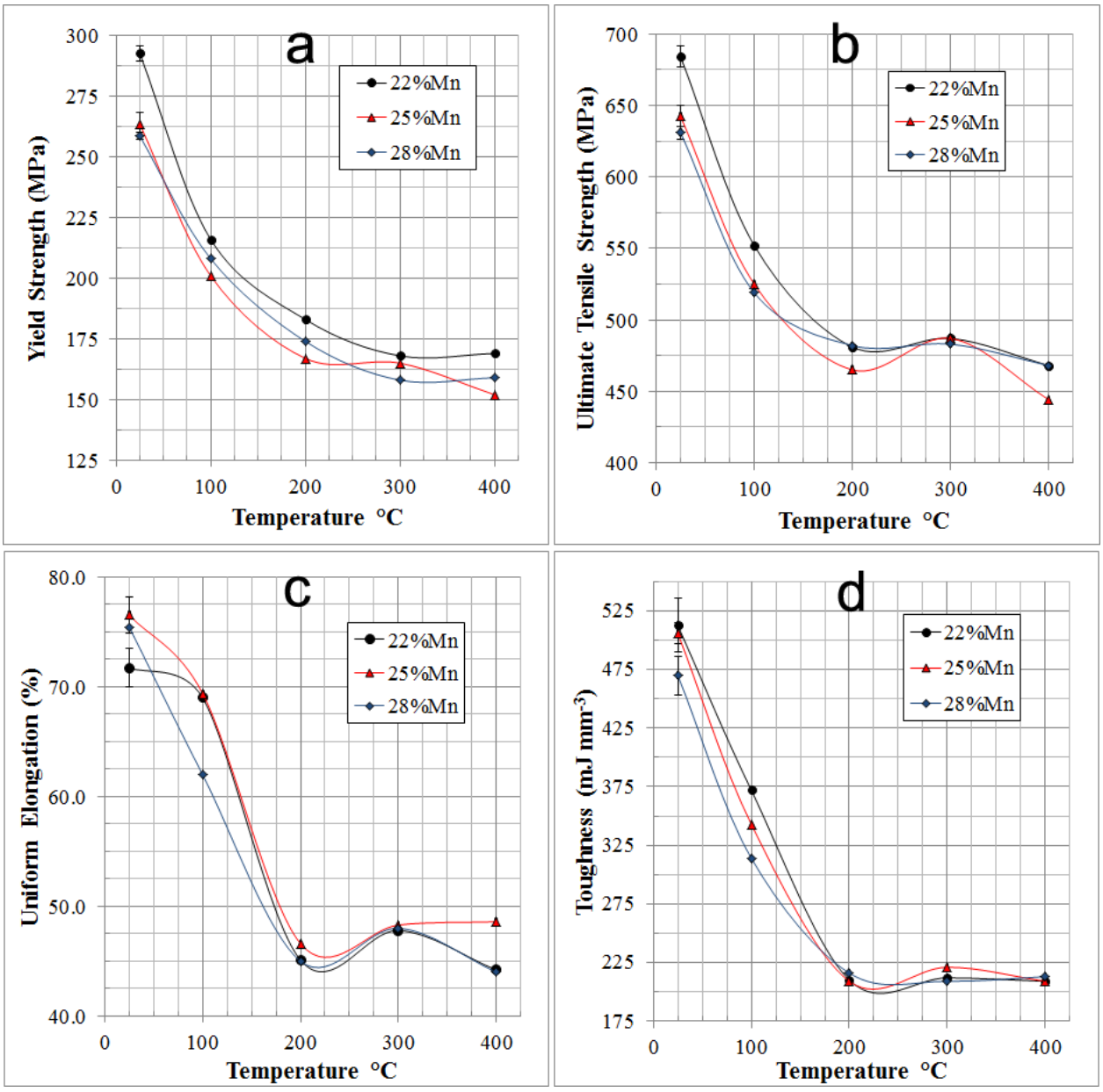

Figure 6-3 – (a) 0.2% offset yield strength, (b) UTS, (c) maximum uniform elongation and (d) toughness (energy absorption) of the Fe-22/25/28Mn-3Al-3Si steels from RT to 400 °C.

6.2 Microstructural evolution

6.2.1 X-ray diffraction

Quantitative XRD analysis determined the phases present in each specimen after deformation at RT. Phase transformations to ε- and α-martensite after deformation were detected by XRD in the 22%Mn alloy while the 25 and 28%Mn alloys were fully austenitic after deformation to maximum uniform elongation. The phase volume fractions were determined at true strains of 0.1, 0.18, 0.34, 0.47 and 0.53 and are plotted as a function of strain for the 22%Mn alloy in Figure 6-4. From 0 to 0.1 true strain the volume % of ε-martensite increases from 0 to 0.35%. From 0.18 to 0.34 true strain the volume % of ε-martensite increases from 1.4 to 3.7% and α-martensite from 2 to 10%. Figure 6-4 also displays the estimated rate of transformation of austenite to martensite, and rates of formation of ε- and α-martensite. The rates of formation of ε- and α-martensite are greatest between 0.18 and 0.34 true strain which coincides with relatively constant strain-hardening rates observed in stage 2 (Figure 6-1b).

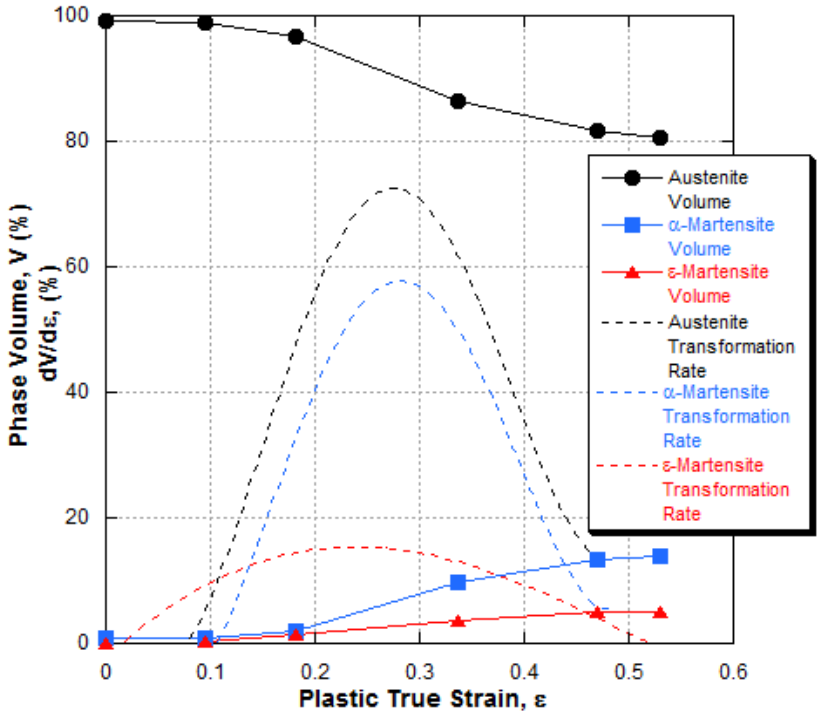

Figure 6-4 – Phase volume % (solid lines) and estimated transformation rates (dashed lines) of austenite, ε-martensite and α-martensite vs. plastic true strain for the 22%Mn alloy.

6.2.2 Optical Microscopy

Figure 6-5 shows optical micrographs of the 25%Mn alloy taken after RT deformation to 0.1, 0.18, 0.34 and 0.56 true strain (maximum uniform elongation). The tensile axis corresponds to the horizontal direction of each micrograph. Planar secondary deformation structures such as bundles of mechanical twins and/or ε-martensite laths (both of which occur in the 25%Mn alloy) correspond to lines of contrast within the grains in the optical micrographs [157]. After 0.1 true strain at RT mechanical twins and/or ε-martensite laths (TEM is required to differentiate mechanical twinning from ε-martensite) are evident in only a small percentage of grains. After 0.18 true strain at RT (Figure 6-5b) most grains show evidence of primary (occurring in only one

system) mechanical twinning and/or ε-martensite lath formation while a few grains begin to show evidence of secondary deformation structures in two or more variants (indicated by arrows). In some grains the markings are relatively few while in others they are uniformly present over the entire grain surface indicating a wide difference in volume fraction of secondary deformation mechanisms from grain to grain. After 0.34 true strain at RT nearly all grains exhibit secondary deformation mechanisms in two systems as shown in Figure 6-5c and these features are distributed over the entire grain surface in general uniformity. At maximum uniform elongation (0.56 true strain) the microstructure consists of highly elongated grains. Significant curvature of the deformation features as shown in Figure 6-5d indicates a high degree of intra-granular misorientation. In comparison, an optical micrograph (Figure 6-6) of the 25%Mn alloy deformed at 400°C to maximum uniform elongation (0.39 true strain) shows elongated grains but no evidence of planar secondary deformation structures within the grains.

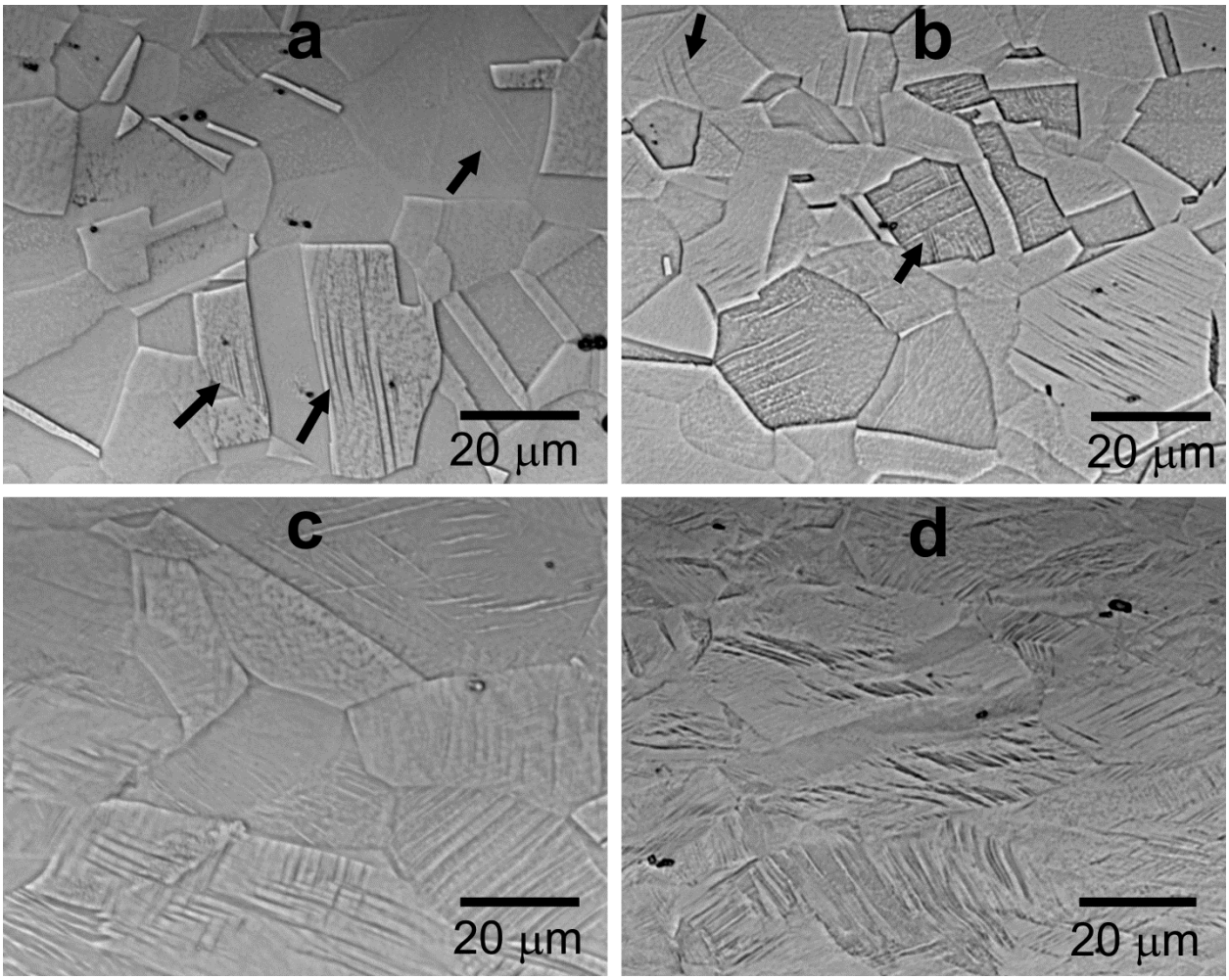

Figure 6-5 – Optical micrographs of the 25%Mn alloy. Specimens deformed at RT to (a) 0.1 (mechanical twins and or ε-martensite laths are indicated by arrows), (b) 0.18 (grains with twins and or ε-martensite laths in multiple slip systems are indicated by arrows), (c) 0.34 and (d) 0.55 true strain. The tensile axis is in the horizontal direction.

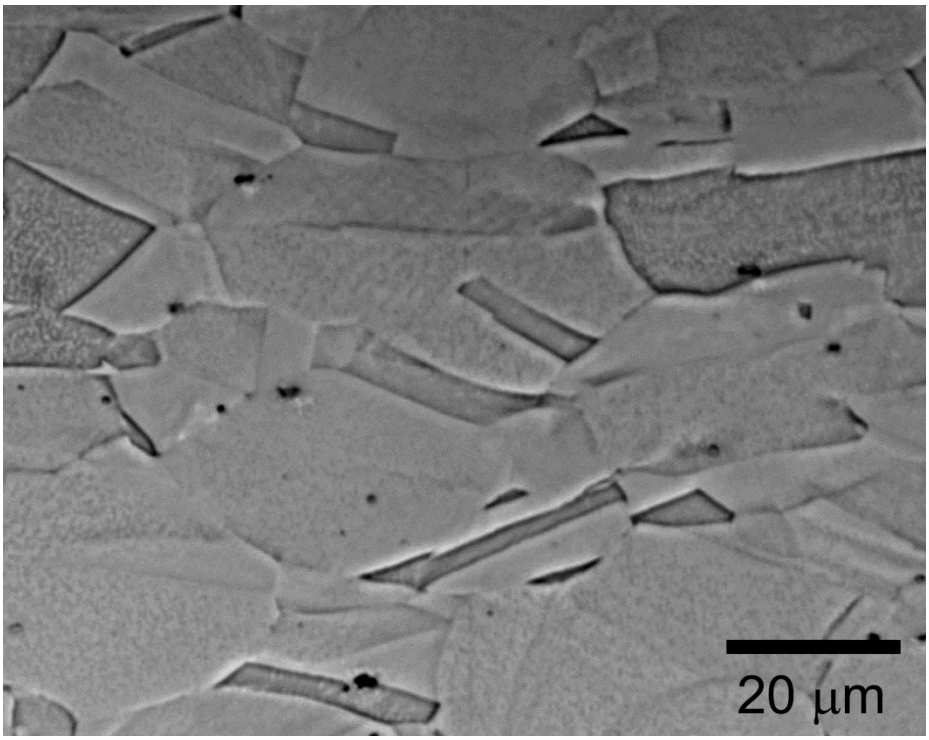

Figure 6-6 – Optical micrographs of the 25%Mn alloy after deformation to maximum uniform elongation (0.39 true strain) at 400°C.

6.2.3 TEM of specimens deformed to 0.03 true strain at RT

After 0.03 true strain at RT the microstructure of the 22%Mn alloy exhibits a planar dislocation structure of partial dislocations and large stacking faults typically activated in two systems. The stacking faults ranged in width (separation distance between the Shockley partials) from 100 nm to 2 μm in width, approximately two orders of magnitude greater than the equilibrium separation of 5 to 12 nm as determined in Chapter 5. The large surface area of the defects increases the likelihood of defects interacting with one another. These interactions were also observed in samples deformed only to the yield point (see Figure 5-2). A typical grain with a highly faulted microstructure after 0.03 true strain is shown in Figure 6-7a. Figure 6-7b was imaged near a [110] zone and shows the leading partials of stacking faults on either a (111) or (-1-11) type

plane impinging on the ε-martensite laths on (1-11) (edge on). The arrows in Figure 6-7b indicate locations where the ε-martensite laths are blocking the motion of partial dislocations. Conversely, in some areas the defects cut through one another. The microstructure of the 25% Mn alloy after deformation to 0.03 true strain at RT contains smaller stacking faults and some constricted dislocations displaying curvature or waviness as in Figure 6-7c. By comparison, the microstructure of the 28%Mn alloy after 0.03 true strain is different, consisting of isolated dislocations and localized areas of tangles of higher dislocation density, as displayed in Figure 6-7d. The majority of dislocations appeared to be constricted when viewed in the bright-field (BF) imaging mode. However, in areas of dislocation tangles, a few dislocations exhibited slight extension (<100 nm) which is likely facilitated by interaction forces from other dislocations.

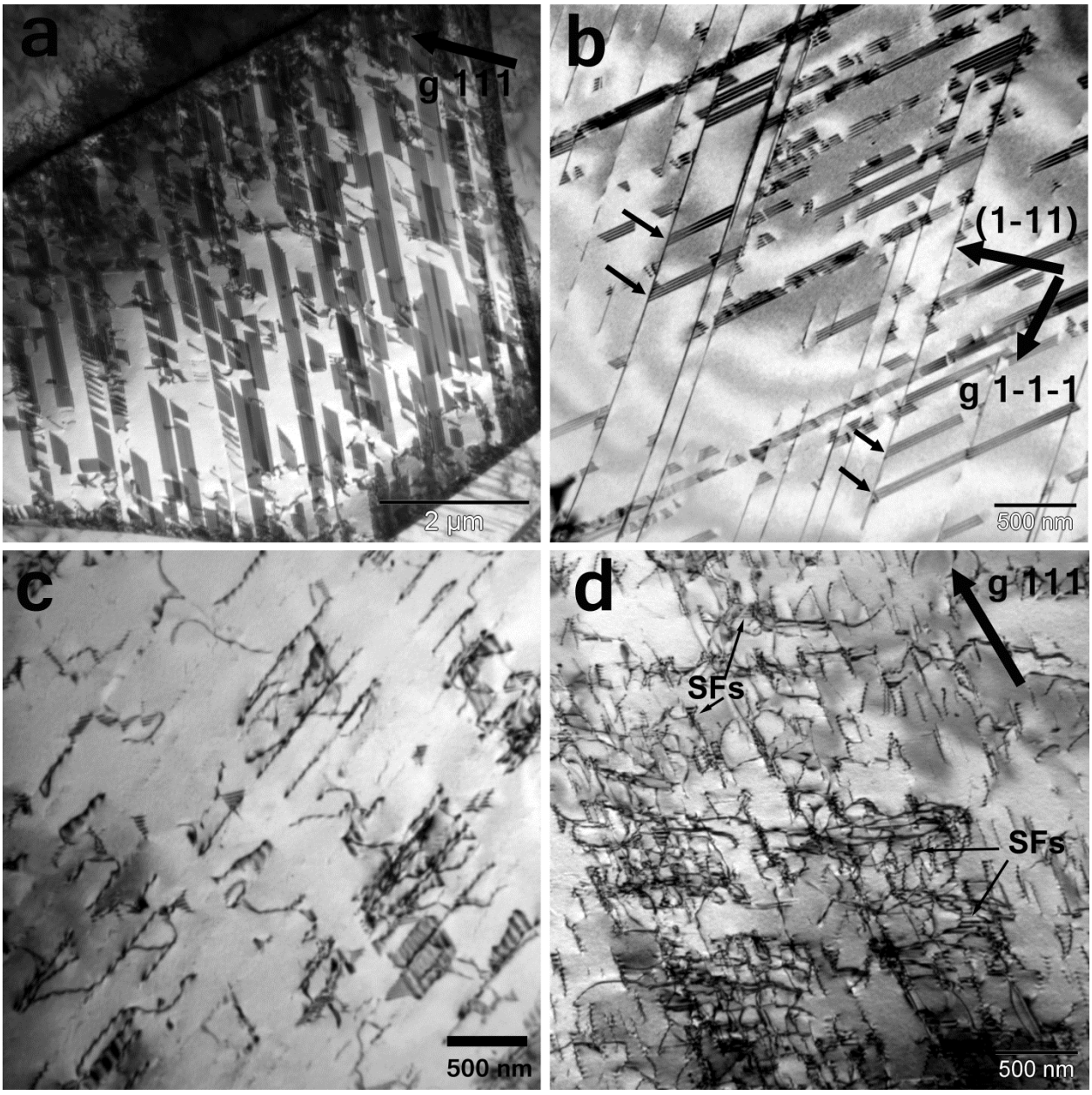

Figure 6-7 – Typical BF TEM micrographs of the Fe-22/25/28Mn-3Al-3Si alloys after 0.03 plastic true strain at RT. (a) The microstructure of a grain in the 22%Mn alloy exhibiting large stacking faults on two slip systems. (b) Image of the microstructure in the 22%Mn alloy obtained with a beam direction near [110] using a 1-1-1 g-vector showing a planar microstructure consisting of large stacking faults on either (111) or (-1-11) intersecting ε-martensite laths (edge on) on (1-11). Arrows indicate where the glide of partial dislocations is being arrested. (c) Grain exhibiting a defect structure with both planar and wavy characteristics in the 25%Mn alloy. (d) Image of the microstructure in the 28%Mn alloy taken with a 111 g-vector showing a wavy microstructure with localized areas of dislocation tangles.

6.2.4 TEM of specimens deformed to 0.1 true strain at RT

After 0.1 true strain at RT the planar microstructure of the 22%Mn alloy exhibits large, irregularly spaced overlapping stacking faults, as shown in Figure 6-8a, and more well-developed ε-martensite lath structures, Figure 6-8b. Compared to 0.03 strain, the microstructure is more refined as the spacing between individual ε-martensite laths is reduced. Figure 6-8b shows ε-martensite lath structures with the $(111)_\gamma||(0001)_\varepsilon/[1\text{-}10]_\gamma||[1\text{-}210]_\varepsilon$ orientation relationship (as indicated by the selected area diffraction pattern (SADP) in the inset) on two separate systems intersecting one another. The thickness of the ε-martensite laths is noticeably larger at 0.1 than 0.03 true strain (Figure 6-7b). In Figure 6-8b, some laths intersect each other (indicated by black arrows) while others terminate at the interface of ε-martensite laths on non-coplanar slip systems. The formation of ε-martensite is the most active secondary deformation mechanism in this steel at 0.1 true strain. A survey of twenty grains to identify which had secondary deformation structures (well developed and clearly identifiable by diffraction spots of sufficient intensity) and what type is listed in Table 6-1. In nine of twenty grains well-developed ε-martensite lath structures were observed at 0.1 true strain. The other grains contained large stacking faults but the volume fraction was not sufficient to identify by SAD.

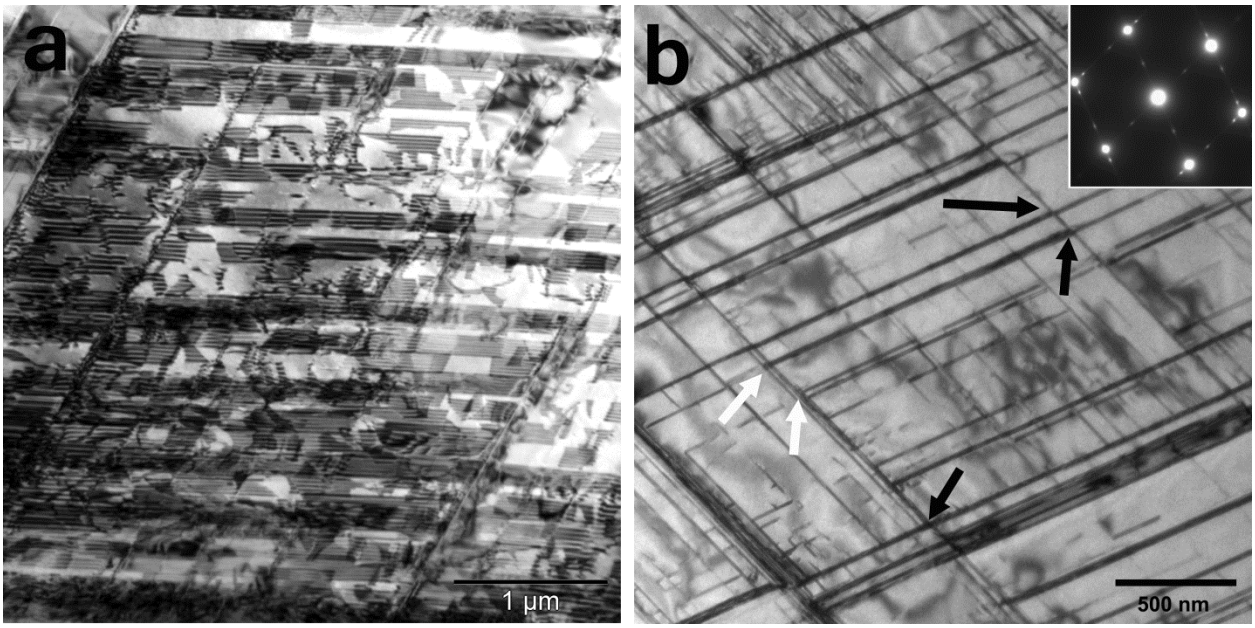

Figure 6-8 – TEM images of the 22%Mn alloy after 0.1 plastic true strain at RT. (a) BF image showing a grain with a high density of large overlapping SFs and (b) a grain exhibiting ε_{hcp}-martensite laths (see SADP inset) in two variants edge on. Arrows identify areas where laths are able to intersect each other (black) or where a lath is arresting defects on a non-coplanar {111} (white).

Table 6-1 – Number of grains after 0.1 and 0.18 true strain at RT in which well-developed ε-martensite or mechanical twinning was observed.*

True strain	Dominant secondary deformation mechanism	Material		
		22%Mn	25%Mn	28%Mn
0.1	ε-martensite	9/20	2/20	0/20
	Mechanical twinning	0/20	4/20	5/20
	Total	9/20	6/20	5/20
0.18	ε-martensite		5/14**	
	Mechanical twinning		11/14**	
	Total		14/14	

*The mechanism was determined from clearly identifiable diffraction spots of sufficient intensity.
**Two grains contained both mechanical twinning and ε-martensite in the same slip system.

The deformation structure of the 25%Mn alloy after 0.1 true strain at RT is planar and contains a high density of stacking faults, although average fault widths (separation between partial dislocations) are less than observed in the 22%Mn alloy. However, unlike in the 22%Mn alloy, mechanical twinning is the dominant secondary deformation mechanism while ε-martensite is also present but in smaller amounts. Figure 6-9a, taken near a <110> zone, shows mechanical twinning occurring in one variant at 0.1 true strain. By comparison, the ε-martensite laths in Figure 6-9b exhibit a finer structure. Of twenty grains observed by TEM, four exhibited mechanical twinning and two ε-martensite laths identifiable by SAD (Table 6-1). The TEM observations are in agreement with optical microscopy (Figure 6-5a) and indicate that the majority of grains have not developed secondary deformation structures after 0.1 true strain at RT in the 25%Mn alloy.

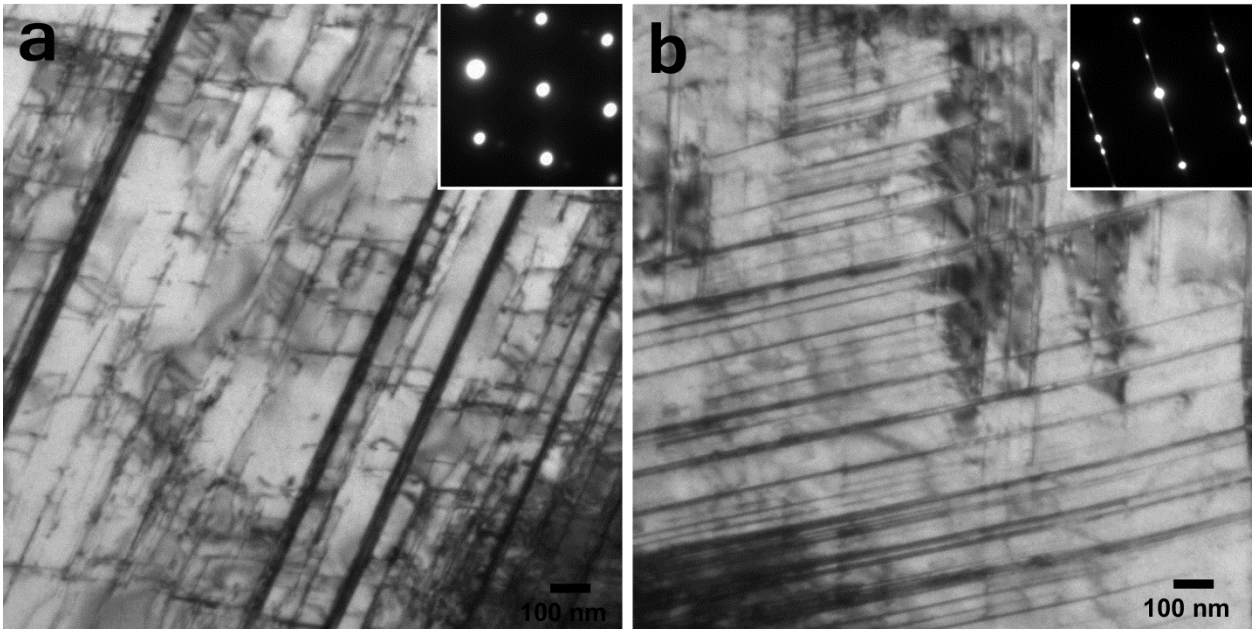

Figure 6-9 – BF images of (a) mechanical twinning and (b) fine ε-martensite lath structure with the $(111)_\gamma||(0001)_\varepsilon/[1\text{-}10]_\gamma||[1\text{-}210]_\varepsilon$ orientation relationship in the 25%Mn alloy deformed to 0.1 true strain. The SADPs were taken at a [110] beam direction for identification of secondary deformation structures.

The microstructure of the 28%Mn alloy observed by TEM after 0.1 true strain at RT exhibited a variety of different microstructural characteristics. Figure 6-10a depicts a grain exhibiting dislocation cells (DCs) where large areas (~1 μm in width) have low dislocation density and are surrounded by cell walls of much higher dislocation density. In contrast, the microstructure of a highly twinned grain is show in Figure 6-10b. The dark-field image in Figure 6-10b is formed using the {111} twin reflection as depicted in the inset SADP. Twenty grains were surveyed by TEM and five contained mechanical twinning that could be identified by SAD and none showed evidence of ε-martensite (see Table 6-1). The twins range in thickness from ~5 to 40 nm. The different microstructures observed (DCs vs mechanical twinning) are consistent with other reports of a strong relationship between grain orientation and deformation mechanism in high-Mn steels with medium SFEs [14] [21] [42].

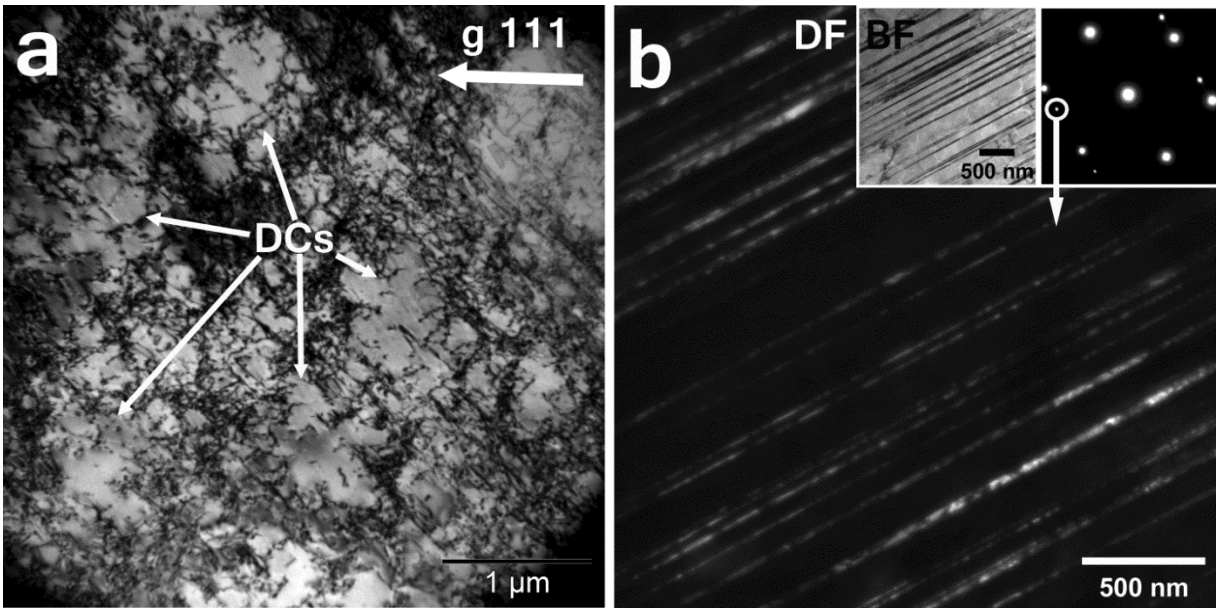

Figure 6-10 – Images of the microstructure in the 28%Mn alloy after 0.1 true strain at RT. (a) BF image of the microstructure in the 28%Mn alloy showing DCs . (b) DF image of mechanical twins in the 28%Mn using the (111) twin refection. The BF image and SADP taken from the [011] zone are shown as insets.

6.2.5 TEM of specimens deformed to 0.18 true strain at RT

Nearly all grains in the 22%Mn alloy after 0.18 true strain at RT display significant grain refinement due to the formation of ε-martensite lath structures on two or more systems. The spacing between these structures ranged from about 20 to 200 nm. Figure 6-11a depicts a grain with a particularly fine ε-martensite lath structure. Mechanical twins were not observed at this strain. In a survey of fourteen grains in the 25%Mn alloy after 0.18 true strain at RT eleven exhibited mechanical twinning and 5 showed ε-martensite laths (see Table 6-1). Nearly all grains in the 28%Mn alloy exhibit mechanical twinning after 0.18 true strain and the first observations of twinning in two systems is observed (e.g., Figure 6-11b). Mechanical twins in both variants exhibit evidence of being sheared suggesting they were active simultaneously. The twins exhibit a lenticular shape and the glide of partial dislocations is arrested at the matrix-twin interface of both twin variants.

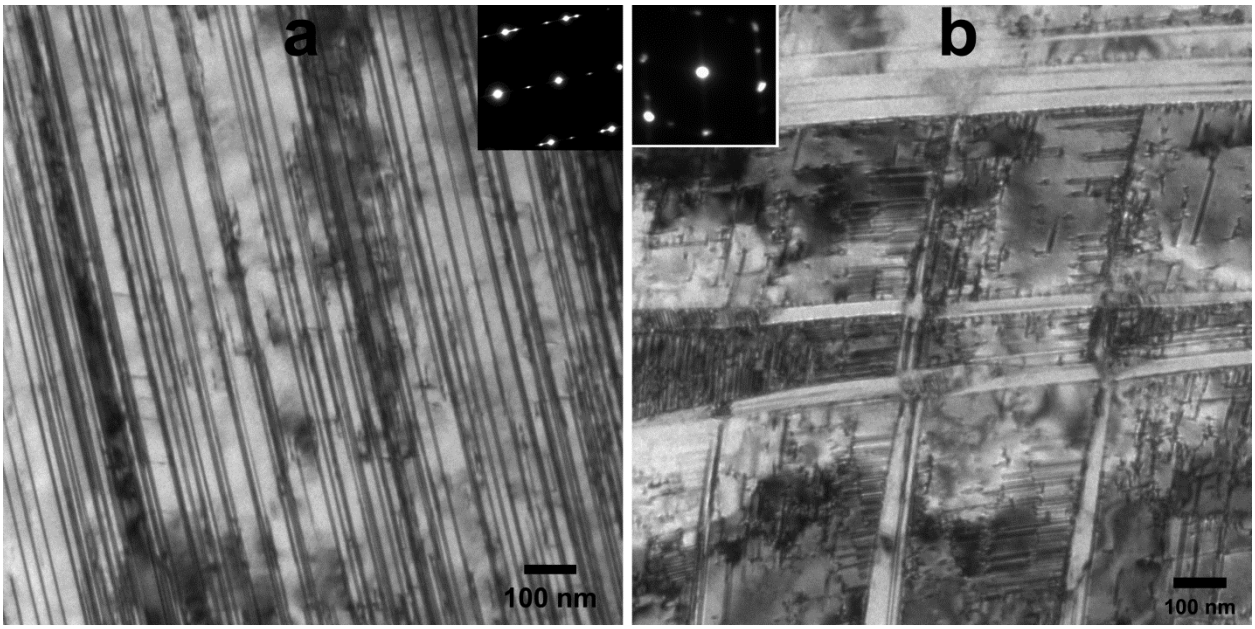

Figure 6-11 – TEM micrographs after deformation to 0.18 true strain at RT showing in (a) the 22%Mn alloy a fine ε-martensite lath structure with the $(111)_\gamma||(0001)_\varepsilon/[1\text{-}10]_\gamma||[1\text{-}210]_\varepsilon$ orientation relationship and (b) the 28%Mn alloy mechanical twinning in two variants (edge on) in the 28%Mn alloy

6.2.6 TEM of specimens deformed to 0.34 true strain at RT

The microstructure shows extensive grain refinement from secondary deformation structures after 0.34 true strain at RT in all three steels as illustrated in Figures 6-12a and b for the 22 and 28%Mn alloys, respectively. Figure 6-12a shows mechanical twinning in the 22%Mn alloy which had not been observed at lower strains. The TEM image in Figure 6-12b shows a refined microstructure consisting of mechanical twinning in two variants in the 28%Mn alloy after deformation to 0.34 true strain at RT. In several areas in Figure 6-12b the mechanical twins are bowed indicating a high degree of intra-granular lattice misorientation and inhomogeneous deformation.

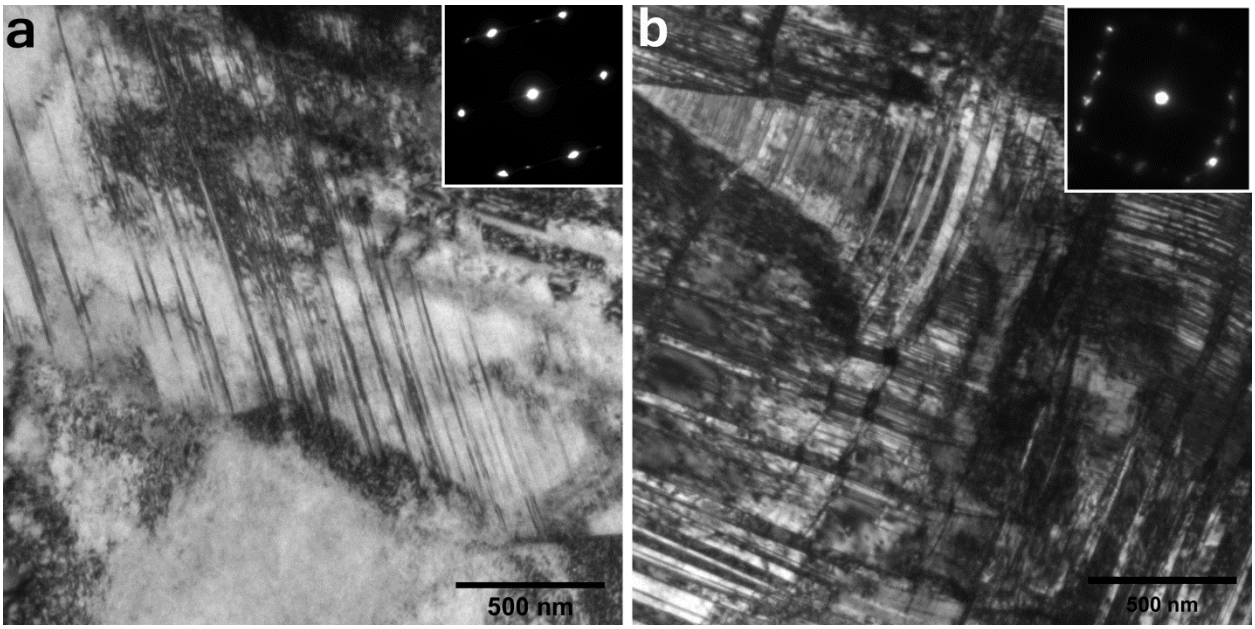

Figure 6-12 – TEM micrographs of mechanical twinning after 0.34 true strain in (a) the 22%Mn alloy and (b) two variants in the 28%Mn alloy.

6.2.7 TEM of specimens deformed at 400°C

The microstructure of the three alloys during deformation at 400°C is controlled by dislocation glide. Secondary deformation mechanisms were not observed. The TEM micrograph in Figure 6-13 of the 25%Mn alloy after 0.18 true strain shows a cellular dislocation structure but no evidence of secondary deformation mechanisms.

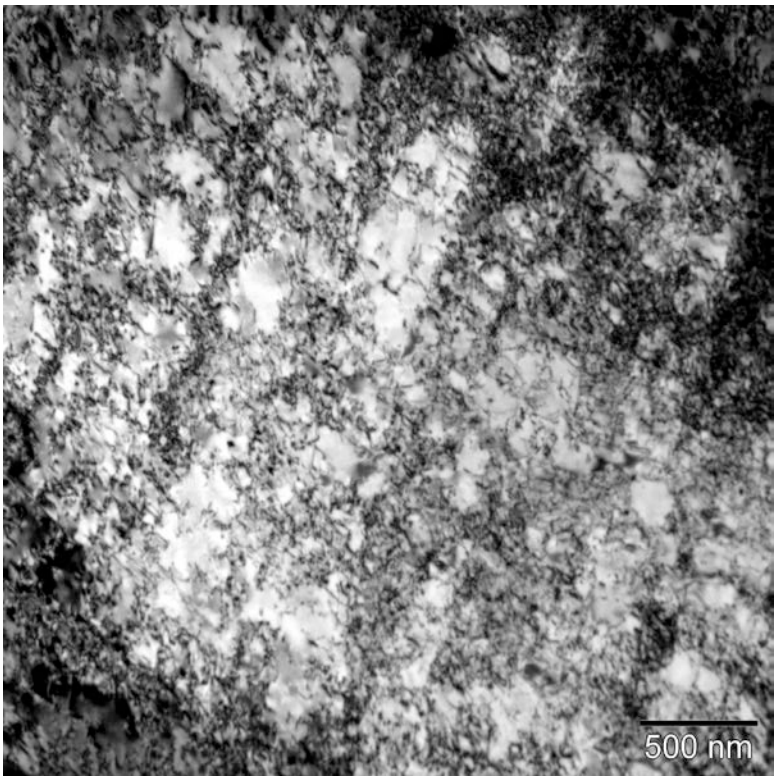

Figure 6-13 – BF TEM micrograph of the microstructure of the 25%Mn alloy after deformation to 0.18 true strain at 400°C.

6.3 Thermodynamic Evaluation of $\Delta G_{total}^{fcc \rightarrow hcp}$

Several authors have employed Equation (6-1) to calculate the SFE of high-Mn steel as a function of temperature and to predict the deformation mechanisms [3] [34] [35] [98].

$$\gamma_{exp} = n\rho\left(\Delta G_{total}^{fcc \rightarrow hcp} + E_{str}\right) + 2\sigma^{\gamma/\varepsilon} \quad (6\text{-}1)$$

However, the temperature dependencies of E_{str} and $\sigma^{\gamma/\varepsilon}$ are not well understood, leading to greater uncertainty in calculated SFE values above RT. Therefore, the prediction of the secondary deformation mechanisms could be simplified if they exhibit good correlation with $\Delta G_{total}^{fcc \rightarrow hcp}$ for different temperatures and Mn content. The value of $\Delta G_{total}^{fcc \rightarrow hcp}$ is shown in Figure 6-14 for the 22, 25 and 28%Mn alloys as a function of deformation temperature from 0 to

300°C. The maximum increase in the surface temperature of the sample due to heat generated during tensile testing is ~5°C at the point of necking just prior to failure, as measured by a thermal camera during a RT test of the 28%Mn alloy (Figure 6-15). The calculated difference in the internal temperature (the region where the TEM specimens were taken from) and surface temperature of the sample was found to be negligible. The increase in sample temperature is likely limited due to the quasi-static strain rate employed ($4x10^{-4}$ s^{-1}) and the use of sub-sized tensile specimens with greater surface to volume ratios. Consequently, the small increase in sample temperature due to deformation has been neglected. Five approximate ranges of $\Delta G_{total}^{fcc \rightarrow hcp}$, each corresponding to a set of secondary deformation mechanisms, are listed on Figure 6-14. In order of increasing value of $\Delta G_{total}^{fcc \rightarrow hcp}$, the deformation mechanisms change from: 1) glide and ε/α-martensite (-90 J mol^{-1}) to; 2) glide, ε/α-martensite and mechanical twinning (-90 to 26 J mol^{-1}) to; 3) glide, mechanical twinning and ε-martensite (~26 to 174 J mol^{-1}) to; 4) glide and mechanical twinning (~174 to 460 J mol^{-1}) and to; 5) only dislocation glide (~>460 J mol^{-1}). The ranges are established from observations of the microstructure and strain-hardening behavior of the alloys in the present work and that of other investigations on similar Fe-Mn-(Al-Si) steels (Fe-26.5Mn-2.8Al-3.0Si [2] and Fe-23.8Mn-2.7Al-3.0Si [158]). In addition, at 200°C, alloys of similar composition were reported to deform by glide only [2].

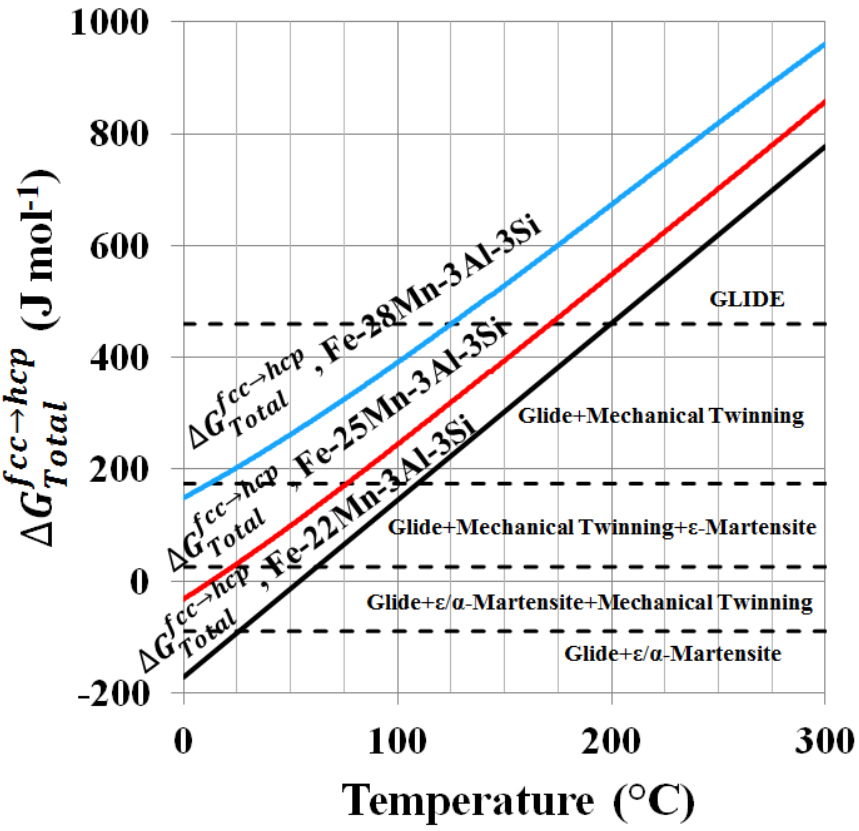

Figure 6-14 –Calculated values of $\Delta G_{total}^{fcc\rightarrow hcp}$ vs. temperature for the Fe-22/25/28Mn-3Al-3Si wt.% steels. The ranges of $\Delta G_{total}^{fcc\rightarrow hcp}$ associated with specific types of deformation mechanisms are listed.

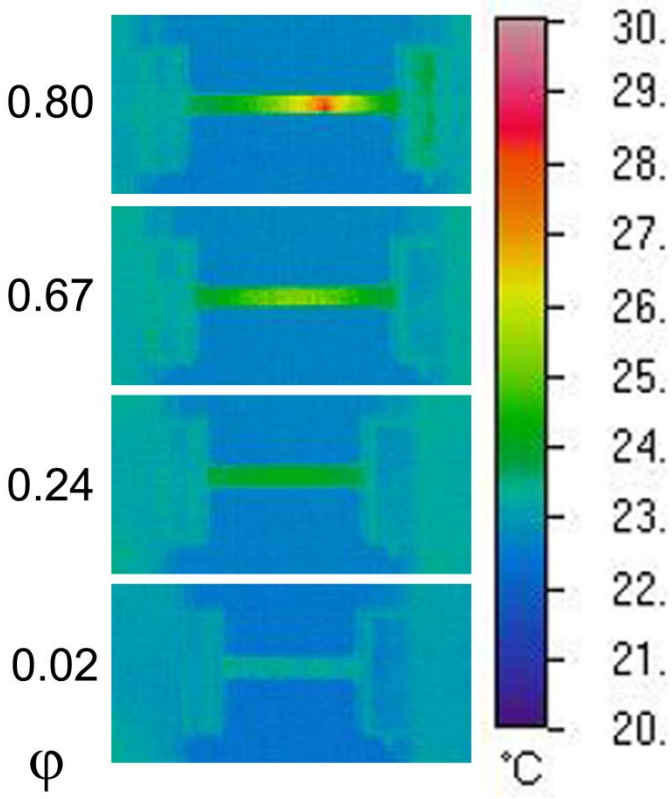

Figure 6-15 – Thermal images of a sub-sized tensile specimen during deformation of the 28%Mn alloy. The plastic strain (φ) is indicated to the left of the respective image and the temperature key is provided on the right.

6.4 Factors Influencing Yield Strength

The RT yield strength of the 22%Mn alloys is 293±3 MPa and is ~12% (~32 MPa) greater than the yield strengths of the 25 and 28%Mn alloys which are 264±5 and 259±2 MPa, respectively. Additions of Mn cause a reduction in yield strength (negative solid solution strengthening). The 25 and 28%Mn alloys are fully austenitic in the recrystallized condition and additions of Mn from 25 to 28 wt.% result in a decrease in yield strength of ~2 MPa per wt.%, agreeing well with a small decrease of 1.6 MPa per wt.% addition of Mn for Fe-xMn-2Al-0.7C (x=16,18 and 20 wt.%) alloys reported by De Cooman et al. [6]. Therefore, solid solution strengthening from Mn

reduction cannot entirely explain the difference in yield strength between the 22 and 25/28%Mn alloys. The 22%Mn alloy contains a small amount (<1 vol.%) of ordered BCC particles (5 to 10 μm in size) interspersed within the softer austenitic matrix which also contribute to the increased strength. The increase in yield strength of the 22%Mn alloy compared to the 25 and 28%Mn alloys for test temperatures from 100 to 400°C is ~6% which is still less than the 12% observed at RT. Therefore, it is proposed that the lower dislocation mobility and suppression of cross–slip in the 22%Mn alloy, which is facilitated by its low SFE (15 mJ m^{-2}), limits the possible slip systems and increases the average Taylor factor, requiring additional normal stress to initiate dislocation movement and plastic deformation. This is reinforced by microstructural observations of the 22%Mn alloy at RT where no cross slip is observed and dislocations exhibit large dissociation widths (e.g., Figures 5-2 a, b and c and 6-7 a and b). Therefore, the individual contributions to the ~32 MPa increase in yield strength of the 22%Mn alloy compared to the 25/28%Mn alloys may be attributed to the low SFE (~16 MPa), solid solution strengthening due to Mn reduction (~9 MPa) and a small volume of harder BCC particles (~7 MPa).

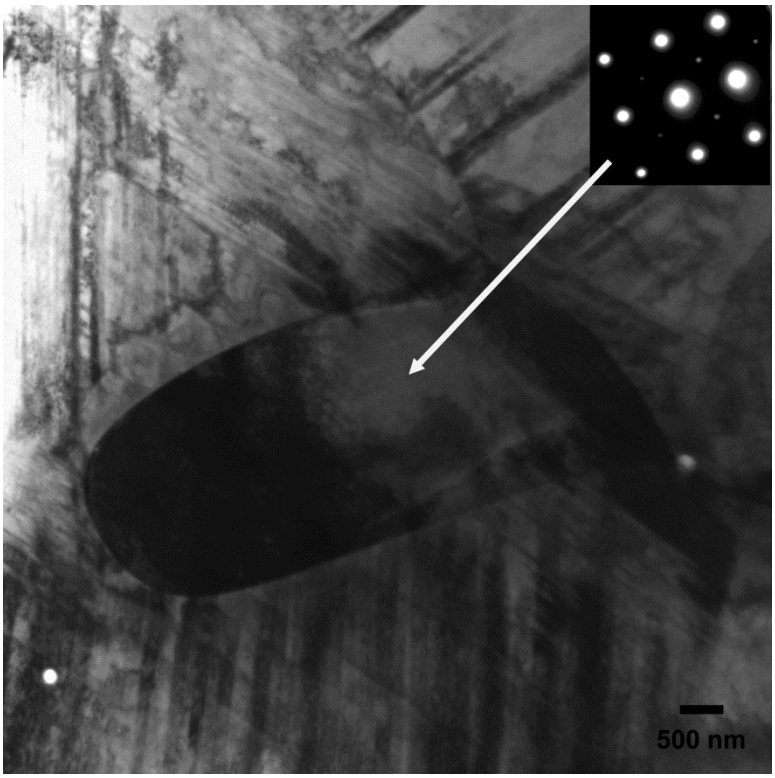

Figure 6-16 – Ordered BCC precipitate observed using a [100] zone axis in the Fe-22Mn-3Al-3Si alloy after 0.18 true strain. The inset shows the [100] BCC SAD pattern with additional spots of faint intensity arising due to the ordered structure.

6.5 Microstructural Influence on Strain-Hardening (0 to 0.1 True Strain)

Initial (stage 1, Figure 6-1b) strain-hardening is characterized by a sharp decrease in the strain-hardening rate for each alloy similar to classical stage III hardening of FCC materials [156]. The 22%Mn alloy has the lowest SFE (15 mJ m^{-2}) of the three materials and the highest RT strain-hardening rate in this stage, particularly from 0-0.03 true strain at RT as show in the inset of Figure 6-1b. The low SFE of this alloy strongly impedes cross slip and confines dislocations to single slip planes as evidenced by Figures 6-7a and b. In addition to reducing dislocation mobility by limiting cross slip, large stacking faults and ε-martensite lath structures form at low

strains (<0.03 true strain) in this alloy and serve as impediments to dislocations gliding on non-coplanar slip planes as shown in Figure 6-7b. Such extensive grain refinement at low strains due to strain-induced planar defects was observed only in the 22%Mn alloy at RT. The negative value of $\Delta G_{total}^{fcc \rightarrow hcp}$ (-88 J mol^{-1}) in the 22%Mn alloy at room temperature favors ε-martensite over mechanical twinning (see Table 6-1). Since the formation of ε-martensite does not require a critical dislocation density in the way that mechanical twinning does [20], it forms earlier in the deformation sequence. Consequently, the strain hardening of the 22%Mn alloy at low strains is superior to the 25 and 28%Mn alloys, as shown in Figures 6-1a and b. As the deformation temperature of the 22%Mn alloy is increased to 100°C, the value of $\Delta G_{total}^{fcc \rightarrow hcp}$ reaches 140 J mol^{-1} and the formation of ε-martensite is largely suppressed and a substantial decrease in the strain-hardening rate at low strains is observed (see Figure 6-2a).

The 25%Mn alloy has a SFE of 21 mJ m^{-2} and shows both planar and wavy deformation characteristics after 0.03 true strain at RT, as evidenced by staking faults and dislocations with curvature in Figure 6-7c. Wavy deformation characteristics are typically associated with greater dislocation mobility and ease of cross slip [159]. The curvature of the dislocations can be exacerbated due to glide of specific segments on different slip planes. Figure 6-7c shows some dislocations which appear constricted in BF imaging exhibiting a high degree of curvature. Wavy deformation characteristics were not observed in the 22%Mn alloy at RT. Therefore, the beginning of the transition from planar to wavy slip in these alloys coincides with an increase in SFE from 15 to 21 mJ m^{-2}. The greater dislocation mobility at low strains due to increase ability for cross slip and fewer strain-induced planar obstacles results in a lower RT hardening rate than is observed in the 22%Mn alloy at low strains (0-0.1 true strain).

The SFE of the 28%Mn alloy is 39 mJ m^{-2} and the microstructure at 0.03 true strain is more typical of a medium SFE alloy, with wavy dislocations that are predominately constricted like those in Figure 6-7d. The dislocation structure indicates that cross slip is more favorable and dislocation mobility is greater in this alloy due to a higher SFE. Consequently, the formation of dislocation tangles and areas of increased dislocation density are common, like those in Figure 6-7d, rather than the planar dislocation structure observed in the 22%Mn alloy. The RT strain-hardening rates at low strains (<0.1 true strain) in the 28%Mn alloy are slightly lower than the 25%Mn alloy and substantially lower than that of the 22%Mn alloy at RT.

Stage 1 strain-hardening has been shown to depend on material, SFE, temperature and strain-rate and is typically associated with dynamic recovery processes including cross-slip, annihilation of screw dislocations with opposite signs and the formation of low-energy dislocation structures (LEDS) like tangles and cells [19] [156] [157] [160] [161] [162] [163]. However, the hardening behavior of the present alloys in stage 1 is remarkably similar for all alloys and test temperatures, except for the 22 and 25%Mn alloys at RT, which exhibit greater strain-hardening (particularly the 22%Mn alloy). Thus, stage 1 strain-hardening in the present alloys is enhanced by lowering the SFE below 21 mJ m^{-2} , due to suppression of cross-slip and the formation of ε-martensite laths which impede glide, but is relatively insensitive to increases in SFE above 21 mJ m^{-2}, where cross slip is observed.

6.6 Microstructural Influence on Strain Hardening (0.1 to 0.34 True Strain)

After 0.1 true strain at RT in the 22%Mn alloy, ε_{hcp}-martensite laths were identified by SAD in nine of twenty grains surveyed, exhibiting significantly higher activity than mechanical twinning in the 25 and 28%Mn alloys after the same deformation. Some grains, such as the one in Figure 6-8b contained laths in multiple non-coplanar systems which serve as strong impediments to dislocations gliding in all slip systems. Even in grains where ε-martensite could not be directly identified by SAD, a high density of stacking faults was observed in multiple slip systems like that in Figure 6-8a. The formation of α_{bcc}-martensite is insignificant at this strain (see Figure 6-4). Therefore, a high density of stacking faults and the formation of ε_{hcp}-martensite is primarily responsible for the enhanced strain-hardening in stage 2a of the 22%Mn alloy at RT compared to the other compositions. This point is reinforced by the strain-hardening behavior of the 22%Mn at 100°C, where the formation of ε_{hcp}-martensite is substantially less favorable (see Figure 6-14), and stage 2a is non-existent (see Figure 6-2a). The beginning of stage 2b at RT is characterized by a 2nd inflection in the strain-hardening rate at ~0.15 true strain which leads to a decrease in the hardening rate until 0.25 true strain. The decrease is attributed to diminishing mean free path reduction. Gutierrez-Urrutia and Raabe [14] showed that the hardening of TWIP steels could be modeled in terms of a dislocation mean free path approach (where the mean free path is governed by parameters such as the spacing between mechanical twins). As the formation of new ε_{hcp}-martensite will preferentially thicken existing laths, leading to larger, more energetically favorable regions of ABAB stacking like those in Figure 6-8b, the rate of mean free path reduction will diminish [52] [53]. The onset of stage 2c occurs with a third inflection (upward) in the strain hardening rate at 0.25 true strain. This inflection coincides with the maximum rate of

α_{bcc}-martensite formation (see Figure 6-4). Grässel et al. observed a similar inflection in the strain-hardening rate that corresponded to high rates of α_{bcc}-martensite transformation in Fe15/20Mn-3Al-3Si steels [2] as did Tomota et al. in an investigation of binary Fe-Mn alloys [67].

Observations of the microstructure of the 25%Mn alloy after 0.1 and 0.18 true strain revealed ε-martensite lath structures and mechanical twinning. The ratio of grains with mechanical twins vs ε-martensite was ~2:1 and did not change significantly from 0.1 to 0.18 true strain as indicated in Table 6-1.The formation of ε-martensite is less intense in the 25%Mn alloy than in the 22%Mn alloy, resulting in lower strain-hardening rates from 0.08 to ~0.25 true strain.

From 0.12 to 0.34 true strain at RT the 28%Mn alloy exhibits a nearly constant strain hardening rate of 0.022, which is attributed to grain refinement and reduction of the mean free path of dislocation glide by both dislocation substructure evolution and mechanical twinning (see Figures 6-10a and b, 6-11b and 6-12b). Mechanical twinning plays an important role in the deformation behavior of the 28%Mn alloy, but only after 0.1 true strain and the transition from stage 1 to 2 (based on observations of the strain-hardening rates in the 28%Mn alloy from RT to 400°C, figure 6-2c). This observation is in agreement with Gutierrez-Urrutia and Raabe [14], who found that the transition from stage a to b strain-hardening of an Fe-22Mn-0.6C TWIP steel was caused by evolution of the dislocation substructure rather than mechanical twinning. However, these observations contrast with the work of Asgari et al. [157], who specifically attributed the interruption of stage 1 and the onset of stage 2 in low SFE alloys MP35N and 70/30 brass to primary mechanical twinning.

6.7 Summary and Conclusions

The influence of SFE and $\Delta G_{total}^{fcc \rightarrow hcp}$ on the microstructural and strain-hardening evolution of three Fe-22/25/28Mn-3Al-3Si alloys was investigated. Secondary deformation mechanisms such as $\alpha_{bcc}/\varepsilon_{hcp}$-martensite formation and/or mechanical twinning are activated at specific SFE and/or $\Delta G_{total}^{fcc \rightarrow hcp}$ values and strongly contribute to the excellent mechanical properties of these materials. The following conclusions were drawn from this work:

i. A SFE of 15 mJ m^{-2} (Fe-22Mn-3Al-3Si at RT) resulted in a highly planar microstructure, suppression of dislocation cross-slip, and $\alpha_{bcc}/\varepsilon_{hcp}$-martensite transformation as the dominant secondary deformation mechanism. The onset of grain refinement due to ε_{hcp}-martensite in multiple slip systems occurs from the beginning of plastic deformation and provides superior work-hardening at low strains (0-0.1 true strain). At intermediate strains (0.1-0.34 true strain), ε_{hcp}-martensite formation combined with α_{bcc}-martensite transformation provides sustained normalized strain-hardening rates from 0.024 to 0.022.

ii. For a SFE of 21 mJ m^{-2} (Fe-25Mn-3Al-3Si at RT) the dislocation structure exhibits both planar and wavy characteristics at low strains. The formation of mechanical twinning and ε_{hcp}-martensite are both observed at intermediate strains (0.1 to 0.34) and result in normalized strain-hardening rates between 0.023 and 0.022.

iii. For a SFE of 39 mJ m^{-2} (Fe-28Mn-3Al-3Si at RT) dislocations are largely constricted at low strains (0 to 0.1 true strain), ε_{hcp}-martensite is absent, and the microstructure exhibits wavy slip and the formation of dislocation cell structures. Mechanical twinning begins to influence the strain-hardening behavior at ~0.1 true strain and causes a uniform strain-hardening rate of

0.022 from ~0.12 to 0.34 true strain. The strain-hardening rates of all three alloys are nearly identical from 0.25 true strain to maximum uniform elongation.

iv. The RT TUTSs and maximum uniform elongations of the Fe-22/25/28Mn-3Al-3Si alloys are 1172±19/1136±9/1104±14 MPa and 72±2/77±2/75±1%, respectively. Increasing the SFE from 15 to 21 mJ m^{-2} (corresponding to the transition from TRIP to TWIP dominated behavior) causes a small decrease in strength and increase in ductility. Remarkably, increasing the SFE from 21 to 39 mJ m^{-2} alters the deformation mechanisms but has little effect on the mechanical properties, as strength and ductility decrease only by ~3%.

v. Increasing the deformation temperature from 25 to 200°C results in suppression of the secondary deformation mechanisms and a severe loss in strength and ductility (toughness decreases from ~ 496 at RT to ~212 mJ m^{-3} at 200°C) in all three alloys.

vi. The deformation mechanisms exhibit a strong correlation with the relative FCC/HCP phase stability, $\Delta G_{total}^{fcc \rightarrow hcp}$ (J mol^{-1}), as it is changed by increasing the temperature and/or additions of Mn. The formation of ε-martensite occurs up to values of $\Delta G_{total}^{fcc \rightarrow hcp}$=175 J mol^{-1}, while mechanical twinning is active in the range of -90 to 460 J mol^{-1}. The value of $\Delta G_{total}^{fcc \rightarrow hcp}$ may be used as a simple method to predict the deformation mechanisms of Fe-Mn-(Al-Si) steels.

CHAPTER 7

FUTURE WORK

Several areas of high-Mn steel research require additional investigation in order to further the development and understanding of these materials. A few of these areas are laid out in the following sections, including: 1) segregation of atoms at defects and interfaces; 2) the influence of SFE on the microstructural and strain-hardening behavior of Fe-Mn-Cr-C-N Steels; 3) measurement of strain fields at mechanical twin boundaries and 4) high strain-rate microstructural characterization. The present author and collaborators have begun initial investigations on some of these topics for which preliminary data is presented.

7.1 Segregation of Atoms at Defects and Interfaces in High Manganese TRIP/TWIP steels

Segregation in high-Mn steels is an important topic due to its suspected impact on mechanical properties and also due to its deleterious effects: limited post-uniform elongation [6], a negative strain-rate sensitivity [4] and surface roughness [45]. Recent results show that Fe-22/25/28Mn-3Al-3Si steels with low carbon content (200-600 ppm) exhibit dynamic strain aging (DSA) at elevated temperatures (200-500°C) and quasi-static strain rates ($4x10^{-4}$ s^{-1}). This occurrence is particularly interesting because the DSA may involve the diffusion of substitutional atoms at temperatures lower than expected. Figure 7-1 shows true stress vs. true strain curves of the Fe-25Mn-3Al-3Si alloy from RT to 400°C. Serrations in the tensile curves are observed at 200°C and intensify with increasing temperature (up to 400°C) and higher total strain. The observations suggest that vacancy-assisted diffusion of solute atoms to dislocation cores is occurring while the

dislocations are at rest, thereby pinning the dislocations and requiring an increased break-away stress to free the dislocations from their solute atmospheres. The manifestation of this phenomenon is the serrations in the tensile curves. Interestingly, in Figure 7-1, the sample deformed at 300°C exhibits greater flow stress than the sample deformed at 200°C, suggesting the DSA may also be a strengthening mechanism.

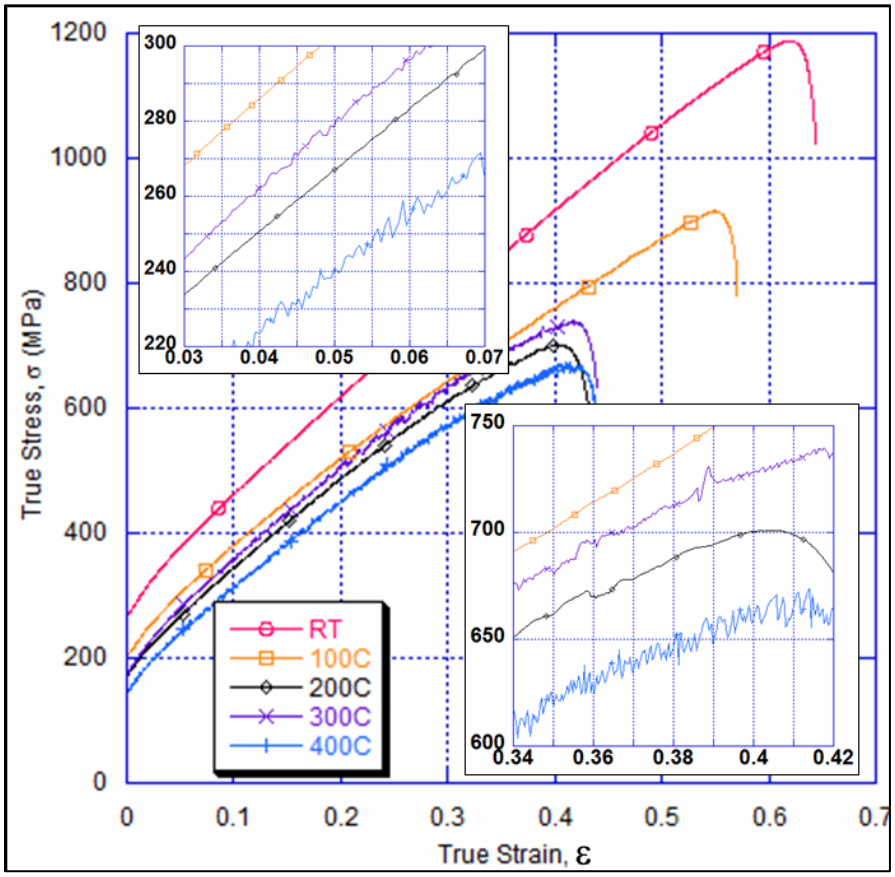

Figure 7-1 True stress vs. true strain curves for an Fe-25Mn-3Al-3Si alloy deformed at quasi-static strain rates. The insets show serrations in the flow stress at 200, 300 and 400°C.

Preliminary atom probe tomography (APT) revealed local Mn and Si concentration gradients in a Fe-25Mn-3Al-3Si alloy. Figure 7-2 shows APT data with two iso-surfaces, bounding volumes deficient (<5.3 at.%) and enriched (>8.5 at.%) in silicon, oriented parallel to each another. A

one-dimensional concentration profile (Figure 7-2b) across these iso-surfaces in the direction of the arrow in Figure 7-2a indicates inhomogeneity of both Mn and Si increasing and decreasing inversely to each other in what resembles cross-core dislocation segregation.

Future work should determine conclusively if solute atmospheres are developing around dislocation cores during high-temperature deformation and causing the DSA. Atom probe tips, fabricated from specimens that have been deformed at 400°C to 20 and 40% deformation (for sufficient dislocation density), should be observed with TEM prior to APT analysis to determine the spatial location of the dislocations, as shown in Figure 7-3. Subsequent atom probe analysis of the same tip would determine if solute atmosphere are occurring around the vicinity of dislocation cores. Performing TEM and APT on the same tip is challenging. Therefore, an alternative and less direct method to determine if segregation is occurring during high-temperature deformation could be employed. In this method, APT analysis should be performed on specimens deformed at 400°C and to different levels of strain. A substantial increase in segregation with increasing strain would indicate that diffusion is occurring during deformation. At low strains and low dislocation density, vacancy assisted diffusion to dislocation cores should be low. Conversely, at strains of 40%, the tip will have a greater dislocation density as shown in Figure 7-4, and significantly more segregation would be expected. These investigations would provide an improved understanding of the basic science involving dislocation interactions with solute atoms during plastic deformation at elevated temperatures.

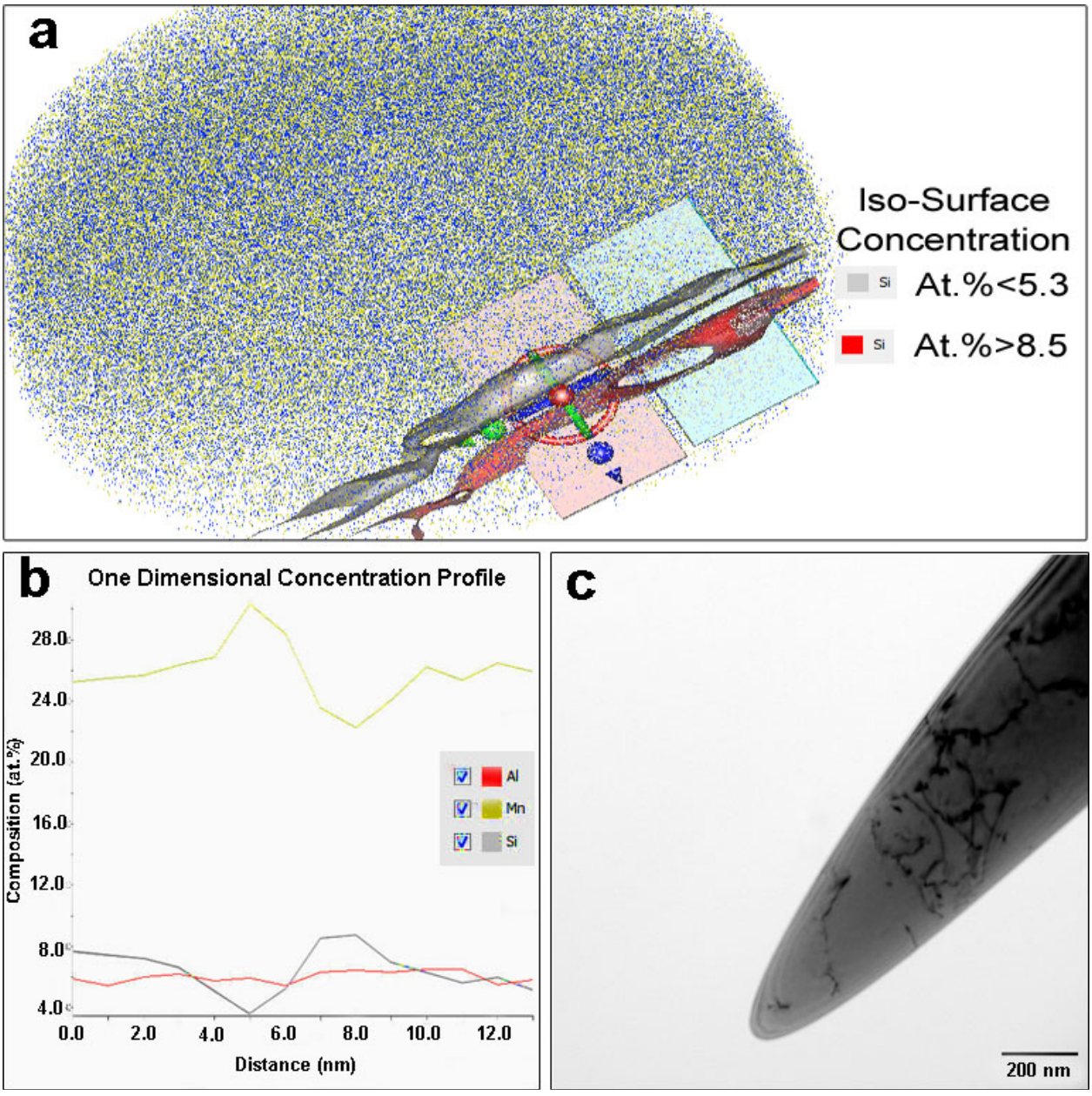

Figure 7-2 - (a) APT reproduction with iso-surfaces bounding zones deficient and enriched in Si indicated, (b) one dimensional concentration profiles across zones defined by iso-surfaces and (c) TEM image of APT tip from an Fe-25Mn-3Al-3Si alloy deformed 10% at 400°C

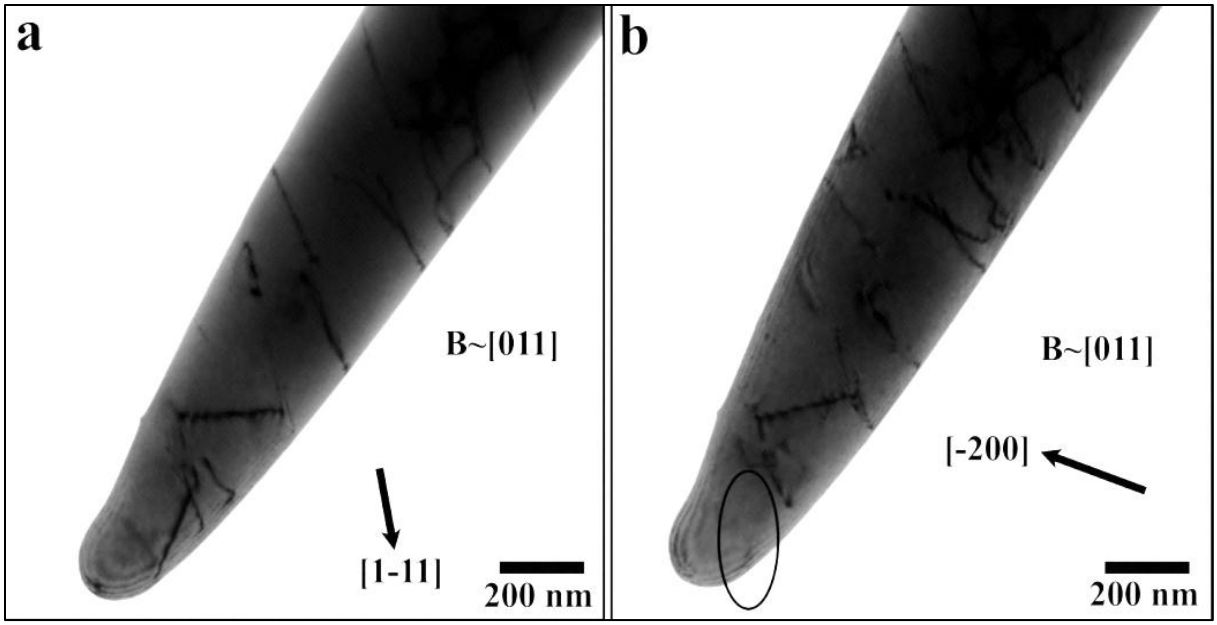

Figure 7-3 - Two-beam bright-field TEM images of dislocation structure in APT tip from an Fe-28Mn-3Al-3Si alloy deformed 3% at 400°C using (a) a [1-11] g-vector and (b) a [-200] g-vector causing the circled dislocation to go out of contrast.

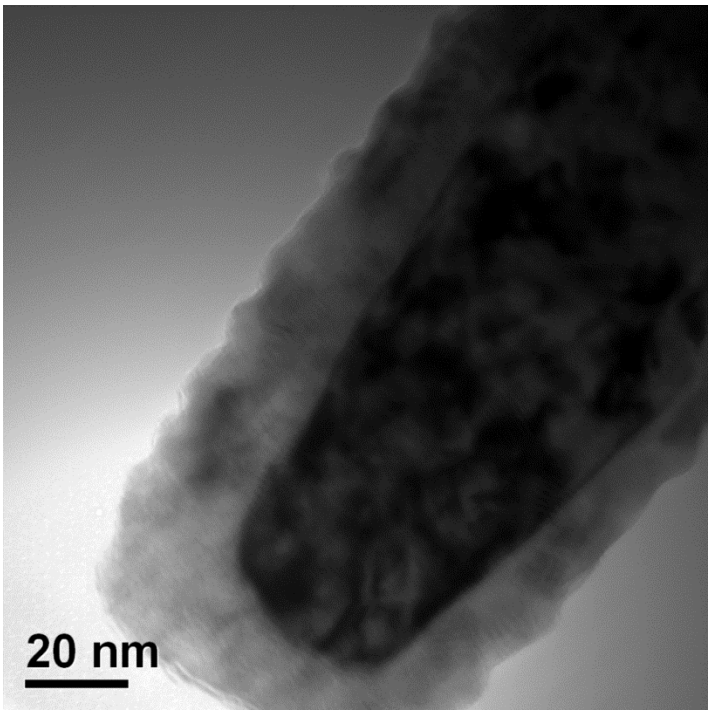

Figure 7-4 – TEM image of an atom probe tip of an Fe-28Mn-3Al-3Si deformed to 0.34 true strain

7.2 Influence of SFE on the Microstructural and Strain-Hardening Evolution in Fe-Mn-Cr-C-N Steels.

High-Mn TRIP and TWIP steels of typical Fe-Mn-(Al-Si-C) compositions are more susceptible to corrosion than Fe-Ni-Cr austenitic steels. However, new grades of Fe-Mn-Cr-C-N steels provide increased corrosion resistance over typical TWIP steels while still exhibiting good mechanical properties. Nonetheless, the compositions of these steels need to be optimized in order to achieve the optimal relative FCC/FCP phase stability to produce the best mechanical properties. This optimization involves the measurement and prediction of the SFE for these materials. Measuring the SFE using WBDF TEM to directly measure partial dislocation separations is the most accurate method. Figure 7-5 is a WBDF image showing a partial dislocation pair in an Fe-14Cr-16Mn-0.3C-0.3N steel with separations on the order of 8.3 to 10.9 nm. Initial SFE measurements indicate the SFE is within the range of 18-26 mJ m^{-2} as shown in Figure 7-6. The theoretical partial-dislocation spacing's corresponding to specific SFEs are based on Equation (1-4) using a shear modulus of 79 GPa and a Poison ratio of 0.28 (see Appendix A). A preliminary SFE value for this material is 22 mJ m^{-2}. However, additional measurements are required to achieve statistical significance. The samples for SFE measurements should only be deformed to the yield point and be given thermal treatments, similar to those described in chapter 2, in order to facilitate SFE measurements. Once additional SFE data points are obtained, the experimental SFE values can then be used to validate thermodynamic SFE models, such as that proposed by Mosecker and Saeed-Akbari for Fe-Mn-Cr-N steels [17].

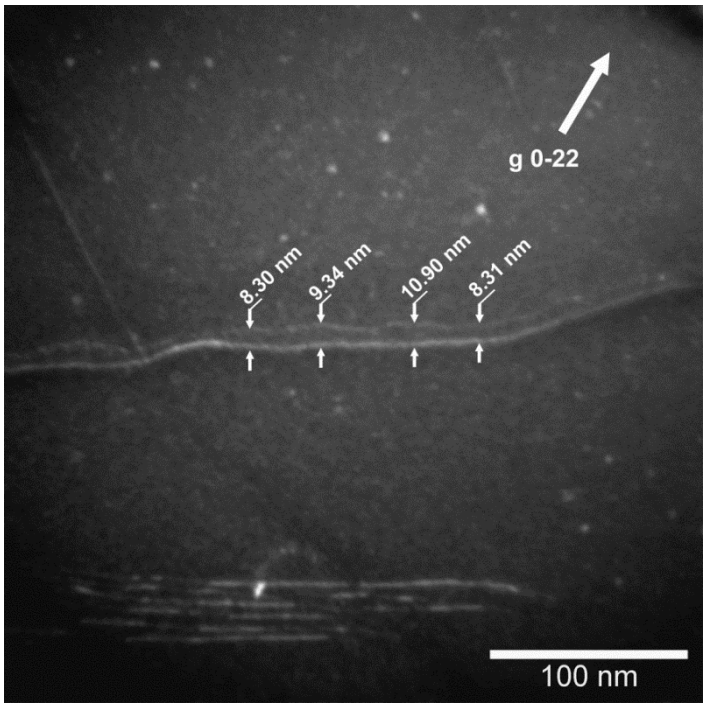

Figure 7-5 – WBDF image of Shockley partial dislocations in an Fe-14Cr-16Mn-0.3C-0.3N steel deformed 1.5%

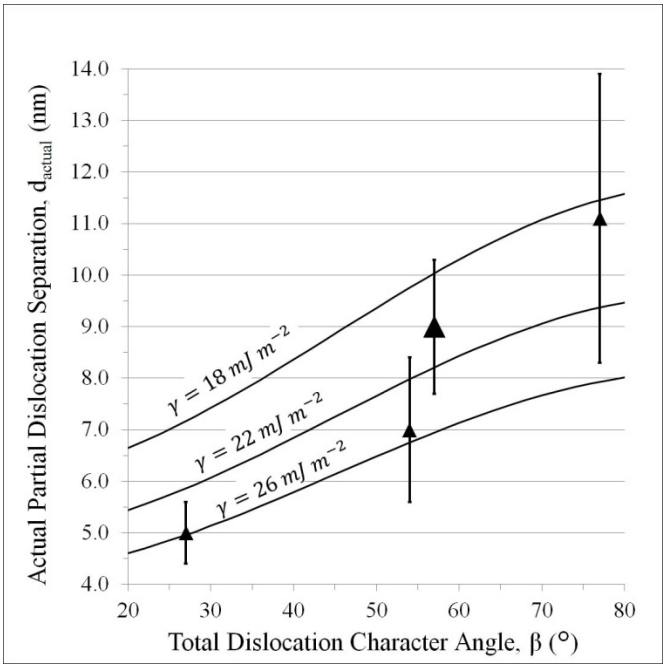

Figure 7-6 - Actual partial dislocation separations vs. character angle for an Fe-14Cr-16Mn-0.3C-0.3N steel. The larger symbol corresponds to the dislocation in Figure 7-5.

7.3 Strain Measurements at Mechanical Twin Matrix Interfaces

Mechanical twins serve as barriers to dislocation glide and TWIP steels containing carbon display significantly greater strain-hardening than Fe-Mn-Al-Si alloys. A reduction in dislocation mobility due to interstitial carbon is partially responsible for the difference in the strain hardening of the two alloys but is not a complete explanation. A recent review of high-managnese steel by Bouaziz et al. [4] suggested “a deeper analysis of the effect of carbon on strain-hardening be conducted” to investigate what appears to be an increase in the efficiency of twins as obstacles. Idrissi, et al., [36] have shown that carbon content has a significant effect on the morphology and internal dislocation structure of deformation twins. Twins in the carbon containing steels were thinner and contained more sessile dislocations than steels without carbon which may make them more effective barriers to dislocation glide. Adler et al. [38] noted that during the twinning shear previous octahedral sites would become tetrahedral sites. As a result, carbon atoms situated in the larger octahedral sites could become trapped during the shear and the conversion to a tetrahedral site. The process would repeat on successive (111) planes as the twin grew in thickness during deformation. A subsequent lattice distortion and a hardening of the twin would be expected.

A greater understanding of these defects and how they impede dislocation motion may be realized by analyzing their structure using high-resolution transmission electron microscopy (HRTEM) and making local strain measurements near the twin boundaries. Initial results have yielded important findings about the proper specimen preparation techniques, experimental procedures, and the structure of mechanical twin boundaries. Analysis of mechanical twins by HRTEM requires the twin habit plane be nearly perpendicular to the foil surface to permit

observation of the twin in the high-resolution TEM. The region of interest must be thin and free of sample bending in order to facilitate sample tilting with a computer controlled stage. Finding regions of the sample that meet these requirements is best done using conventional TEM prior to observation using HRTEM. A region of a Fe-25Mn-3Al-3Si sample suitable for HRTEM is shown in in a conventional TEM image in Figure 7-7. The mechanical twins (indicated by arrows) terminate at the sample hole where the specimen is thin. Figure 7-8 shows an atomic-resolution image of a mechanical twin in a Fe-16Mn-14Cr-0.3C-0.3N alloy deformed to 20%. These images can be used to measure the displacements of columns of atoms relative to each other to determine the strain fields near the twin boundary.

Future work should focus on comparing the strain fields near twin boundaries in TWIP steels with and without interstitial C. The Fe-16Mn-14Cr-0.3C-0.3N and Fe-22/25/28Mn-3Al-3Si alloys are well suited for this work, as they are easy to electro-polish and produce high-quality TEM samples. The samples should be deformed to about 20% to introduce a sufficient amount of mechanical twins. This work will enable a deeper understanding of the structure of mechanical twins and their interactions with dislocations and may explain why TWIP steels with C exhibit superior strength.

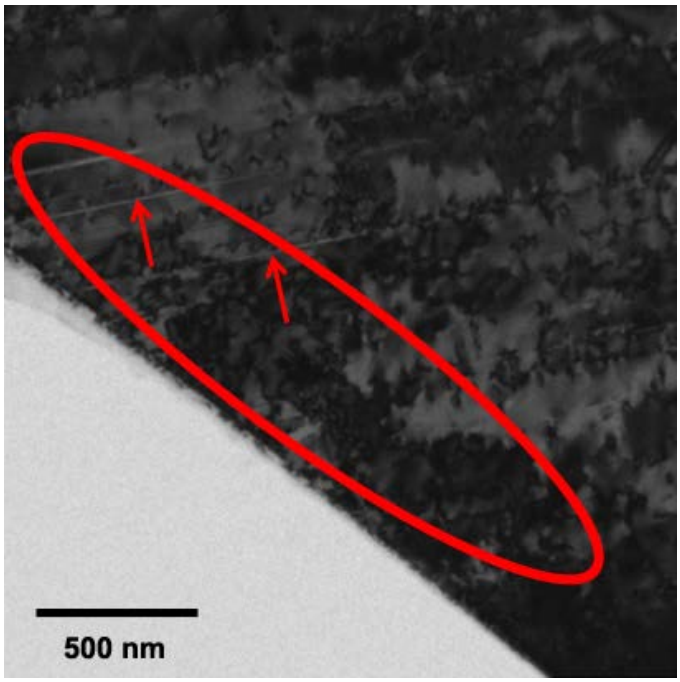

Figure 7-7 – Conventional TEM image of an area (red circle) containing mechanical twins (identified by arrows) potentially suitable (thin, free of bends, with mechanical twins terminating at the sample hole) for HRTEM in an Fe-25Mn-3Al-3Si alloy deformed 20%.

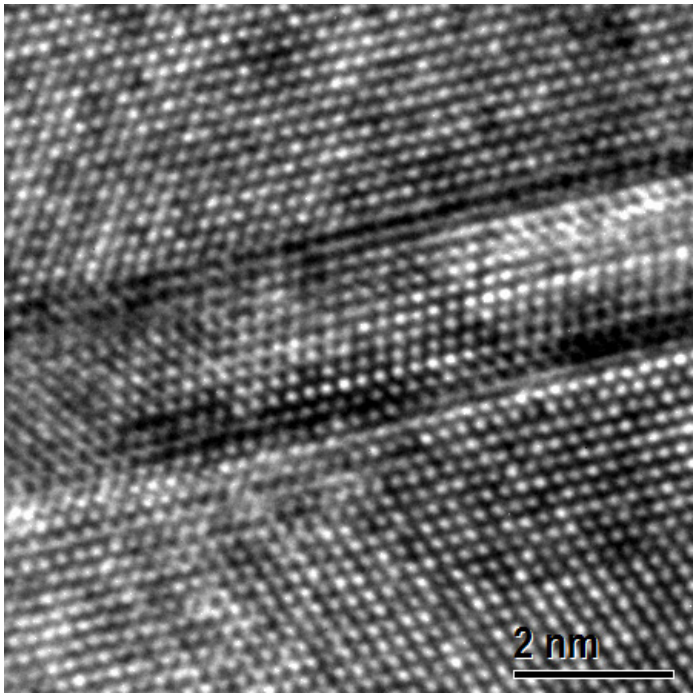

Figure 7-8 - The image displays atomic resolution of a mechanical twin, ~2 nm wide in an Fe-16Mn-14Cr-0.3C-0.3N sample deformed 20%. The atomic positions and the interface between the matrix and the twined crystal are directly observed.

7.4 High Strain-Rate Microstructural Characterization

High strain-rate testing is important for TRIP/TWIP steels given their potential use in automobile structures. There have been numerous studies on the mechanical properties of these steels under high strain rates [2] [3] [164] [165]. At high strain rates the testing becomes significantly more complex, and above 10 s^{-1} multiple waves are reflected within the load cell and must be considered in load measurements. Strain measurements are often made with non-contact optical extensometers or lasers [166]. The International Iron and Steel Institute (ISIJ) released their official recommendations for dynamic testing ~7 years ago [166]. A fundamental difference between quasi-static strain-rate and high strain-rate testing is the introduction of inertial effects and quasi-adiabatic heating [165]. The ISIJ states that the temperature of the tensile specimen can be raised by as much as 60°C when strained at a rate of 1000 s^{-1} [166]. Other reports cite an increase of greater than 100°C during high strain-rate testing [20] [165].

The influence that these combined inertial and thermal effects have on the microstructural evolution has not been well studied. This is due in large part to the difficulty in interrupting a high strain-rate test prior to specimen failure (test duration on the order of milliseconds). Christian and Mahajan have stated that an increase in strain-rate generally leads to an increase in twinning activity [58]. It was also noted that some FCC materials that do not twin under quasi-static deformation conditions, such as aluminum alloys, exhibit twinning under shock loading. A first-of-its-kind study by Choi et al. [167] compared the volume fraction of retained austenite in two different TRIP steels as a function of strain at rates up to 600 s^{-1}. In this study, retained austenite transformed slightly quicker (as a function of strain) at higher strain rates. In another study, microstructural evaluation of an Fe-18Mn-1.22Al-0.56C alloy showed adiabatic shear

banding and twinning after ballistic testing at ~10^5 s^{-1} [168]. Given the sensitivity of the SFE to temperature and the adiabatic heating of the sample during tensile testing, an impact on the microstructure is expected. Furthermore, the deformation mechanisms in certain alloys observed at quasi-static strain rates may be suppressed at high strain rates. For example, the 22%Mn alloy displays TRIP behavior at RT but twinning may be activated at higher strain rates given the increase in specimen temperature.

Future work on high-strain rate testing should be performed using an alloy, such as the Fe-25Mn-3Al-3Si alloy studied in the present work, which has been extensively characterized and exhibits both ε-martensite formation and mechanical twinning at RT. Thus, any shift in the deformation mechanisms (e.g., from TRIP to TWIP behavior) will be readily apparent in the microstructure of specimens deformed at high strain-rates. The strain rates employed should approximate those experienced in automobile crashes (i.e., 10-1000 s^{-1}). The use of non-uniform tensile specimen geometries (i.e., tapered shapes or specimens with multiple different cross sectional areas) should be employed as this could result in local areas of the specimen with different total strains after failure, eliminating the need for interrupting the test. Non-contact optical methods of strain and temperature measurement would be required.

CHAPTER 8

General Conclusions

The work reported here advances several key areas of TRIP/TWIP steel research, including; 1) the determination of the optimal thermo-mechanical processing routes of specimens and best TEM methods for SFE measurement, 2) the first measurements of the single-crystal elastic constants for several TRIP/TWIP steels and determination of the influence of antiferromagnetic ordering on the elastic anisotropy, 3) determination of the SFE and FCC/HCP interfacial energy using a combined experimental and theoretical method, and 4) development of semi-quantitative relationships among temperature, SFE, deformation mechanisms and mechanical properties.

The optimal method of SFE measurement for the Fe-22/25/28Mn-3Al-3Si wt.% alloys is the direct measurement of partial-dislocation separations using WBDF imaging techniques. Extended nodes that formed in this alloy appeared asymmetric with varying sizes and were rarely isolated, precluding any meaningful measurements. The thermo-mechanical treatments utilized to prepare the tensile samples discussed in Chapter 3, coupled with tensile deformation to only the YP, resulted in the best microstructure (optimal grain size with minimal internal strain) for measuring partial-dislocation separations.

A method to calculate single-crystal elastic constants from orientation-specific indentation moduli was proposed for use on polycrystalline cubic materials. The model yields single-crystal elastic constants to within a standard deviation of ~4% of established literature values. The method yields values of C_{11}, C_{12} and C_{44} of 175±7/83±3/97±4 and 174±7/85±3/99±4 GPa for Fe-

(22/25)Mn-3Al-3Si wt.% TRIP/TWIP alloys, respectively. For a Fe-18Mn-1.5Al-0.6C wt.% steel, with indentation data in the literature, the method yields elastic constants of 169±6/82±3/96±4 GPa, showing good agreement with the Fe-Mn-Al-Si steels. These values represent some of the first experimental single-crystal elastic constants for TRIP/TWIP steels and can be utilized to account for anisotropic elasticity, as in references [82] [83] [85], to increase the accuracy of SFE measurements. Fe-(22/25)-3Al-3Si and Fe-18Mn-1.5Al-0.6C steels are magnetically disordered at room temperature and do not experience significant suppression of the shear term $(C_{11}-C_{12})/2$ caused by antiferromagnetic ordering. As a result, the anisotropy ratios of the TRIP/TWIP steels, 2.11-2.22, are significantly lower than that of ~3.5-3.9 for binary Fe-30-40Mn at.% alloys with similar composition but in the antiferromagnetic state. For TWIP steels in the antiferromagnetic regime at room temperature, such as the Fe-22Mn-0.6C grade, the elastic anisotropy is expected to increase.

The effect of Mn content on the SFE was investigated by measuring dissociation widths of partial-dislocation pairs in three Fe-22/25/28Mn-3Al-3Si wt.% alloys, yielding SFE values of 15 ±3, 21 ±3 and 39 ±5 mJ m^{-2}, respectively. The strain energy associated with the contraction in molar volume during the austenite to ε_{hcp}-martensite transformations was determined to be ~1-4 mJ m^{-2}, resulting in ideal SFE values of 14±3, 19±3 and 35±5 mJ m^{-2}. A new thermodynamic model for the Fe-Mn-Al-Si-C system was proposed which determines the chemical and magnetic components of the difference in Gibbs free energy of the FCC and HCP phases. The new model provides improved agreement with experimental observations of the influence of Si on the SFE in Fe-Mn based alloys. The ideal SFE values were used in conjunction with the thermodynamic phase data to determine the FCC/HCP interfacial energies of the three Fe-22/25/28Mn-3Al-3Si

alloys. Additional calculations of the interfacial energy were made for Fe-Mn and Fe-Mn-C-Al/Si alloys for which experimental SFE data are available in the literature. The calculated FCC/HCP interfacial energies ranged from 8.6 to 11.8 mJ m^{-2} for the TRIP/TWIP alloys. The range of 8.6 to 11.8 mJ m^{-2} is narrower than the 5 to 27 mJ m^{-2} range that has been employed in past SFE calculations [3] [34] [35] and should enhance the accuracy of future thermodynamic SFE models. The interfacial energy of the binary Fe-Mn alloys ranged from 15.7 to 32.5 mJ m^{-2}. The present work shows a strong correlation between the value of the interfacial energy of Fe-Mn-(Al,Si,C) steels and the difference in free energy of the FCC and HCP phases. An empirical relationship to describe the interfacial energy was proposed to improve the accuracy of SFE calculations. The combined thermodynamic model and empirical relationship exhibit good agreement with the present SFE measurements, and those in the literature, making it a useful tool for the design of high-Mn TRIP/TWIP steels.

The influence of SFE and $\Delta G_{total}^{fcc \rightarrow hcp}$ on the microstructural and strain-hardening evolution of three Fe-22/25/28Mn-3Al-3Si alloys was investigated. Secondary deformation mechanisms such as $\alpha_{bcc}/\varepsilon_{hcp}$-martensite formation and/or mechanical twinning are activated at specific SFE and/or $\Delta G_{total}^{fcc \rightarrow hcp}$ values and strongly contribute to the excellent mechanical properties of these materials. A SFE of 15 mJ m^{-2} (Fe-22Mn-3Al-3Si at RT) resulted in a highly planar microstructure, suppression of dislocation cross-slip, and $\alpha_{bcc}/\varepsilon_{hcp}$-martensite transformation as the dominant secondary deformation mechanism. The onset of grain refinement due to ε_{hcp}-martensite in multiple systems enhanced the strain-hardening at low strains in this alloy. For a SFE of 21 mJ m^{-2} (Fe-25Mn-3Al-3Si at RT) the dislocation structure exhibits both planar and wavy characteristics at low strains. Mechanical twinning is the dominant secondary deformation

mechanism in this alloy and influences the strain-hardening after 0.1 true strain. The formation of ε_{hcp}-martensite plays a smaller role in the deformation and α_{bcc}-martensite is completely suppressed. For a SFE of 39 mJ m^{-2} (Fe-28Mn-3Al-3Si at RT) dislocations are largely constricted at low strains (0 to 0.1 true strain), ε_{hcp}-martensite is absent, and the microstructure exhibits wavy slip and the formation of dislocation cell structures. Mechanical twinning begins to influence the strain-hardening behavior at ~0.1 true strain

The TUTSs and maximum uniform elongations of the Fe-22/25/28Mn-3Al-3Si alloys at RT are 1172±19/1136±9/1104±14 MPa and 72±2/77±2/75±1%, respectively. As the SFE is increased from 15 to 21 mJ m^{-2} (corresponding to the transition from TRIP to TWIP dominated behavior) a small decrease in strength and increase in ductility is observed. As the SFE is increased from 21 to 39 mJ m^{-2} the TUTSs and maximum uniform elongation remain nearly constant, decreasing by only 3%. Therefore, changes in the SFE from 21 to 39 mJ m^{-2} alter the deformation mechanisms but have little effect on the mechanical properties.

Increasing the deformation temperature from 25 to 200°C results in suppression of the secondary deformation mechanisms and a severe loss in strength and ductility in each tested alloy (toughness decreases from ~ 496 at RT to ~212 mJ m^{-3} at 200°C). The deformation mechanisms exhibit a strong correlation with the relative FCC/HCP phase stability, $\Delta G_{total}^{fcc \rightarrow hcp}$ (J mol^{-1}), as it is changed by increasing the temperature and/or additions of Mn. The formation of ε-martensite occurs up to values of ~$\Delta G_{total}^{fcc \rightarrow hcp}$=175 J mol^{-1}, while mechanical twinning is active in the range

of ~-90 to 460 J mol^{-1}. The value of $\Delta G_{total}^{fcc \rightarrow hcp}$ may be used as a simple method to predict the deformation mechanisms of Fe-Mn-(Al-Si) steels.

APPENDIX A

ULTRASONIC PULSE VELOCITY MEASURMENTS

The shear moduli and Poisson's ratios of four steels (Fe-22/25/28Mn-3Al-3Si and Fe-14Cr-16Mn-0.3N-0.3C) were determined from ultrasonic pulse (transverse/shear and longitudinal) velocities. A Tektronix TDS 2001C oscilloscope, Olympus 5072PR pulser/receiver, 20 MHz delay line normal incident longitudinal transducer (CTS Valpey Corporation, part number DP 202 20/.25) and a 10 MHz delay line normal incident shear transducer (CTS Valpey Corporation, part number SD 102-SL) were used to make ultrasonic pulse velocity measurements. The transducers were used in a pitch/catch method on flat sheets of material ranging from 1 to 1.5 mm thickness which were polished in accordance with the methods described in Chapter 2. Soundsafe ultrasound couplant and molasses were used to couple specimens to the longitudinal and shear wave transducers, respectively. The pulse is introduced by the transducer normal to the specimen surface, travels through the material, is reflected by the opposite surface, and is received by the transducer. Multiple reflections (echoes) occur in the specimen before the pulse is dissipated. The longitudinal (v_l) and transverse (v_t) velocities are obtained from the path length (twice the specimen thickness) divided by the transit time (obtained from the time between the crests of the leading wave of successive echoes [121]). The initial pulse and eight trailing echoes are shown in Figure A-1a for the Fe-28Mn-3Al-3Si alloy at RT. Figure A-1b shows only the second and third echoes and indicates the transit time. An error associated with the transducer and transducer/specimen coupling is included in measurements of the transit time. Following Neighbours [169], the transit time error is determined by plotting the transit time vs. specimen

thickness of the same material for several different thicknesses (type 304 steel was used to determine the transit time error). The transit time vs. specimen thickness for the type 304 steel is presented in Figure A-2 and indicates that the transit time error is ~0.0024 and 0.0044 μs for longitudinal and transverse waves, respectively, for the current experimental setup.

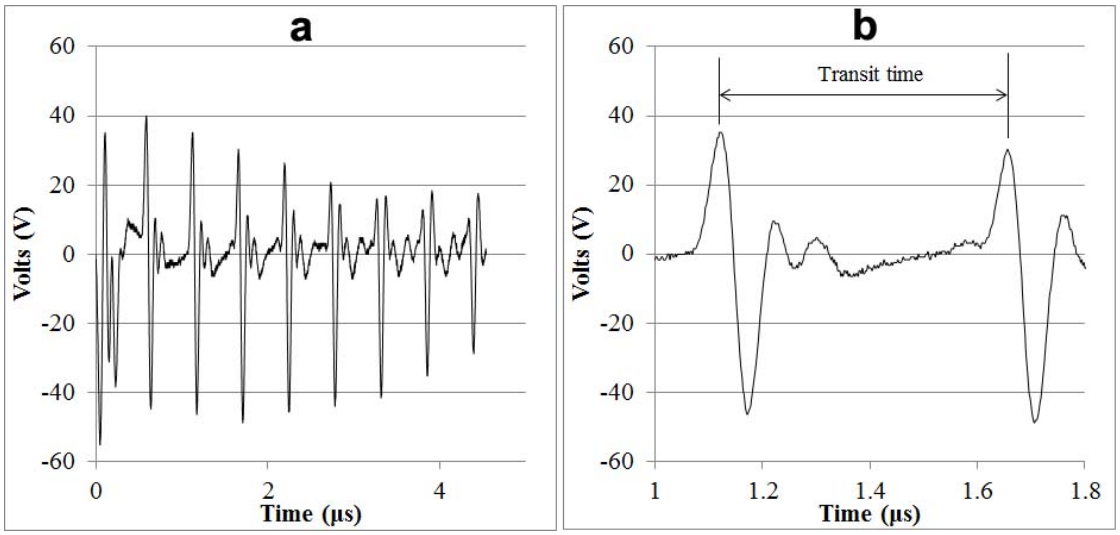

Figure A-1 – (a) Volts vs. time (μs) for an ultrasonic pulse and 8 echoes in and Fe-28Mn-3Al-3Si alloy at RT. (b) amplitude vs time showing the transit time between the second and third echoes (as measured from the apex of the leading edge of each echo).

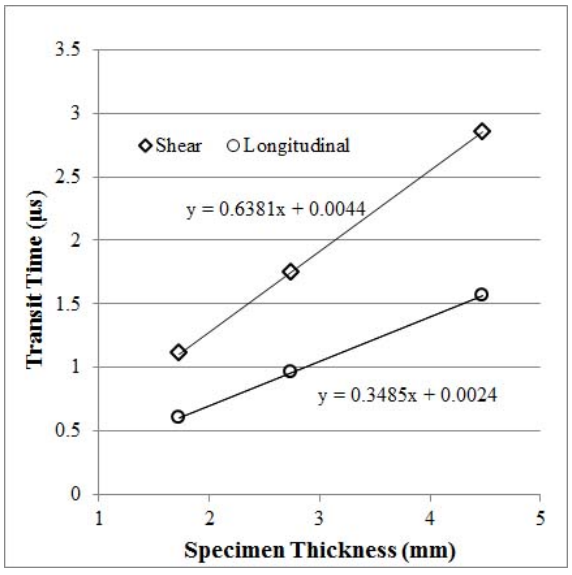

Figure A-2 – Transit time for longitudinal and transverse waves vs. specimen thickness for type 304 steel.

The shear moduli (G) and Poisson's (ν) ratios are determined from the transverse and longitudinal sound velocities by Equations A-1 and A-2, respectively [121]:

$$G = \rho v_t^2 \quad \text{(A-1)}$$

$$\nu = \frac{1}{2}\frac{(v_l^2 - 2v_t^2)}{(v_l^2 - v_t^2)} \quad \text{(A-2)}$$

where ρ is the density of the material. The longitudinal and transverse sound velocities, density, Young's modulus, shear modulus and Poisson's ratio at room temperature are presented in Table A-1. Additional transverse velocity measurements were obtained from ~ -15 to 60°C for the Fe-25/28Mn-3Al-3Si alloys and the shear moduli calculated from these measurements are shown in Figure A-3. The reduction in shear modulus below room temperature is attributed to antiferromagnetic ordering [4] [48] [132].

Table A-1 – Longitudinal and transverse sound velocities, density, Young's modulus, shear modulus and Poisson's ratio for the Fe-22/25/28Mn-3Al-3Si alloys and a Fe-14Cr-16Mn-0.3N-0.3C steel.

Material	v_l (μm μs^{-1})	v_t (μm μs^{-1})	ρ (g cm^{-3})	E (GPa)	G (GPa)	ν
Fe-22Mn-3Al-3Si	5561±94	3054±40	7.39	184±2	69±2	0.26±0.01
Fe-25Mn-3Al-3Si	5478±43	3070±22	7.38	177±2	69±2	0.27±0.01
Fe-28Mn-3Al-3Si	5516±22	3067±22	7.35	179±2	69±2	0.27±0.01
Fe-14Cr-16Mn-0.3N-0.3C	5756±50	3180±91	7.83	203±2	79±1	0.28±0.01

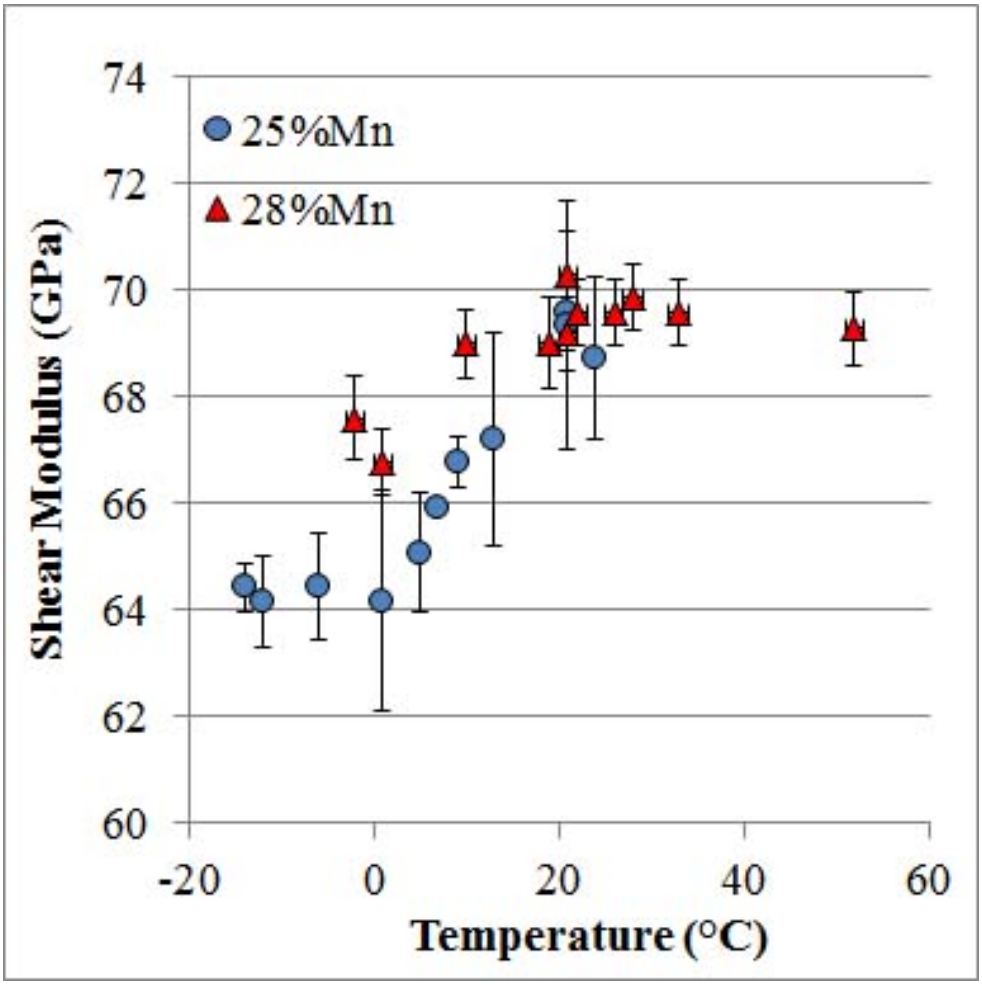

Figure A-3 – Shear modulus vs. temperature for 25 and 28%Mn alloys.

REFERENCES

[1] O. Grässel, G. Frommeyer, C. Derder and H. Hofmann, "Phase Transformations and Mechanical Properties of Fe-Mn-Al-Si TRIP Steels," *J. Physique IV,* vol. 7, pp. C5-383-386, 1997.

[2] O. Grässel, L. Krüger, G. Frommeyer and L. W. Meyer, "High Strength Fe-Mn-(Al, Si) TRIP/TWIP Steels Development - Properties - Application," *Int. J. Plasticity,* vol. 16, p. 1391, 2000.

[3] S. Curtze and V. T. Kuokkala, "Dependence of tensile deformation behavior of TWIP steels on stacking fault energy, temperature and strain rate," *Acta Mater.,* vol. 58, no. 15, 2010.

[4] O. Bouaziz, S. Allain, C. P. Scott, P. Cugy and D. Barbier, "High manganese austenitic twinning induced plasticity steels: A review of the microstructure properties relationships," *Curr. Opin. Solid State Mater. Sci.,* vol. 15, p. 141, 2011.

[5] S. Vercammen, Processing and Tensile Behaviour of TWIP Steels Microstructural and Textural Analysis, Leuven: Katholieke Universiteit Leuven, 2004.

[6] B. C. De Cooman, O. Kwon and K.-G. Chin, "State of the knowledge on TWIP steel," *J. Mater. Sci. Technol,* vol. 28, no. 5, 2012.

[7] A. Saeed-Akbari, L. Mosecker, A. Schwedt and W. Bleck, "Characterization and Prediction of Flow Behavior in High-Manganese Twinning Induced Plasticity Steels: Part 1. Mechanism Maps and Work-Hardening Behavior," *Metall. Mater. Trans. A,* vol. 43, p. 1688, 2012.

[8] A. Saeed-Akbari, A. Schwedt and W. Bleck, "Low Stacking Fault Energy Steels in the Context of Manganese-Rich Iron-Based Alloys," *Scripta. Mat.,* vol. 66, pp. 1024-1029, 2012.

[9] "National Highway Traffic Safety Administration," 2013. [Online]. Available: http://www.nhtsa.gov/.

[10] "Insurance Institute for Highway Safety," 2013. [Online]. Available: http://www.iihs.org/.

[11] B. C. De Cooman, K.-G. Chin and J. Kim, "High Mn TWIP Steels for Automotive Applications," in *New Trends and Developments in Automotive System Engineering*, M. Chiaberge, Ed., 2011, pp. 101-128.

[12] "Steel Works," 2013. [Online]. Available: http://www.steel.org/.

[13] S.-K. Kim, G. Kim and K.-G. Chin, "Development of High Manganese TWIP Steel with 980MPa Tensile Strength," in *International Conference on New Developments in Advanced High-Strength*

Sheet Steels, Orlando, 2008.

[14] I. Gutierrez-Urrutia and D. Raabe, "Dislocation and twin substructure evolution during strain hardening of an Fe-22 wt.% Mn-0.6 wt.% C TWIP steel observed by electron channeling contrast imaging," *Acta Mater.*, vol. 59, p. 6449, 2011.

[15] J. Kim, S.-J. Lee and B. C. De Cooman, "Effect of Al on the stacking fault energy of Fe-18Mn-0.6C twinning-induced plasticity," *Scripta Mat.*, vol. 65, pp. 363-366, 2011.

[16] K. Jeong, J.-E. Jin, Y.-S. Jung, S. Kang and Y.-K. Lee, "The effects of Si on the mechanical twinning and strain hardening of Fe-18Mn-0.6C twinning-induced plasticity steel," *Acta Mater.*, vol. 61, pp. 3399-3410, 2013.

[17] L. Mosecker and A. Saeed-Akbari, "Nitrogen in chromium-manganese stainless steels: a review on the evaluation of stacking fault energy by computational thermodynamics," *Sci. Technol. Adv. Mater.*, vol. 14, pp. 1-14, 2013.

[18] I. Gutierrez-Urrutia and D. Rabbe, "Multistage strain hardening through dislocation substructure and twinning in a high strength and ductile weight-reduced Fe-Mn-Al-C steel," *Acta Mater*, vol. 60, pp. 5791-5802, 2012.

[19] R. Abbaschian, L. Abbaschian and R. E. Reed-Hill, Physical Metallurgy Principles, 4 ed., H. Gowans, Ed., Cengage Learning, 2009.

[20] D. R. Steinmetz, T. Japel, B. Wietbrock, P. Eisenlohr, I. Gutierrez-Urrutia, A. Saeed-Akbari, T. Hickel, F. Roters and D. Raabe, "Revealing the strain-hardening behavior of twinning-induced plasticity steels: theory, simulations, experiments," *Acta Mater.*, vol. 61, p. 494, 2013.

[21] I. Gutierrez-Urrutia, S. Zaefferer and D. Raabe, "The Effect of Grain Size and Grain Orientation on Defformation Twinning in a Fe-22 wt.%Mn-0.6wt.%C TWIP Steel," *Mater. Sci. Eng. A*, vol. 527, pp. 3552-3560, 2010.

[22] L. Remy, "Kinetics of F.C.C. Deformation Twinning and its Relationship to Stress-Strain Behaviour," *Acta Metall*, vol. 26, pp. 443-451, 1978.

[23] S. Allain, O. Bouaziz and J. P. Chateau, "A physical model of the twinning-induced plasticity effect in a high manganese austenitic steel," *Materials Science and Engineering*, Vols. 387-389, pp. 143-147, 2004.

[24] O. Bouaziz, S. Allain and C. Scott, "Effect of grain and twin boundaries on the hardening mechanisms of twinning-iduced plasticity steels," *Scripta Mat.*, vol. 58, pp. 484-487, 2008.

[25] D. Barbier, V. Favier and B. Bolle, "Modeling the deformation textures and microstructural evolutions of a Fe-Mn-C TWIP steel during tensile and shear testing," *Mater Sci Eng A*, vol. 540,

pp. 212-225, 2012.

[26] S. Dancette, L. Delannay, K. Renard, M. A. Melchior and P. J. Jacques, "Crystal plasticity modeling of texture development and hardening in TWIP steels," *Acta Mater,* vol. 60, pp. 2135-2145, 2012.

[27] J. Kim, Y. Estrin, H. Beladi, I. Timokhina, K.-G. Chin, S.-K. Kim and B. C. De Cooman, "Constitutive Modeling of the Tensile Behavior of Al-TWIP Steel," *Metall Mater Trans,* vol. 43, pp. 479-490, 2012.

[28] Y. G. Kim, Y. S. Park and J. K. Han, "Low Temperature Mechanical Behavior of Microalloyed and Controlled-Rolled Fe-Mn-Al-C-X Alloys," *Metall. Trans. A.,* vol. 16, pp. 1689-1693, 1985.

[29] L. Remy and A. Pineau, "Twinnign and Strain-induced F.C.C to H.C.P. Transformation in the Fe-Mn-Cr-C System," *Mater Sci Eng,* vol. 28, pp. 99-107, 1977.

[30] Y. G. Kim, J. K. Han and E. W. Lee, "Effect of Aluminum Content on Low Temperature Tensile Properties in Cryogenic Fe/Mn/Al/Nb/C Steels," *Metall. Trans. A,* vol. 17, pp. 2097-2098, 1986.

[31] G. Frommeyer, U. Brux and P. Neumann, "Supra-Ductile and High-Strength Manganese-TRIP/TWIP Steels for High Energy Absorption Purposes," *ISIJ Int.,* vol. 43, no. 3, pp. 438-446, 2003.

[32] G. Frommeyer and U. Brux, "Microstructure and Mechanical Properties of High-Strength Fe-Mn-Al-C Light-Weight TRIPLEX Steels," *Steel Research Int.,* vol. 77, no. 9-10, pp. 627-633, 2006.

[33] S. R. Kalidindi, A. A. Salem and R. D. Doherty, "Role of Deformation Twinning on Strain Hardening in Cubic and Hexagonal Polycrystalline Metals," *Adv. Eng. Mater.,* vol. 5, no. 4, pp. 229-232, 2003.

[34] S. Allain, J. P. Chateau, O. Bouaziz, S. Migot and N. Guelton, "Correlations between the calculated stacking fault energy and the plasticity mechanisms in Fe-Mn-C alloys," *Materials Science and Engineering A,* Vols. 387-389, pp. 158-162, 2004.

[35] A. Saeed-Akbari, J. Imlau, U. Prahl and W. Bleck, "Derivation and Variation in Composition-Dependent Stacking Fault Energy Maps Based on Subregular Solution Model in High-Manganese Steels," *Metall. Mater. Trans. A,* vol. 40a, p. 3076, 2009.

[36] H. Idrissi, K. Renard, D. Schryvers and P. J. Jacques, "On the Relationship Between the Twin Internal Structure and the Work-hardening Rate of TWIP Steels," *Scripta Mat.,* vol. 63, pp. 961-964, 2010.

[37] J. Gil Sevillano, "An Alternative Model for the Strain Hardening of FCC Alloys that Twin, Validated for Twinning-Induced Plasticity Steel," *Scripta Mat.,* vol. 60, pp. 336-339, 2009.

[38] P. H. Adler, G. B. Olson and W. S. Owen, "Strain Hardening of Hadfield Manganese Steel," *Metall. Mater. Trans. A* , vol. 17A, pp. 1725-1737, 1986.

[39] M. K. Miller, P. A. Beaven, S. S. Brenner and G. D. W. Smith, "An Atom Probe Study of the Aging of Iron-Nickel-Carbon Martensite," *Metall. Trans. A*, vol. 14A, pp. 1021-1024, 1983.

[40] M. K. Miller, P. A. Beaven, R. J. Lewis and G. Smith, "Atom Probe Microanalytical Studies of Some Commercially Important Steels," *Surface Science*, vol. 70, pp. 470-484, 1978.

[41] R. K. W. Marceau, K. L. Moore, I. Gutierrez-Urrutia, M. Herbig, S. Lozano-Perez and D. Raabe, "Multi-scale Correlative Microscopy Investigation of Both Structure and Chemistry of Deformation Twin Bundles in Fe-Mn-C Steel," *Microscopy and Microanalysis*, vol. 19, no. 6, pp. 1581-1585, 2013.

[42] D. Barbier, N. Gey, S. Allain, N. Bozzolo and M. Humbert, "Analysis of the tensile behavior of a TWIP steel based on the texture and microstructure evolutions," *Mater. Sci. Eng. A*, vol. 500, pp. 196-206, 2009.

[43] S.-J. Lee, J. Kim, S. N. Kane and B. C. De Cooman, "On the Origin of Dynamic Strain Aging in Twinning-Induced Plasticity Steels," *Acta Mat*, vol. 59, pp. 6809-6819, 2011.

[44] T. A. Lebedkina, M. A. Lebyodkin, J.-P. Chateau, A. Jacques and S. Allain, "On the Mechanism of Unstable Plastic Flow in an Austenitic FeMnC TWIP Steel," *Mater. Sci. Eng. A*, vol. 519, pp. 147-154, 2009.

[45] D. Zavattieri, V. Savic, L. G. Hector, J. R. Fekete, W. Tong and Y. Xuan, "Spatio-temporal Characteristics of the Potevin-Le Châtelier Effect in Austenitic Steel with Twinning Induced Plasticity," *Int. J. Plast.*, vol. 25, pp. 2298-2330, 2009.

[46] I.-C. Jung and B. C. De Cooman, "Temperature Dependence of the Flow Stress of Fe-18Mn-0.6C-xAl Twinning-Induced Plasticity Steel," *Acta Man*, vol. 61, pp. 6724-6735, 2013.

[47] H. Beladi, I. B. Timokhina, Y. Estrin, J. Kim, B. C. De Cooman and S. K. Kim, "Orientation dependence of twinning and strain hardening behaviour of a high manganese twinning induced plasticity steel with polycrystalline structure," *Acta Mater.*, vol. 59, pp. 7787-7799, 2011.

[48] I. Jung, S.-J. Lee and B. C. De Cooman, "Influence of Al on Internal Friction Spectrum of Fe-18Mn-0.6C Twinning-Induced Plasticity Steel," *Scripta Mater.*, vol. 66, pp. 729-732, 2012.

[49] J. P. Hirth, Theory of Dislocations, 2nd ed., John Wiley and Sons, 1982.

[50] S. Kibey, J. B. Liu, D. D. Johnson and H. Sehitoglu, "Predicting Twinning Stress in FCC Metals: Linking Twin-Energy Pathways to Twin Nucleation," *Acta Mat.*, vol. 55, pp. 6843-6851, 2007.

[51] G. B. Olson and M. Cohen, "A General Mechanism of Martensitic Nucleation: Part 1. General

Concepts and the FCC to HCP Transformation," *Metall. Trans. A*, vol. 78, p. 1897, 1976.

[52] J. W. Brooks, M. H. Loretto and R. E. Smallman, "In situ Observations of the Formation of Martensite in Stainless Steel," *Acta Met.*, vol. 27, p. 1829, 1979.

[53] J. W. Brooks, M. H. Lorreto and R. E. Smallman, "Direct Observations of Martensite Nuclei in Stainless Steel," *Acta Met.*, vol. 27, p. 1839, 1979.

[54] C. C. Bampton, I. P. Jones and M. H. Loretto, "Stacking Fault Energy Measurements in Some Austenitic Stainless Steels," *Acta Met.*, vol. 26, p. 39, 1978.

[55] P. Marinelli, A. Baruj, A. Fernandez Guillermet and M. Sade, "Lattice Parameters of Metastable Structures in Quenched Fe-Mn Alloys. Part I: Experimental Techniques, bcc and fcc phases," *Z. Metallkd.*, vol. 91, no. 11, pp. 957-962, 2001.

[56] P. Marinelli, A. Baruj, A. Fernandez Guillermet and M. Sade, "Lattice Parameters of Metastable Structures in Quenched Fe-Mn Alloys. Part II: hcp Phase," *Z. Metallkd.*, vol. 92, no. 5, p. 489, 2001.

[57] P. Mullner and P. J. Ferreira, "On the energy of terminated stacking faults," *Philos. Mag. Lett.*, vol. 73, no. 6, pp. 289-297, 1996.

[58] J. W. Christian and S. Mahajan, "Deformation Twinning," *Prog. Mater. Sci.*, vol. 39, pp. 1-157, 1995.

[59] S. Mahajan and G. Y. Chin, "Formation of Deformation Twins in F.C.C. Crystals," *Acta Metall.*, vol. 21, no. 10, pp. 1353-1363, 1973.

[60] J. B. Cohen and J. Weertman, "A Dislocation Model for Twinning in F.C.C. Metals," *Acta Metall.*, vol. 11, no. 8, pp. 996-998, 1963.

[61] J. B. Cohen and J. Weertman, "Reply to Comments on “A Dislocation Model for Twinning in F.C.C. Metals," *Acta Metall.*, vol. 11, no. 12, pp. 1368-1369, 1963.

[62] S. Miura, J. I. Takamura and N. Narita, "Orientation Dependance of Flow Stress for Twinning in Silver Crystals," *Trans. Jpn. Inst. Metals*, vol. S, no. 9, p. 555, 1968.

[63] H. Fujita and T. Mori, "A Formation Mechanism of Mechanical Twins in F.C.C. Metals," *Scripta Metall.*, vol. 9, no. 6, pp. 631-636, 1975.

[64] H. Idrissi, K. Renard, L. Ryelandt, D. Schryvers and P. J. Jacques, "On the Mechanism of Twin Formation in Fe-Mn-C TWIP Steels," *Acta Mater.*, vol. 58, pp. 2464-2476, 2010.

[65] V. T. Witusiewicz, F. Sommer and E. J. Mittemeijer, "Reevaulutation of the Fe-Mn Phase Diagram," *JPEDAV*, vol. 25, pp. 346-354, 2004.

[66] A. J. Bradley and J. Thewlis, "The Crystal Structure of Alpha Manganese," *Proc. R. Soc. Lond. A,* vol. 115, pp. 456-471, 1927.

[67] Y. Tomota, M. Strum and J. W. Morris, "Microstructural Dependance of Fe-High Mn Tensile Behavior," *Met. Trans A,* vol. 17, pp. 537-547, 1995.

[68] R. P. Reed and R. E. Schramm, "Relationships between stacking-fault energy and x-ray measurments of stacking-fault probability and microstrain," *J. Appl. Phys.,* vol. 45, no. 11, pp. 4706-4711, 1974.

[69] R. E. Schramm and R. P. Reed, "Stacking Fault Energies of FCC Fe-Ni Alloys by X-Ray Diffraction Line Profile Analysis," *Met. Trans. A.,* vol. 7, pp. 359-363, 1976.

[70] R. E. Schramm and R. P. Reed, "Stacking Fault Energies of Seven Commercial Austenitic Stainless Steels," *Met. Trans. A,* vol. 6, pp. 1345-1351, 1974.

[71] M. J. Whelan, "Dislocations in Face-Centered Cubic Metals with Particular Refference to Stainless Steel," *Proc. Roy. Soc.,* vol. 249, p. 114, 1958.

[72] L. M. Brown, "The Self-stress of Dislocations and the Shape of Extended Nodes," *Philos. Mag.,* vol. 10, p. 441, 1964..

[73] L. M. Brown and A. R. Tholen, "Shape of Three-Fold Extende Nodes," *Disc. Faraday Soc.,* vol. 38, p. 35, 1964.

[74] R. Siems, "Shape of Extended Nodes," *Disc. Faraday Soc.,* vol. 38, p. 42, 1964.

[75] T. Jøssang, M. J. Stowell, J. P. Hirth and J. Lothe, "On the Determination of Stacking Fault Energies From Extended Dislocation Node Measurements," *Acta Met.,* vol. 13, no. 3, p. 279, 1965.

[76] A. W. Ruff, "Measurements of Stacking Fault Energy from Dislocation Interactions," *Met. Trans.,* vol. 1, p. 2391, 1970.

[77] R. M. Latinison and A. W. Ruff, "The temperature dependance of stacking fault energy in Fe-Cr-Ni alloys," *Metall. Trans.,* vol. 2, pp. 505-509, 1971.

[78] P. C. J. Gallagher, "Influence of alloying, temperature, and related effects on the stacking fault energy," *Metall. Mater. Trans. B,* vol. 1, p. 2429, 1970.

[79] P. Y. Volosevich, V. N. Gridnev and Y. N. Petrov, "Influence of Manganese and the Stacking Fault Energy of Iron-Manganese Alloys," *Phys. Met. Metallogr.,* vol. 42, pp. 126-130, 1976.

[80] P. Y. Volosevich, V. N. Gridnev and Y. N. Petrov, "Influence of Carbon on the Stacking Fault Energy of Austenite in Manganese Steels," *Phys. Met. Metallogr.,* vol. 40, pp. 90-100, 1975.

[81] L. Remy, "Temperature Variation of the Intrinsic Stacking Fault Energy of a High Manganese Austenitic Steel," *Acta Met.*, vol. 25, p. 173, 1977.

[82] J. D. Eshelby, W. T. Read and W. Shockley, "Anisotropic Elasticity with Applications to Dislocation Theory," *Acta Met.*, vol. 1, no. 3, pp. 251-259, 1953.

[83] A. E. Foreman, "Dislocation Energies in Anisotropic Crystals," *Acta Met.*, vol. 3, pp. 322-330, 1955.

[84] L. J. Teutonico, "The Dissociation of Dislocations in the Face-Centered Cubic Structure," *Acta Metall.*, vol. 11, no. 12, pp. 1283-1289, 1963.

[85] E. Aerts, P. Delavignette, R. Siems and S. Amelinckx, "Stacking Fault Energy in Silicon," *J. Appl. Phys.*, vol. 33, no. 10, p. 3078, 1962.

[86] D. J. H. Cockayne and V. Vitek, "Effect of Core Structure on the Determination of the Stacking-Fault Energy in Close-Packed Metals," *Phys. Stat. Sol. (b)*, vol. 65, pp. 751-764, 1974.

[87] D. J. H. Cockayne, I. L. F. Ray and M. J. Whelan, "Investigations of Dislocation Strain Fields Using Weak Beams," *Philos. Mag.*, vol. 20, no. 168, p. 1265, 1969.

[88] D. B. Williams and C. B. Carter, Transmission Electon Microscopy, a Text Book for Materials Science, 2nd ed., Springer, 2009.

[89] J. W. Edington, Practical Electron Microscopy in Materials Scinece, Eindhoven: N. V. Philips Gloeilampenfabrieken, 1976.

[90] D. H. Cockayne, M. L. Jenkins and I. L. F. Ray, "The Measurment of Stacking-fault Energies of Pure Face-centered Cubic Metals," *Philos. Mag.*, vol. 24, no. 192, pp. 1383-1392, 1971.

[91] W. M. Stobbs and C. H. Sworn, "The weak beam technique as applied to the determination of the stacking-fault energy of copper," *Philos. Mag.*, vol. 24, pp. 1365-1381, 1971.

[92] M. L. Jenkins, "Measurement of the stacking-fault energy of gold using the weak-beam technique of electron microscopy," *Philos. Mag.*, vol. 26, pp. 747-751, 1972.

[93] I. L. F. Ray and D. J. H. Cockayne, "The dissociation of dislocations in silicon," *Proc. Roy. Soc. Lond. A.*, vol. 325, pp. 543-554, 1971.

[94] C. B. Carter and S. M. Holmes, "The Stacking-Fault Energy of Nickel," *Philos. Mag.*, vol. 35, no. 5, p. 1161, 1977.

[95] D. J. H. Cockayne, "A Theoretical Analysis of the Weak-beam Method of Electron Microscopy," *Z. Naturforsch*, vol. 27a, p. 452, 1972.

[96] A. Dumay, J. P. Chateau, S. Allain, S. Migot and O. Bouaziz, "Influence of addition elements on the stacking fault energy and mechnaical properties of an austenetic Fe-Mn-C steel," *Materials Science and Engineering A*, Vols. 483-484, pp. 184-187, 2008.

[97] S. Curtze, V. -T. Kuokkala, A. Oikari, J. Talonen and H. Hanninen, "Thermodynamic Modeling of the Stacking-Fault Energy of Austenitic Steels," *Acta Mat.*, vol. 59, pp. 1068-1076, 2011.

[98] J. Nakano and P. J. Jacques, "Effects of the thermodynamic parameters of the hcp phase on the stacking fault energy calculations in the Fe–Mn and Fe–Mn–C systems," *CALPHAD*, vol. 34, pp. 167-175, 2010.

[99] M. Hillert and M. Jarl, "A Model for Alloying Effects in Ferromagnetic Metals," *CALPHAD*, vol. 2, no. 3, pp. 227-238, 1978.

[100] G. Inden, "The Role of Magnetism in the Calculation of Phase Diagrams," *Physica*, vol. 103B, pp. 81-100, 1981.

[101] A. Saeed-Akbari, J. Imlau, U. Prahl and W. Bleck, "Derivation and Variation in Composition-Dependent Stacking Fault Energy Maps Based on Subregular Solution Model in High-Manganese Steels," *Metall. Mater. Trans. A*, vol. 40a, pp. 3076-3090, 2009.

[102] J. D. Eshelby, "The Determination of the Elastic Field of an Ellipsoidal Inclusion, and Related Problems," *Proc. R. Soc. Lond. A*, vol. 241, pp. 376-396, 1957.

[103] H. M. Ledbetter, "Monocrystal-Polycrystal Elastic Constants of a Stainless Steel," *Phys. Stat. Sol. (a)*, vol. 85, no. 89, pp. 89-96, 1984.

[104] Y. Endoh, Y. Noda and M. Iizumi, "Lattice Dynamics and Invar Properties in F.C.C. FeMn Alloy," *J. Phys. Soc. Jpn*, vol. 50, no. 2, pp. 469-475, 1981.

[105] J. T. Lenkkeri, "Measurments of Elastic Moduli of Face-centered Cubic Alloys of Transition Metals," *J. Phys. F: Metal Phys.*, vol. 11, pp. 1991-1996, 1981.

[106] M. Cankurtaran, G. A. Saunders., P. Ray, Q. Wang, U. Kawald, J. Pelzl and H. Bach, "Relationship of the Elastic and Nonlinear Acoustic Properties of the Antiferromagnetic FCC Fe60Mn40 Single-crystal Alloy to Invar Behavior," *Phys. Rev. B*, vol. 47, no. 6, pp. 3161-3170, 1993.

[107] J. T. Lenkkeri and J. Levoska, "Effects of Magnetic and Structural Change on Elastic Moduli of Iron-Manganese Alloys," *Philos. Mag. A*, vol. 48, no. 5, pp. 749-758, 1983.

[108] S. Allain, Ph.D Thesis, Institut National Polytechnique de Lorraine, 2004.

[109] D. Music, T. Takahashi, L. Vitos, C. Asker and I. A. Abrikosov, "Elastic Properties of Fe-Mn Random Alloys Studied by Ab Initio Calculations," *Appl. Phys. Lett.*, vol. 91, no. 191904, pp. 1-3, 2007.

[110] T. Gebhardt, D. Music, M. Ekholm, I. A. Abrikosov, J. Von Appen, R. Dronskowski, D. Wagner, J. Mayer and J. M. Schneider, "Influence of Chemical Composition and Magnetic Effects on the Elastic Properties of FCC Fe-Mn alloys," *Acta. Mater.*, vol. 59, pp. 1493-1501, 2011.

[111] T. Gebhardt, D. Music, D. Kossmann, M. Ekholm, I. Abrikosov, L. Vitos and J. Schneider, "Elastic Properties of FCC Fe-Mn-X (X=Al, Si) Alloys Studied by Theory and Experiment," *Acta Mater.*, vol. 59, no. 8, p. 3145, 2011.

[112] S. Reeh, D. Music, T. Gebhardt, M. Kasprzak, T. Japel, S. Zaefferer, D. Rabbe, S. Richter, A. Schwedt, J. Mayer, B. Wietbrock, G. Hirt and J. M. Schneider, "Elastic Properties of Face-centered Cubic Fe-Mn-C Studied by Nanoindentation and Ab Initio Calculations," *Acta Mater.*, vol. 60, pp. 6025-6032, 2012.

[113] L. J. Teutonico, "The Widths of Glissile Extended Dislocations in Anisotropic Face Centered Cubic Metals," *Philos. Mag.*, vol. 15, p. 959, 1966.

[114] W. C. Oliver and G. M. Pharr, "An Improved Technique for Determining Hardness and Elastic Modulus Using Load and Displacement Sensing Indentation Experiments," *J. Mater. Res.*, vol. 7, no. 6, pp. 1564-1583, 1992.

[115] D. T. Pierce, J. Bentley, J. A. Jimenez and J. E. Wittig, "Stacking fault energy measurements of Fe-Mn-Al-Si austenitic twinning-induced plasticity steels," *Scripta Mat*, 2012.

[116] D. Pierce, J. Bentley, J. Jiménez and J. Wittig, "Stacking-Fault Energy Measurements in Fe-Mn-Al-Si Austenitic TWIP Steels," Nashville, 2011.

[117] D. T. Pierce, J. Bentley, J. A. Jiménez and J. E. Wittig, "The Influence of Stacking-Fault Energy on Deformation Mechanisms in an Fe-Mn-Al-Si Austenitic TRIP/TWIP Steel," in *Microsc. Microanal.*, Phoenix, 2012.

[118] H. Idrissi, L. Ryelandt, M. Veron, D. Schryvers and P. J. Jacques, "Is there a relationship between the stacking fault character and the activated mode of plasticity of Fe-Mn-based austenitic steels?," *Scripta Mater.*, vol. 60, p. 941, 2009.

[119] D. T. Pierce, K. Nowag, A. Montagne, J. A. Jimenez, J. E. Wittig and R. Ghisleni, "Single Crystal Elastic Constants of High-Manganese Transformation- and Twinning-Induced Plasticity Steels Determined by a New Method Utilizing Nanoindentation," *Mater. Sci. Eng., A*, vol. 578, pp. 134-139, 2013.

[120] D. T. Pierce, K. Nowag, A. Montagne, J. A. Jimenez and J. E. Wittig, "Single Crystal Elastic Constants of TWIP Steel Determined From Nanoindentation," in *Microsc. Microanal.*, Indianapolis, 2013.

[121] H. M. Ledbetter, N. V. Frederick and M. W. Austin, "Elastic-Constant Variability in Stainless-Steel

304," *J. Appl. Phys.*, vol. 51, no. 1, pp. 305-309, 1980.

[122] S. Kim and H. Ledbetter, "Elastic Constants of Four Fe-Cr-Ni-Mn Alloys," *J. Mat. Sci.*, vol. 29, pp. 5462-5466, 1994.

[123] H. M. Ledbetter, "Manganese Contributions to the Elastic Constants of Face Centered Cubic Fe-Cr-Ni Stainless Steel," *Journal of Materials Science*, vol. 20, pp. 2923-2929, 1985.

[124] J. J. Vlassak and W. D. Nix, "Indentation Modulus of Elastically Anisotropic Half Spaces," *Philos. Mag.*, vol. 67, no. 5, pp. 1045-1056, 1993.

[125] J. J. Vlassak and W. D. Nix, "Measuring the Elastic Properties of Anisotropic Materials by Means of Indentation Experiments," *J. Mech. Phys. Solids*, vol. 42, no. 8, pp. 1223-1245, 1994.

[126] H. M. Ledbetter, "Sound Velocities and Elastic-constant averaging for polycrystalline copper," *J. Phys. D: Appl. Phys.*, vol. 13, pp. 1879-1884, 1980.

[127] W. Wang and K. Lu, "Nanoindentation Study on Elastic and Plastic Anisotropies of Cu Single Crystals," *Philos. Mag.*, vol. 86, no. 33-35, pp. 5309-5320, 2006.

[128] M. Levy, H. E. Bass and R. R. Stern, Handbook of Elastic Properties of Solids, Liquids and Gasses, vol. 2, London: Academic Press, 2001.

[129] S. Kang, Y.-S. Jung, B.-G. Yoo, J.-i. Jang and Y.-K. Lee, "Orientation-dependent Indentation Modulus and Yielding in a High Mn Twinning-Induced Plasticity Steel," *Mater. Sci. Eng. A*, vol. 532, pp. 500-504, 2012.

[130] J. C. Stinville, C. Tromas, P. Villechaise and C. Templier, "Anisotropy Changes in Hardness and Indentation Modulus Induced by Plasma Nitriding of 316L Polycrystalline Stainless Steel," *Scripta Mat.*, vol. 64, pp. 37-40, 2011.

[131] M. J. Druyvesteyn and J. L. Meyering, "Elastical Constants in the System Cu-Zn," *Physica*, vol. 8, no. 9, pp. 1059-1074, 1941.

[132] H. W. King and M. A. Peters, "Predictive Equations for Martensitic and Antiferromagnetic Transformations in Fe-Mn-Al-Si Alloys," *Can. Metall. Q.*, vol. 36, no. 2, pp. 137-141, 1997.

[133] Y. S. Zhang, X. Lu, X. Tian and Z. Qin, "Compositional Dependence of the Neel Transition, Structural Stability, Magnetic Properties and Electrical Resistivity in Fe–Mn–Al–Cr–Si alloys," *Mater. Sci. Eng., A*, vol. 334, pp. 19-27, 2002.

[134] D. T. Pierce, J. A. Jiménez, J. Bentley, D. Raabe, C. Oskay and J. E. Wittig, "The Influence of Manganese Content on the Stacking-Fault and Austenite/ε-Martensite Interfacial Energies in Fe-Mn-(Al-Si) Steels Investigated by Experiment and Theory," *Acta Mat*, 2014.

[135] S. M. Cotes, A. Fernandez Guillermet and M. Sade, "FCC/HCP Martensitic Transformation in the Fe-Mn System: Part II. Driving Force and Thermodynamics of the Nucleation Process," *Metall. Mater. Trans. A,* vol. 35A, pp. 83-91, 2004.

[136] J.-E. Jin, M. Jung, C.-Y. Lee, J. Jeong and Y.-K. Lee, "Néel Temperature of High Mn Austenitic Steels," *Met. Mater. Int.,* vol. 18, no. 3, pp. 419-423, 2012.

[137] W. Huang, "An Assesment of the Fe-Mn System," *CALPHAD,* vol. 13, no. 3, p. 243, 1989.

[138] Y. N. Petrov, T. F. Volynova, I. A. Yakubtsov, I. B. Medov and V. M. Mnasin, "Cold Shortness of Iron-Manganese Alloys with Different Stacking Fault Energies," *Phys. Met. Metall.,* vol. 68, no. 6, pp. 169-172, 1989.

[139] D. Djurovic, B. Hallstedt, J. Von Appen and R. Dronskowski, "Thermodynamic Assessment of the Fe-Mn-C system," *CALPHAD,* vol. 35, pp. 479-491, 2011.

[140] X. Tian and Y. Zhang, "Effect of Si Content on the stacking fault energy in gamma Fe-Mn-C-Si Alloys: Part 1. X-ray diffraction line profile analysis," *Mater. Sci. Eng. A.,* vol. 516, pp. 73-77, 2009.

[141] X. Tian and Y. Zhang, "Effect of Si Content on the Stacking Fault Energy in γ-Fe-Mn-Si-C Alloys: Part II. Thermodynamic Calculation," *Mater. Sci. Eng. A,* vol. 516, pp. 78-83, 2009.

[142] D. Djurovic, B. Hallstedt, J. Von Appen and R. Dronskowski, "Thermodynamic assesment of the Mn-C system," *CALPHAD,* vol. 34, pp. 279-285, 2010.

[143] K. Frisk, "A Thermodynamic Evaluation of the Cr-Mn-N System," *CALPHAD,* vol. 17, no. 3, pp. 335-339, 1993.

[144] A. T. Dinsdale, "SGTE Data for Pure Elements," *CALPHAD,* vol. 15, no. 4, pp. 317-425, 1991.

[145] P. Gustafson, "A Thermodynamic Evaluation of the Fe-C System," *Scand. J. Metall.,* vol. 14, p. 259, 1985.

[146] A. Shukla and A. D. Pelton, "Thermodynamic Assessment of the Al-Mn and Mg-Al-Mn Systems," *Journal of Phase Equilibria and Diffusion,* vol. 30, no. 1, pp. 28-39, 2009.

[147] J. LaCaze and B. Sundman, "An Assessment of the Fe-C-Si System," *Metall. Trans. A.,* vol. 22, pp. 2211-2223, 1991.

[148] J. Miettinen, "Reassessed Thermodynamic Solution Phase Data for the ernary Fe-Si-C System," *CALPHAD,* vol. 22, no. 2, pp. 231-256, 1998.

[149] L. Li and T. Y. Hsu, "Gibbs Free Energy Evaluation of the FCC(γ) and HCP(ε) Phases in Fe-Mn-Si Alloys," *Calphad,* vol. 21, no. 3, pp. 443-448, 1997.

[150] S. Cotes, A. Fernandez Guillermet and M. Sade, "Phase Stability and FCC/HCP Martensitic Transformation in Fe–Mn–Si Alloys: Part II. Thermodynamic Modeling of the Driving Forces and the Ms and As Temperatures," *J. Alloys Compd.,* vol. 280, pp. 168-177, 1998.

[151] A. Forsberg and J. Agren, "Thermodynamic Evaluation of the Fe-Mn-Si System and the y/e Martensitic Transformation," *J. Phase Equilib.,* vol. 14, no. 3, pp. 354-363, 1993.

[152] W. S. Yang and C. M. Wan, "The Influence of Aluminum Content to the Stacking Fault Energy in Fe-Mn-Al-C Alloy System," *Journal of Materials Science* , vol. 25, pp. 1821-1823, 1990.

[153] H. Schumann, "EinfluB der Stapelfehlerenergie auf den kristallographischen Umgitterungsmechanismus der y/a-Urnwandlung in hochlegierten Stalhlen," *Kristall Technik,* vol. 9, no. 10, pp. 1141-1152, 1974.

[154] S. Cotes, A. Fernandez Guillermet and M. Sade, "Phase stability and fcc/hcp martensitic transformation in Fe-Mn-Si alloys Part I. Experimental study and systematics of the Ms and As temperatures," *J. Alloys Compd.,* vol. 278, pp. 231-238, 1998.

[155] S. R. Kalidindi, "Modeling the Strain Hardening Response of Low SFE FCC Alloys," *Int. J. Plast.,* vol. 14, pp. 1265-1277, 1998.

[156] U. F. Kocks and H. Mecking, "Physics and phenomenology of strain hardening: the FCC case," *Prog Mater Sci,* vol. 48, pp. 171-273, 2003.

[157] S. Asgari, E. El-Danaf, S. Kalidindi and R. Doherty, "Strain Hardening Regimes and Microstructural Evolution during Large Strain Compression of Low Stacking Fault Energy FCC Alloys that Form Deformation Twins," *Met. Trans A,* vol. 28, pp. 1781-1795, 1997.

[158] H. Ding, Z.-Y. Tang, W. Li, M. Wang and D. Song, "Microstructures and Mechanical Properties of Fe-Mn-(Al,Si) TRIP/TWIP Steels," *J. Iron Stl. Res.,* vol. 13, no. 6, pp. 66-70, 2006.

[159] D. Kuhlmann-Wilsdori, H. G. F. Wilsdorf and J. A. Wert, "LEDS Theory of Workhardening Stages and "Planar" Versus "Distributed Glide," *Sripta Met.,* vol. 31, no. 6, pp. 729-734, 1994.

[160] D. Kuhlmann-Wilsdorf, "Energy Minimization of Dislocations in Low-Energy Dislocation Structures," *Phys Stat Sol (a),* vol. 104, pp. 121-144, 1987.

[161] D. Kuhlmann-Wilsdorf and N. Hansen, "Theory of work-hardening applied to stages III and IV," *Met. Trans. A,* vol. 20, pp. 2393-2397, 1989.

[162] S. I. Hong and C. Laird, "Mechanisms of Slip Mode Modification in F.C.C Solid Solutions," *Acta Metal. Mater.,* vol. 38, no. 8, pp. 1581-1594, 1990.

[163] W. Puschl, "Models for dislocation cross-slip in close-packed crystal structures: a critical review," *Prog. Mater Sci.,* vol. 47, pp. 415-461, 2002.

[164] M. Hokka, S. Curtze, V.-T. Kuokkala, P. Peura and R. Oyj, "Dynamic Response of High-Manganese TWIP Steels," in *Society for Experimental Mechanics XI International Congress & Exposition on Experimental & Applied Mechanics*, Orlando, 2008.

[165] S. Curtze, "Characterization of the Dynamic Behaivor and Microstructure Evolution of High Strength Sheet Steels," Tampere, 2009.

[166] M. Borsutzki, D. Cornette, Y. Kuriyama, A. Uenishi, B. Yan and E. Opbroek, "Reccomendations for Dynamic Tensile Testing of Sheet Steels," 2005.

[167] I. Choi, D. Son, S. Kim, D. K. Matlock and J. G. Speer, "Strain Rate Effects on Mechanical Stability of Retained Austenite in TRIP Sheet Steels," in *SAE World Congress & Exhibition*, 2006.

[168] N. Li, Y. D. Wang, R. Lin Peng, X. Sun, P. K. Liaw, G. L. Wu, L. Wang and H. N. Cai, "Localized Amorphism After High-Strain-Rate Deformation in TWIP Steel," *Acta Mater.*, vol. 59, pp. 6369-6377, 2011.

[169] J. R. Neighbours, F. W. Bratten and C. S. Smith, "The Elastic Constants of Nickel," *J. Appl. Phys.*, vol. 23, no. 4, pp. 389-393, 1952.